

Instituto Tecnológico y de Estudios Superiores de Monterrey

Campus Monterrey

School of Engineering and Sciences



**TECNOLOGICO  
DE MONTERREY®**

**An integrated approach for additive manufacturing process  
planning: Selective Laser Melting**

A dissertation presented by

**Erick Ramirez-Cedillo**

Submitted to the  
School of Engineering and Sciences  
in partial fulfillment of the requirements for the degree of

Doctor of Philosophy

In

Engineering Science

Major in Advanced Manufacturing

Monterrey Nuevo León, December 13<sup>th</sup>, 2019  
Instituto Tecnológico y de Estudios Superiores de Monterrey

Campus Monterrey

Instituto Tecnológico y de Estudios Superiores de Monterrey

Campus Monterrey

School of Engineering and Sciences

The committee members, hereby, certify that have read the dissertation presented by Erick Guadalupe Ramírez Cedillo and that it is fully adequate in scope and quality as a partial requirement for the degree of Doctor of Philosophy in Engineering Sciences, with a major in Your Major.

Ciro Ángel Rodríguez González, Ph.D  
Tecnológico de Monterrey  
School of Engineering and Sciences  
Principal Advisor

Dr. Leopoldo Ruiz Huerta, Ph.D  
Universidad Nacional Autónoma de México  
Co-advisor

Dr. Héctor R. Siller, Ph.D  
University of North Texas  
Co-advisor

Jesús Alejandro Sandoval Robles, Ph.D  
Tecnológico de Monterrey  
Committee Member

Erika García López, Ph.D.  
Tecnológico de Monterrey  
Committee Member

Omar Eduardo López Botello, Ph.D  
Tecnológico de Monterrey  
Committee Member



Dr. Rubén Morales Menéndez  
Dean of Graduate Studies  
School of Engineering and Sciences  
Monterrey Nuevo León, December 10<sup>th</sup>, 2019

## Declaration of Authorship

I, Erick Ramírez-Cedillo, declare that this dissertation titled, **An integrated approach for additive manufacturing process planning: Selective Laser Melting** and the work presented in it are my own. I confirm that:

- This work was done wholly or mainly while in candidature for a research degree at this University.
- Where any part of this dissertation has previously been submitted for a degree or any other qualification at this University or any other institution, this has been clearly stated.
- Where I have consulted the published work of others, this is always clearly attributed.
- Where I have quoted from the work of others, the source is always given. With the exception of such quotations, this dissertation is entirely my own work.
- I have acknowledged all main sources of help.
- Where the dissertation is based on work done by myself jointly with others, I have made clear exactly what was done by others and what I have contributed myself.

A handwritten signature in black ink, appearing to read 'Ramírez', enclosed within a large, stylized, hand-drawn triangular shape.

---

Erick Ramírez-Cedillo (Student)  
Monterrey Nuevo León, December 13<sup>th</sup>, 2019

@2019 by Erick Ramírez-Cedillo  
All rights reserved

## **Dedication**

To my parents (Jorge and Marina) for all your support during this chapter of my life.

## Acknowledgements

I would like to express my deepest gratitude to my mentor and co-advisor, Dr. Hector Siller, for the support during this thesis project, for this innovation, motivation, and career advisor.

I wish to show my gratitude to Dr. Ciro Rodríguez, who has always given the right words, the best advice, support, and the best example of a leader and advisor. I learned how to manage my professional and research life.

For the critical view and for being the best technical advisor, I want to thank my co-advisor Dr. Leopoldo Ruiz. Also, I want to express my gratitude to my two tutors: Dr. Jesús Sandoval and Dra. Erika López was a strong motivation for this project and had the patience and right feedback.

**I want to acknowledge the support of the following persons who co-authorship my articles:**

- BEng. Regina Vargas
- Dra. Wendy Ortega
- Dr. Israel Martínez
- Dr. Omar López
- Dr. Alejandro Alvarez
- Dr. Luis Zamudio
- Dr. Alberto Caballero
- Dr. Edgar Montufar
- Dra. Aída Rodríguez

I want to share my gratitude with the following persons that support me and gave me hope and good advice during my PhD.

- My business partner and best friend, Hiram Uribe, supports me in this process.
- Raquel Tejeda and Javier Vázquez that helped me and stayed with me in the good and bad times.
- My friends: Dinorah, Mariana, Cristina, Rubí, Adrián, Nayeli, Diana, Alberto, Carlos, Saket, Marinela, Jashim, Cesar, Vanessa.
- My texas' family opened their home and received me as a member of the family in Denton, Texas. Thanks Jane, Spencer, Colin, and Marjorie.

### **Funding:**

I acknowledge part financial support for this work from a seed research project funded by the Advanced Materials and Manufacturing Processes Institute (AMMPI) at the University of North Texas (UNT), from the CONACyT Mixed Scholarships Program, and from Tecnológico de Monterrey, Research Group of Advanced Manufacturing. My sincere gratitude to Tecnológico de Monterrey support on tuition and CONACyT with the support for living.

# **An integrated approach for additive manufacturing process planning: Selective Laser Melting**

By

Erick Ramírez-Cedillo

## **Abstract**

In many industrial applications, Laser Powder Bed Fusion Technology (LPBF) commercially well-known Selective laser melting (SLM) has been recognized for its flexibility in Net Shape Manufacturing. Where a feedstock is deposited and selectively fused with a thermal joining via laser power. In this work, an overview and integrated approach for the additive manufacturing process planning is presented. The unit process life cycle inventory (UPLCI) was used to discretize energy consumption and material losses for modeling the SLM process. A reusable perspective in terms of materials, parameters, and calculation tools to estimate the energy consumption and mass loss in practical evaluations of production lines is presented. Calculations of energy were obtained and classified as basic, idle, and active energy. Theoretical equations were also shown to relate the most important parameters of the process with its energy consumption. On the other hand, the optimization and characterization of parts for the processing parameters calibration in LPBF has been recently well studied in academia, but still under research in the industry, due to the early adoption of this technology in different companies and research centers. For this reason, a process planning workflow for the obtention of calibrated ranges of parameters for AISI 316L samples, and to understand the relationship between the improved parameters, the surface quality and part integrity with the microstructural characteristics. Two principal methods of characterization, (1) Nanoindentation and Electron backscatter diffraction (EBSD) and (2) non-contact profilometry by Focus Variation, were used to validate the influence of the overlap of the point distance (PD) and hatch distance (HD) in the fabrication process. In this study, hardness and the modulus of elasticity exhibited the highest values of 4.59 GPa and 229.7 GPa respectively in the parallel orientation to the build direction. The obtained hardness and modulus of elasticity were correlated with the different grain sizes and the resulting crystallographic orientation product of the thermal history of the process. Roughness (Ra) was improved with the selection of parameters and presented the lowest value of 5.433  $\mu\text{m}$ . Finally, the microstructure was studied on the samples as the final assessment on the improved parameters where finer cellular/dendritic structures were found. At the end, a series of case studies were presented at the end to validate the use of these two-process planning methodology in the medical device applications.

# List of Figures

Figure 1.1 Metal Additive Manufacturing overview .....	13
Figure 2.1 a) Selective laser melting machine (Photographs from Renishaw, UK) b) SLM Process schematics.....	17
Figure 2.2. SLM parameters. a) Laser parameters. b) Laser scanning strategy c) Parameters related to the AM process d) Powder parameters.....	18
Figure 2.3 LCI data for SLM Process.....	19
Figure 2.4 Input-Output diagram of an SLM process.....	19
Figure 2.5. Generic power and time profile in SLM with energy as the area under the power-time graphs as shown. ....	22
Figure 2.6. System boundary of the SLM process .....	23
Figure 2.7. Top variables for SLM.....	25
Figure 2.8. Tibia fixation plate .....	32
Figure 2.9. Laser strategy and (b) supports system, (c) laser strategy, (d) filling, (e) upskin filling, (f) fill contour 1 (g) fill contour 2, (h) border, (i) upskin border.....	33
Figure 2.10. Power vs time during the SLM process.....	34
Figure 2.11. Implant with support. ....	37
Figure 3.1. Process parameters. <b>(a)</b> Overview of the processing variables in the building chamber. <b>(b)</b> Parameters related to modulated lasers <b>(c)</b> Parameters related remelting and rotation angles through the part. ....	44
Figure 3.2.Laser scanning strategies. ....	44
Figure 3.3. Selection criteria for best parameters, adapted from [12] .....	45
Figure 3.4 Proposed process tasks to obtain parameter ranges. ....	51
Figure 3.5 <b>(a)</b> . Particle size distribution. <b>(b)</b> SEM Micrograph of stainless steel powder with $D_{90}=42.84 \mu\text{m}$ .....	52
Figure 3.6. Overlapping percentages of PD and HD (a) 75%, (b) 50%, (c) 25% .....	53
Figure 3.7. AISI 316L part from which two samples were made by cutting it with EDM on perpendicular (PERP) and parallel (PAR) to build orientation. ....	55
Figure 3.8. Visual selection of <b>(A)</b> Non continuous weld line P: 125W ET: 80 $\mu\text{s}$ PD: 56 $\mu\text{m}$ <b>(B)</b> Spatter particles surrounding the weld lines P: 175W ET: 80 $\mu\text{s}$ PD: 37 $\mu\text{m}$ <b>(C)</b> Uniform weld line P: 175W ET: 50 $\mu\text{s}$ PD: 18 $\mu\text{m}$ .....	57
Figure 3.9. Top parameters in Build 1 <b>(A)</b> P: 175W ET: 50 $\mu\text{s}$ PD: 18 $\mu\text{m}$ <b>(B)</b> Spatter particles surrounding the weld lines P: 125W ET: 80 $\mu\text{s}$ PD: 18 $\mu\text{m}$ , and <b>(C)</b> Uniform weld line P: 175W ET: 80 $\mu\text{s}$ PD: 18 $\mu\text{m}$ .....	57
Figure 3.10. Roughness on the PERP orientation of the Build 2 parts (variation of hatch distance): <b>A)</b> HD: 18 $\mu\text{m}$ , <b>B)</b> HD: 37 $\mu\text{m}$ , and <b>C)</b> HD: 56 $\mu\text{m}$ . ....	58

Figure 3.11 Roughness on the perpendicular and parallel orientation of the samples. (Lowest values of Roughness are marked with * in blue). .....	59
Figure 3.12 SEM Micrographs, <b>(A)</b> Well defined weld lines (150x), <b>(B)</b> Agglomeration of particles and voids (150x), <b>(C)</b> Balling effect and particles concentration (50x), and <b>(D)</b> Critical damaged surface (150x).....	60
Figure 3.13 Nanoindentation measurements of samples. <b>(A)</b> Modulus of Elasticity (GPa) and <b>(B)</b> Hardness (GPa). .....	61
Figure 3.14. NanoSEM EBSD IQ+IPF maps with nanoindents at 500X <b>(A)</b> PAR orientation and <b>(B)</b> PERP orientation of sample 5 (Parameters: HD: 37 $\mu$ m P: 125W ET: 80 $\mu$ s PD: 18 $\mu$ m) (best mechanical properties) <b>(C)</b> PAR orientation and <b>(D)</b> PERP orientation of sample 6 ( Parameters: HD: 37 $\mu$ m P: 175 W ET: 80 $\mu$ s PD: 18 $\mu$ m) (best roughness) <b>(E)</b> Original IQ of an indent, and <b>(F)</b> IPF Iron (Gamma).....	65
Figure 3.15. FIB/SEM images showing microstructures of two different laser powers, <b>(A)</b> and <b>(B)</b> Microstructural characteristics with layer-layer fusion pool boundary with laser power of 125 watts, <b>(C)</b> and <b>(D)</b> Microstructural characteristics of higher laser power of 175 watts. ....	67
Figure 3.16 Microstructures of various laser power with various hatch distances on both parallel and perpendicular to build direction are shown (HD: 37 $\mu$ m P: 125W ET: 80 $\mu$ s PD: 18 $\mu$ m) <b>(A)</b> and <b>(B)</b> show the microstructural characteristics in PERP and PAR respectively. <b>(C)</b> and <b>(D)</b> show the microstructural characteristics in PERP and PAR (HD: 37 $\mu$ m P: 175W ET: 80 $\mu$ s PD: 18 $\mu$ m), and lastly for <b>(E)</b> and <b>(F)</b> show microstructural characteristics in PAR and PER of (HD: 56 $\mu$ m P: 175W ET: 80 $\mu$ s PD: 18 $\mu$ m). .....	68



# List of Tables

Table 2-1. Time study for SLM operations from the case study and the literature. ....	21
Table 2-2. Volumetric energy density for different materials. ....	25
Table 2-3. Processing parameters for stainless steel 316L. ....	26
Table 2-4. Energy consumed through different stages of the SLM process. ....	27
Table 2-5. Waste streams in SLM. ....	29
Table 2-6. Specifications of a Renishaw 400 SLM system. ....	31
Table 2-7. Specifications of the implant. ....	31
Table 2-8. Processing parameters for the case of study. ....	32
Table 2-9. Peripheral equipment and their power consumption and times. ....	35
Table 2-10. Stages of the idle energy ....	35
Table 3-1. Main studies using Linear Energy Density (LED) for parameters optimization. ....	46
Table 3-2. Main studies with VED for the optimization of parameters ....	47
Table 3-3. Literature overview of the processing parameters for different materials. .	48
Table 3-4. Processing parameters for Build 2. ....	53

# Contents

<b>Abstract</b>	5
<b>List of Figures</b>	6
<b>List of Tables</b>	8
<b>Chapter 1. Metal Additive Manufacturing: overview</b>	12
Hypothesis	13
1.1 Motivation	13
1.2 Problem Statement and Context	14
1.3 Research Question	14
1.4 Solution overview	14
<b>Chapter 2. Reusable unit process life cycle inventory for manufacturing: selective laser melting</b>	15
Abstract	15
1. Introduction	15
2. Methodology for Unit Process Life Cycle Inventory Model	19
2.1 Selective Laser Melting Process Energy Characteristics	20
2.2 Parameters Affecting the Energy Consumed for Selective Laser Melting	23
2.3 Energy through the SLM process.	24
2.3.1 Active energy	24
2.3.2 Idle Energy	28
2.3.3 Basic Energy	28
2.3.4 Summary on Unit Process Life Cycle Energy	29
2.4 Method of Quantification for Mass Loss	29
2.4.1 LCI for Material Mass Loss Calculations	30
2.4.2 LCI for Inert Gas Loss Calculations	30
3. Case Study on SLM	31
3.1 Product Details:	31
3.2 Processing parameters	32
3.3 SLM process	33
3.4 Time and Energy calculations	34
3.4.1 Basic energy	34
3.4.2 Idle energy	35
3.4.3 Active energy	36

3.4.4 Volumetric energy density (VED)	36
3.4.5 Total energy	37
3.6 LCI mass loss calculations	37
3.6.1 Inert gas loss calculations	37
3.6.2 Material gas loss calculations	38
4. Conclusions	38
Future works	39
References	39
List of symbols	41
Abbreviations	41
<b>Chapter 3. Process planning of L-PBF of AISI 316L for improving surface quality and relating part integrity with microstructural characteristics</b>	<b>42</b>
1. Introduction	42
a) Scanning strategies	44
b) Linear energy density (LED)	45
c) Volumetric energy density (VED)	46
1.1 Focus Variation	49
1.2 Nanoindentation and Electro Backscatter Diffraction	50
2. Materials and Methods	51
2.1 Materials and Experimental Set-Up	51
2.2 Samples design	52
2.3 Design of experiments	52
2.4 Visual Characterization and Topography characterization	54
2.5 Nanoindentation and microstructure	54
3. Results and discussion	56
3.1 Visual characterization and surface topography characterization and Roughness (Ra)	56
3.2 Morphological characterization	59
3.3 Nanoindentation and microstructure	60
3.3.1 Nanoindentation	60
3.3.2 Electron Backscatter Diffraction	62
3.4 Microstructure analysis	65
4. Conclusions	69
Abbreviations	70
Nomenclature	70

References	70
<b>Chapter 3 Overall Conclusions</b>	<b>76</b>
<b>Appendix A</b>	<b>77</b>
<b>Appendix B</b>	<b>88</b>
<b>Appendix C</b>	<b>100</b>
<b>Published papers</b>	<b>111</b>
<b>Curriculum Vitae</b>	<b>112</b>



Figure 1.1 Metal Additive Manufacturing overview

## Hypothesis

It is acknowledged the strong influence of process parameters in the quality of parts produced by Selective Laser Melting, SLM, and it is also well known that the heterogeneity of machines, laser, hardware and software architectures is a challenge toward the industrial implementation of the process.

It is hypothesized that the standardization of data, information and knowledge related with all the process input and output variables will improve the process planning of this additive manufacturing process, having multiple planning layers, from energy management with modeling techniques to parameters calibration with innovative destructive and non-destructive testing techniques

### 1.1 Motivation

Surgical instruments, hip, ankle, tibia, and shoulder joints require a smooth surface, while for prosthetic components that need osseointegration like pins, implants, and screws, surfaces must have customized properties. Regarding the Additive Manufacturing technologies, several process parameters can be modified to improve the roughness and mechanical properties of the final part, achieving acceptable values to minimize the post-processing.

## 1.2 Problem Statement and Context

From the previous overview of the metal additive manufacturing challenges, an area of opportunity in the medical field was identified. Where the widespread clinical use of medical devices fabricated with additive manufacturing and medical device integration can contribute to improve workflow, reduce clinical errors and costs. With additive manufacturing complex forms and risky cases can be approached, but several protocols and guidelines are required to ensure that these medical devices can fulfill its function without failure. Also, to have a process, planning and guidance is a challenge for new technologies due to the lack of standards and certifications. Since 2017, the National Institute of Standards and Technology (NIST) has been developing standards for metal additive manufacturing pushed by the aerospace and automotive industries. Overall, a process mapping that can be translated into different systems and machines is needed for the industry. But, also specific requirements such as surface integrity and mechanical properties are relevant in the fabrication of parts. In the medical field, both part characteristics have a strong influence on the success of the medical device implantation in a patient.

## 1.3 Research Question

How can the standardization of data, process guidelines, information, and knowledge with all variables (input and output) improve the process planning in the production of implants using SLM technologies?

## 1.4 Solution overview

- Standardization of data, process guidelines, of all variables (input and outputs) has been set up by using a Unit Process Life Cycle Inventory (UPLCI) methodology.
- A process guideline for all variables related to the manufacturing process has been presented as a way to obtain optimized ranges of parameters for a specific material by using different characterization methods.
- A validation with different process chains for the fabrication of customized, complex and optimized implants has proved that LPBF can meet the requirements for the manufacturing of medical devices

# Chapter 2. Reusable unit process life cycle inventory for manufacturing: selective laser melting

## Abstract

In many industrial applications, Selective laser melting (SLM) has been recognized for its flexibility in Net Shape Manufacturing. In this powder bed fusion technology, a feedstock is deposited and selectively fused with a thermal joining via laser power. In this work, the unit process life cycle inventory (UPLCI) was used to discretize energy consumption and material losses for modeling the SLM process. A reusable perspective in terms of materials, parameters, and calculation tools to estimate the energy consumption and mass loss in practical evaluations of production lines is presented. Calculations of energy were obtained and classified as basic, idle, and active energy. Theoretical equations were also shown to relate the most important parameters of the process with its energy consumption. Finally, a case study is presented to analyze the UPLCI capacity to improve energy consumption in the manufacturing of medical devices.

**Keywords:** *unit process life cycle inventory, selective laser melting, additive manufacturing, energy consumption.*

## 1. Introduction

Selective Laser Melting is a transforming process of mass conservation categorized as thermal joining due to laser energy used for the welding of successive layers. According to ASTM 52900:2015, SLM is classified as a powder bed fusion technology where a feedstock is deposited and selectively fused with a heating agent [1]. The principle is based on laser fusion of a layer of powder material with a laser scanning pattern on a building platform which moves in Z-axis direction for the addition of a new powder layer. Parts of different alloys such as stainless AISI 316L, Cobalt-Chromium alloy (Co-Cr), Ti6Al4V, Aluminum alloys, Nickel alloys among others can be manufactured through this process. The selection of the powder material depends on the mechanical, chemical and physical properties of the final application, which are adapted to the medical, aerospace, automotive and other industries where highly complex geometries or customization is required. Metal Additive Manufacturing (MAM) has presented 875% growth in the past five years, and 220% in 2016-2017 [2].

The manufacturing process starts with a digital geometry file which is converted to STL (Standard Tessellation Language file) and introduced to the machine software where parameters are selected, and a code is generated and sent to the SLM system. After that, the SLM system is prepared to fabricate parts. The size and shape of the powder considered to feed the machine are strongly important as the inert gas (commonly Ar or N<sub>2</sub> according to the chemistry of the alloy) is used for filling the process chamber to avoid any reaction related with the powder (i.e., reducing oxidation, controlling humidity and adjusting the temperature of the system). In the HMI (Human-Machine Interface) screen of the SLM system, the file is selected, and the machine starts the pressurizing of the chamber. Then, the inert gas flows inside the chamber to reduce the O<sub>2</sub> to less than 10 ppm (parts per million) [3]. Afterwards, the powder covers the building plate with a roller, blade or a combination of them which produce a uniform distribution over it. After the powder has covered the building plate, the laser (CO<sub>2</sub>, lamp or Nd: YAG laser, disk or a fiber laser) adapted to a beam deflection system (Galvanometric mirrors) melts each layer with a scanning strategy. When the layer is finished, the building plate moves down in Z-axis, and the process is repeated. Inert gasses are in continuous flow during the process and perpendicular to the roller mechanism to avoid inconsistencies and provide a safer environment. Depending on the material, the building plate is adjusted to a temperature to conserve it during the additive process. After the additive process is completed, cooling time is automatically set, and the building chamber is cleaned by moving the non-used powder to the containers for its recycling. Parts are removed from the building plate and cleaned using an ultrasonic bath. If it is needed, parts could be post-processed with mechanical or electrochemical polishing to enhance surface quality.

Some authors [4–8] have adopted Life Cycle Inventory (LCI) or performed the environmental and energy assessment of AM. For example, Kellen's et al. performed an energy and performance analysis of the SLM process by collecting data using life cycle inventory (LCI) and discretized some of the elements of machine energy consumption. The study consisted of a power analysis, where it was found an average power consumption of 3.25 kW when the laser was active, and total energy of the building process of 39.60MJ for 0.409kg of stainless steel 316L[9]. Besides, Baumers et al. compared electron beam melting (EBM) and SLM process energy consumptions where it was reported energy consumption of 111.60 - 139.50 MJ per kg of stainless steel 316L while EBM resulted in 61.20-176.67 MJ per kg, but some quality characteristics were compromised in EBM [10].

Faludi et al. measured with LCI the environmental impacts of SLM in terms of energy consumed per part (MJ/part) using aluminum-silicon powder considering all peripheral equipment. They found that auxiliary equipment consumes more energy than the SLM system. Also, they relate the energy consumed with productivity, and they found an energy consumption of 68.88MJ (0.058 kg) when producing one part while when producing 12 parts, the energy required was 32.98MJ (0.696 kg) for each part concluding that by having a full building plate of parts, energy can be optimized. In addition, material removal processes should be used instead



of EDM because the energy consumed after the SLM process increases per part in 28 % [4]. After LCI analysis on SLM process, authors have found that savings in energy can be obtained by optimizing the orientation of the part, parameters, and design [11], or maximizing the capacity with a full filled building platform [12, 13], performing design optimization of the parts [14], and even selecting an adequate material for the part[5].

The unit process life cycle inventory (UPLCI) was developed for high production in manufacturing operation pursuing the environmental performance assessment of the process taking into consideration all inputs and outputs [15]. For AM processes, it is of great importance to study systematically the electric energy consumption, the material used and recycled, waste, and inert gas consumption.

Figure 2.1a illustrates a SLM machine configuration, while Figure 2.1b shows the process schematics. Process variables related to the laser unit and optical array are laser power ( $P$ ), exposure time ( $ET$ ), and the spot size diameter ( $SS$ ). Variables related to the scanning strategy are point distance ( $PD$ ), and hatch distance ( $HD$ ). Parameters associated with the additive process are the number of layers ( $n$ ), layer thickness ( $LT$ ), and the speed of the roller (Figure 2.2), while the powder alloy parameters as size distribution and shape are also related with the  $LT$  and indirectly related with  $SS$ ,  $HD$  among others.

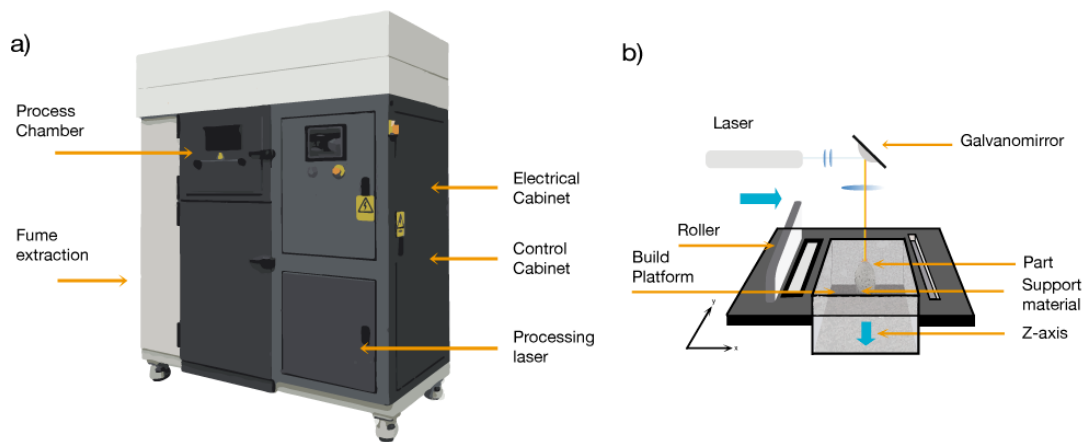


Figure 2.1 a) Selective laser melting machine (Photographs from Renishaw, UK) b) SLM Process schematics.

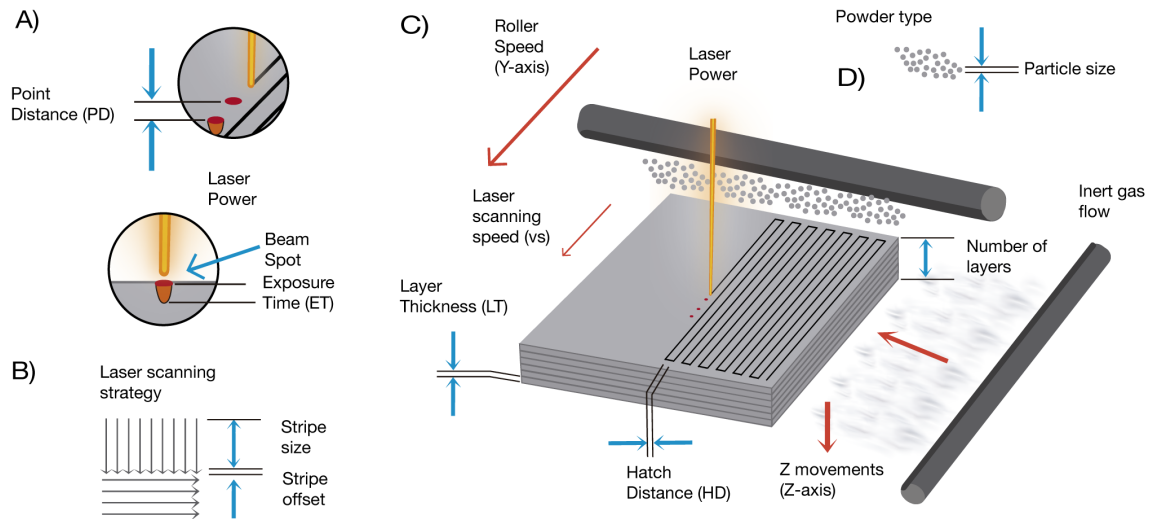


Figure 2.2. SLM parameters. a) Laser parameters. b) Laser scanning strategy c) Parameters related to the AM process d) Powder parameters

Figure 3 shows an overview of the developed environmental-based factors for SLM according to UPLCI methodology. For a given workpiece, the life cycle analysis yields energy use, recyclable powder, inert gas, and waste. Inputs such as the material in the form of powder (new or recycled), inert gas, energy (electricity), dry air, process parameters, and the preparation (set-up) of the machine are introduced to the SLM system. The process cycle will be defined by the number of layers of powder deposited and melted by the laser. At the end of the process, the parts are cooled for a specific time. Non-melted powder and parts are the final outputs of the process, the powder is sieved, and pieces can be post-processed using mechanical or electrochemical polishing.

At the bottom of Figure 2.3, LCI methodology is summarized and inputs are named as resource data (all the requirements to start the process). Inside the process variables, the LCI measurable variables are presented as the machine energy, the inert gas consumption, the powder, and waste. Finally, as output, the LCI data are referred to the information obtained during the SLM process about the measurable variables.

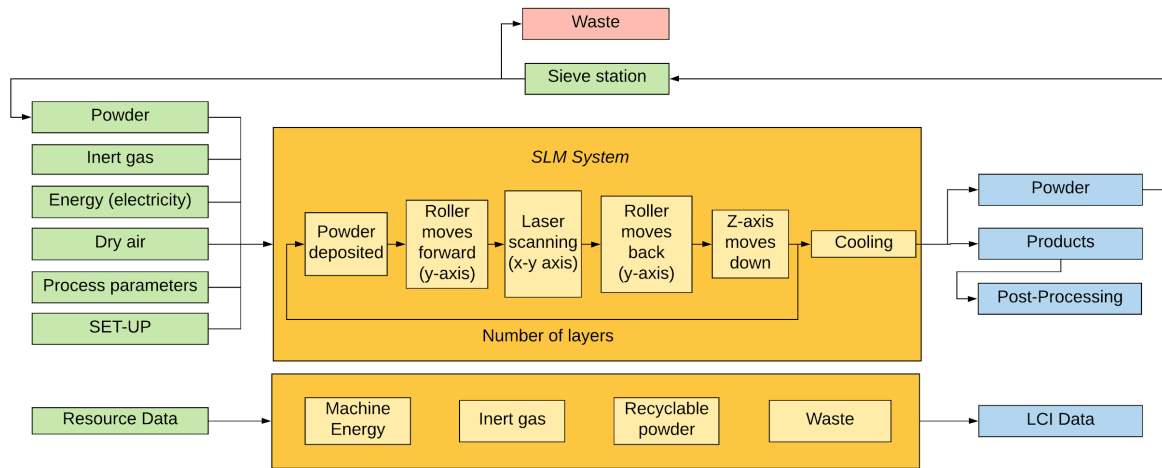


Figure 2.3 LCI data for SLM Process.

## 2. Methodology for Unit Process Life Cycle Inventory Model

The concept of unit operation is applied in order to assess the manufacturing process in terms of environmental impact. The unit process consists of inputs, process components, and outputs of operation. Each unit process is converting material/chemical inputs into a transformed material/chemical output. The unit process diagram of the SLM process is shown in Figure 2.4.

The transformation of input to output results in this report generates five LCI characteristics,

- Input requirements [powder characteristics, inert gas characteristics, energy (electricity), dry air, process parameters, set-up preparation (consumables)].
- Material loss (that may be subsequently recycled or declared waste).
- Primary machine and material variables relating inputs to outputs.
- Resulting characteristics of the output product that might enter the next unit process.

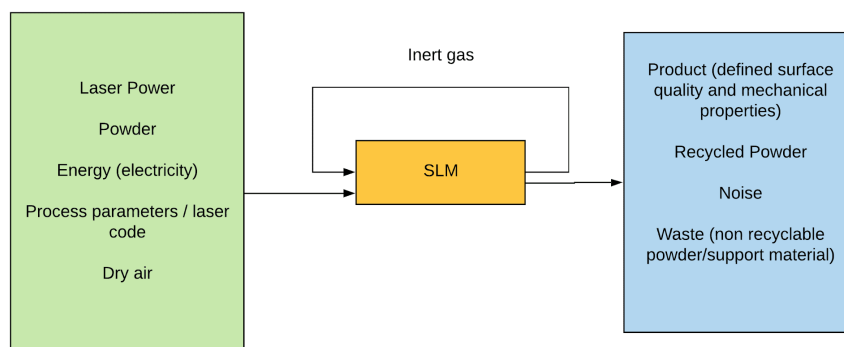


Figure 2.4 Input-Output diagram of an SLM process

## 2.1 Selective Laser Melting Process Energy Characteristics

Selective laser melting machine consists of a laser beam that is focused selectively by galvanometric mirrors in a building platform, in which a roller is displaced in y-axis to distribute metallic powder thoroughly, and a servo motor is controlled in the Z-axis to move down the platform after the melt layer is produced [4, 16]. This process continues until consecutive layers are finished.

The UPLCI is based on a representative operational sequence, as follows.

- a) *Generation of laser strategy.* Firstly, a 3D model is introduced to the SLM machine software. The orientation of the part, the support material, the number of pieces and parameters are defined. Selecting the right laser strategy can take different times and depends on parameters selection, mesh quality of the 3D model, the addition of specific support, and selection of laser scanning strategies.
- b) *Set-up by the operator.* It includes turning on the SLM system [*Stand by*] dehumidifier and chiller, the opening of inert gas and dry air, fume extraction (filter valves) and powder containers valves. After that, the roller is assembled (silicone changed), and building plate is collocated and fixed with screws to the process chamber. Then, Z-axis is calibrated with 100  $\mu\text{m}$  thick shim, the file is selected, and the operator pushes the button of start.
- c) *Warm up.* The building chamber is pressurized at a specific pressure while the inert gas flows through the chamber until it gets on the required level of  $\text{O}_2$  (typically less than 2000 ppm). Set-up times from the literature are given in Table 1.
- d) Process time can be determined by the laser scanning and the Z-axis movements [*SLM process*].
  - i) Since the STL is divided into slices according to layer thickness size, it can have different area sizes (X-Y) through its construction because it depends on the geometry of the part and the orientation. So, different processing times can be obtained through the layers due to the size of the sliced area. In addition, laser scanning strategies may represent different times of fabrication, and surface properties[17]; for example, meander (simple hatching) strategy will take the longest time because of its movements are line by line unlike chessboard (quad hatching) and stripes where the laser is divided by section areas resulting in a faster way of melting the powder compared with meander strategy.
  - ii) The time required for the roller along Y-axis and the Z-axis movements is constant through all the process.

- iii) Cooling time is set at the end of the fabrication [*Cooling*].
- e) *Cleaning time* depends on the amount of powder over the parts in the building chamber. Removing the parts from the building plate can be performed through a mechanical deformation or electro-discharge machining processes. Then parts are introduced to an ultrasonic bath for 5 to 10 min for removing the powder added to the external surface.
- f) When the operation is finished, the workpiece is unloaded and might be sent forward to another manufacturing process for post-processing (i.e., machining process, electrochemical polishing, among others), or to continue the process plan.

Some articles have reported the specific times for some of the previous activities and are shown in Table 1. The measured times for the below case of study are included to compare them with the literature. For UPLCI, since it is a methodology dedicated to production mode, the first two steps *Generation of laser strategy* and *set-up by the operator* are included to have the overall times and processing for this process. Since usually, the production in MAM is for customized and complex projects; these two activities will be necessary for each build to maximize productivity. In addition, both activities are performed automatically in some machines, therefore they vary depending on the specific automatic set up activities of the SLM system. Typical values of averaged power during these two steps are presented below.

*Table 2-1. Time study for SLM operations from the case study and the literature.*

<b>Application</b>	<b>Time</b>	<b>Time [Reference]</b>
Generation of laser code	0.5-1h	0.25 h [18]
Set-up (operator)	0.16 h	n/a
Warm up time	0.35 h	0.5 h [18], 0.5h[9], 0.65h [4], 0.48h [5]
Processing time	3.74 h	n/a
Cooling / Cleaning time	0.08h / 1 h	0.6h [5], 2-3.5 h [19] / -
Post-Processing	0.5 h	0.1 h [18]

Figure 2.5 presents three power levels and times (basic, idle, active energy). Additional times of preset-up of the machine and cleaning times are added to the process. The time per part is consistent if the machine is used for the production of the same part. Each power level is represented in Figure 2.6. All time and power are estimated by using references from the literature.

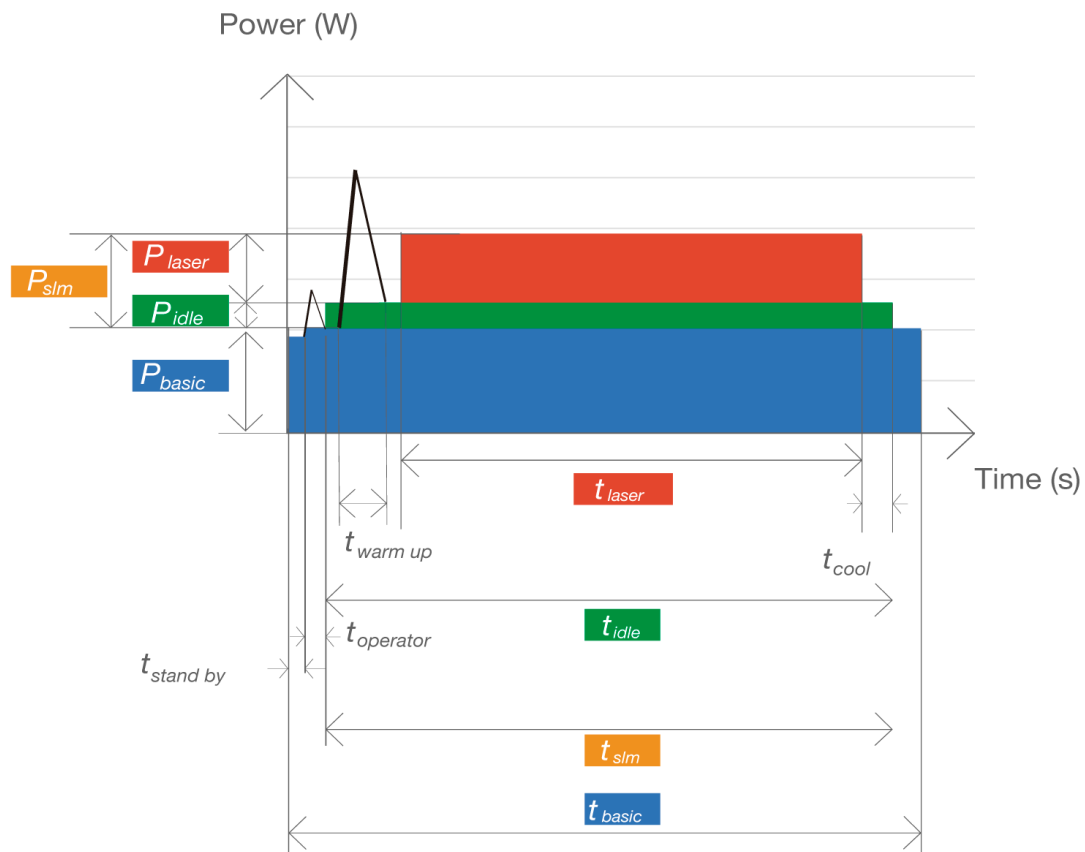


Figure 2.5. Generic power and time profile in SLM with energy as the area under the power-time graphs as shown.

The system boundaries are set to include only the active use of the SLM machine, without including maintenance, the cleaning of the machine, and the powders disposal. In addition, the operation of the SLM machine is isolated, without the influence of other elements of the manufacturing system such as material handling, and post-processing.

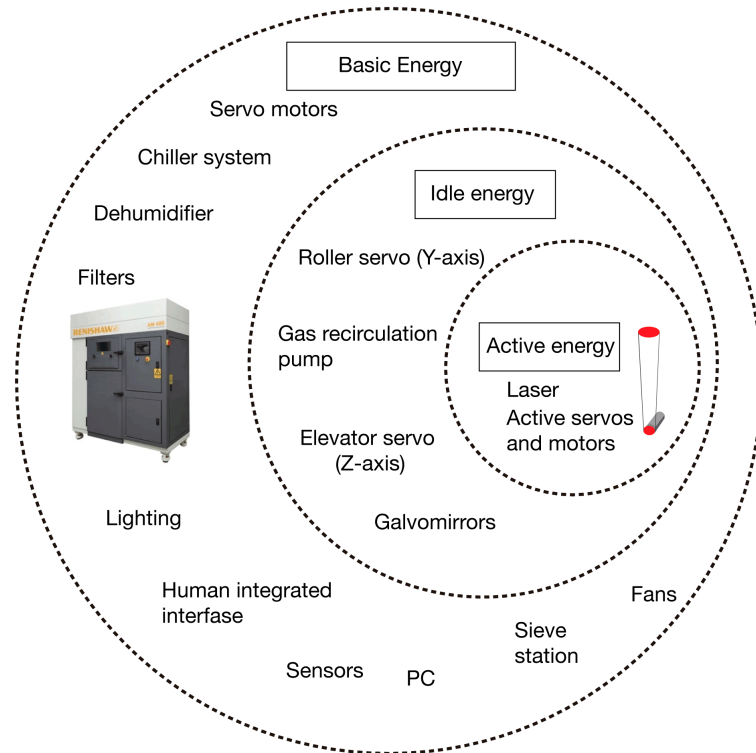


Figure 2.6. System boundary of the SLM process

## 2.2 Parameters Affecting the Energy Consumed for Selective Laser Melting

Selective Laser Melting can be analyzed by many variables. The most important are ranked as follows from most important to least important\*:

1. Powder type and particle size
2. Laser power
3. Laser scanning strategy
4. Laser speed (Point distance, Exposure time)
5. Hatch Distance
6. Layer thickness
7. Spot size diameter
8. Number of layers
9. Fine-tuning parameters (number of borders, number of fill contours, upskin and downskin)
10. Geometry and set-up
11. Support material

\*Importance was given to parameters based on the result in terms of the product integrity. Also, the influence on the surface quality and mechanical properties was taken into consideration.

## 2.3 Energy through the SLM process.

From UPLCI methodology, the total energy consumption calculations of SLM per part can be adapted from the following equation (Eq. 1). Where, according to Figure 2.6, three important stages are presented: the basic, idle and active energy which will be further discussed below.

$$E_{TOTAL} = E_{BASIC} + E_{IDLE} + E_{ACTIVE} \quad Eq. 1$$

### 2.3.1 Active energy

Process top parameters of the SLM process are presented in Figure 2.7. There are two basic UPLCI approaches for active energy. The first one, from the literature and expressed in Equation 2, provides the volumetric energy density, which is the result of the most important process variables listed before; laser power, laser speed, layer thickness, and hatch distance. Volumetric energy density (*VED*) values are in a range of 30-104.52  $\frac{J}{mm^3}$  (Table 2-2) for stainless steel 316L according to the literature review. Table 2-2 presents a literature review of the volumetric energy density for different materials.

For the calculation of *VED*, equation 1 considers all the top parameters,

$$VED = \frac{P \times ET}{PD \times LT \times HD} = \frac{P}{v_s \times LT \times HD} \quad Eq. 2$$

where the volumetric energy density (*VED*) is given in  $\frac{J}{mm^3}$ .

- *HD* is the hatch distance given in *mm*
- *P* is the laser power used in *W*
- *ET* is the exposure time and is given in  $\mu m$ ;
- and *PD* and *LT* are given in  $\mu m$ .



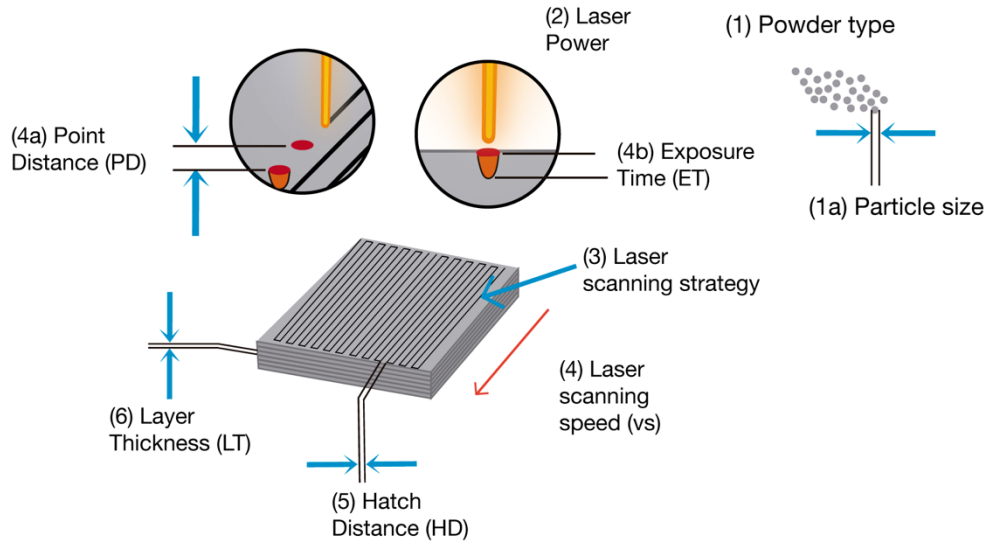


Figure 2.7. Top variables for SLM.

Equation 3 presents the energy to produce the part, including supports, so with this calculation energy consumption of the laser system can be estimated with the *VED* and volume of the part.

$$E_{laser} = VED \times Vol_{slm} \quad \text{Eq. 3}$$

and  $Vol_{slm}$  comes from equation 4,

$$Vol_{slm} = Vol_{part} + Vol_{support} \quad \text{Eq. 4}$$

where

- $Vol_{part}$  is the volume of the part in  $mm^3$
- $Vol_{support}$  is the volume of the support material in  $mm^3$

The laser energy can be calculated with the geometry and volume of the part, material properties (Table 2), and processing parameters (Table 3).

Table 2-2. Volumetric energy density for different materials.

Material	Study	VED (J/mm <sup>3</sup> )	Reference
Stainless steel, 316L	Porosity and Hardness Test	30-80	[20]
	Part density	104.52	[21]
	Tensile Test, Hardness Test	62	[22]
	Density, Tensile Test, Surface quality	40-90	[23]

		Roughness, Tensile Test	56.67	[24]
		Density, Microstructure	55-60	[25]
		Density, Hardness, Microstructure	75	[26]
		Density, Microhardness	120-190	[27]
	Ti6AlV4	Porosity and density	117	[28]
		Residual stresses, Roughness, Porosity	116.7	[29]
		Roughness, Tensile Test, Microstructure	195	[30]
		Roughness, Tensile Test, Microstructure	85	[30]
	Co-Cr	Hardness, Compression, and Tensile Tests	180 (out), 75 (in)	[31]
	Aluminum, AlSi10Mg alloy	Porosity, Tensile Test	60	[32]
	Inconel 625	Tensile Test, Fatigue Test, Porosity, Roughness	93.6	[33]

Table 2-3. Processing parameters for stainless steel 316L.

Material	Particle Size	P(W)	$v_s$ (mm/s)	SS (mm)	HD ( $\mu\text{m}$ )	LT ( $\mu\text{m}$ )	Strategy	SLM machine	Reference
	-	200	750-1000	0.07	110	50	mender	Renishaw AM250	[20]
	15-45	180	400*	0.07	124	50	meander	Renishaw AM250	[21]
Stainless steel, 316L	15-40	200	1600	-	-	50	chessboard	Concept Laser M2	[34]
	15-45	200	715*	0.05	90	50	-	Renishaw SLM 125	[22]
	22	90	160	-	-	75	meander*	Realizer 250 SLM	[23]
	15-45	170	1000	0.075	60	50	meander	Renishaw AM400	[24]

The other approach for addressing the active energy manages the power and time relationship in megajoules (MJ) during the laser scanning process as it is shown in and Figure 2.7 and Equation 6, and what later will be named as demanded energy. A few works shown in Table 4 used this approach and reported the energy consumed in MJ during the SLM process with different metal alloys. In this table, all the previous stages of the SLM process mentioned in section 2.2 are included. Some authors measured the standby, the peripheral, and the post processing energy consumed, but not listed or declared them as part of the basic, idle or active energy, so values were collocated to fix the UPLCI methodology.

### Time

The time for the fabrication of the part during the laser scanning is dependent on the following mechanisms: the Y-axis (roller) and Z-axis moving, and the time when the laser is actively melting the material (Equation 5).

$$t_{SLM} = \sum_0^n t_{zaxis} + \sum_0^{2n} t_{roller (y axis)} + \sum_0^n t_{laser scanning} \quad Eq. 5$$

### Power

During the process,  $P_{SLM}$  is averaged and multiplied by the  $t_{SLM}$  and thus obtaining the energy demanded by the machine when the laser was active (see Equation 6).

$$E_{SLM} = P_{SLM} \times t_{SLM} \quad Eq. 6$$

where the average of the SLM energy  $E_{SLM}$  is given in *MJ*.

- $P_{SLM}$  is the average power during the process given in watts
- $t_{SLM}$  is given in minutes

Thereby, from the two forms for calculating the active energy for SLM, the first one is thus based on the workpiece material being processed, processing parameters and the volume added and the supports for the part, but not considering the active actuators. In the second form, the demanded energy from the system,  $E_{SLM}$ , includes the  $E_{laser}$ , active actuators, and idle sensors and actuators. Nevertheless, in the approaches explained above, some values of the Idle Energy  $E_{IDLE}$  are not taken into account and need to be addressed in a more complete assessment.

Table 2-4. Energy consumed through different stages of the SLM process.

Part / Material	Energy Consumption							Post Processing (MJ)	Reference
	Basic			Idle		Active	Total		
	Set Up (MJ)	Stand by (MJ)	Periphe ral (MJ)	Warm up (MJ)	Cooling (MJ)	Active (MJ)	SLM total (MJ)		
Single part Build (S 316L)	-	-	-	-	-	111.60	111.60*	-	[10]
Full build experiment (SS 316L)	-	-	-	-	-	139.50	139.50*	-	[10]
Full build experiment (SS 316L)	-	-	-	-	-	96.82	96.82	-	[9]
Single bearing block (SS 17-4PH)	-	-	-	-	-	222.13	222.13	-	[12, 13]
Single turbine wheel (SS 17-4PH)	-	-	-	-	-	66.80	66.80	-	[12, 13]
Full build experiment (SS 17-4PH)	-	-	-	-	-	879.73	879.73	-	[12, 13]
Single part build (Aluminum)	-	1.34**	31.5**	2.88 [8.02%]	6.19 [17.25%]	26.81 [74.72%]	35.88 MJ [100%]	33.45	[4]***

Full build experiment (Aluminum)	-	1.34**	141.31**	2.11 [0.08%	6.23 [2.45%	245 [96.70%	253.34 [100%	142.46	[4]***
----------------------------------	---	--------	----------	-------------	-------------	-------------	--------------	--------	--------

\*The total energy is given in MJ/per Kg

\*\* Values of energy mentioned in the reference, but not included in the sum of energy consumed.

\*\*\* Breakdown of energy consumed in different stages.

### 2.3.2 Idle Energy

The idle energy consists of all the accessory parts of the machine requiring energy when the machine is not in standby mode. Idle power,  $P_{IDLE}$ , are listed in Figure 7. To calculate the idle energy, the idle time,  $t_{idle}$  (s), which is the sum of time when the machine is active from the warm-up to the cooling of the fabricated parts, including the time when the laser is scanning the layers. The sum of all idle times is presented in Equation 7.

$$t_{idle} = t_{warm\ up} + t_{SLM} + t_{cooling} \quad Eq. 7$$

The idle energy for a single feature is calculated using Equation 8,

$$E_{IDLE} = E_{warm\ up} + E_{SLM} + E_{cooling} \quad Eq. 8$$

It can be also represented by the average of the power during the specific times of each step (Equation 9),

$$E_{IDLE} = P_{warm\ up} \times t_{warm\ up} + P_{slm} \times t_{slm} + P_{cooling} \times t_{cooling} \quad Eq. 9$$

where  $P_{slm}$  and  $t_{slm}$  are referring to the idle energy measured when the laser is scanning the powder. The other two components of the equation consider the energy consumption during the warmup and the cooling stages; both averaging the power during their specific time.

### 2.3.3 Basic Energy

The basic energy includes the consumption of energy of the elements inside or outside of the machine. These elements can consume energy even when the machine is not running in production. Some of the peripheral elements are listed in Figure 2.6. The basic energy is generated by the servomotors, lighting devices, numerical control, human-machine interaction devices, and equipment attached to the machine (the chiller, dehumidifier or the sieve station). Although some of them are not operating (i.e., fume pump, galvanometric mirrors, servo motors), they are running at no-load power consumption. In contrast, the chiller and the humidifier are running at the same time in which the energy consumption is required for their operation. From Figure 2.5, the basic time is the time required for the process, and it can be represented in the following equation:

$$t_{basic} = t_{stand\ by} + t_{set\ up} + t_{idle} \quad Eq. 10$$

The basic time (in minutes) comprehends all the time required to produce a part in the machine since it is turned on until the part is cooled and ready to be taken from the building chamber, covering the time for set-up and the idle time.

The peripheral equipment considered for this paper are the sieve station, the chiller, and the dehumidifier. For the calculation of the peripheral energy  $E_{peripheral}$  (MJ), the average power consumption of each one of external equipment is multiplied by the active time when the equipment is working (Equation 11).

$$E_{peripheral} = E_{chiller} + E_{dehumidifier} + E_{sieve} \quad Eq. 11$$

Thus the basic energy,  $E_{basic}$ , is given by equation 12, where  $E_{standby}$  contains the basic energy consumption when the machine is turned on without any operation,  $E_{setup}$  is the energy needed to calibrate and set up the machine by the operator. Both are calculated by the average of power,  $P_{standby}, P_{setup}$  during the specific time ( $t_{standby}, t_{setup}$ ) of those steps.  $E_{peripheral}$  is obtained from equation 11.

$$E_{basic} = E_{standby} + E_{setup} + E_{peripheral} \quad Eq. 12$$

### 2.3.4 Summary on Unit Process Life Cycle Energy

The following information is used for the estimation of the unit process life-cycle energy for Selective Laser Melting:

1. Part material being manufactured.
2. Part and supports volume.
3. Equations and tables presented above.

## 2.4 Method of Quantification for Mass Loss

In SLM, the mass loss is being analyzed through the process performance measurements (Table 5).

Table 2-5. Waste streams in SLM.

Type of waste streams		Selective Laser Melting
Waste streams	Gas	<ul style="list-style-type: none"> <li>• Inert gas</li> </ul>
	Solid	<ul style="list-style-type: none"> <li>• Powder</li> <li>• Support material</li> </ul>

### 2.4.1 LCI for Material Mass Loss Calculations

After the SLM process is concluded, the powder is collected and stored in metal containers for filtering. The powder which not passes through the sieve is called powder waste ( $m_{powderwaste}$ ), and is a part of the mass loss ( $m_{loss}$ ) because it cannot be recycled. Therefore, the calculation of the powder waste comes from the multiplication of the mass sieved, the amount of powder not recycled, and the number of times the powder is sieved. Besides, the support material ( $m_{supports}$ ), which is removed after taking out the parts from the building plate is also part of the losses of material ( $m_{loss}$ ). The support material ( $m_{supports}$ ) can be determined by the multiplication of the  $Vol_{support}$  and the density of the support material ( $\rho_{support}$ ) as expressed in Equation 13.

$$m_{support} = Vol_{support} \times \rho_{support} \quad Eq. 13$$

The powder waste  $m_{powder waste}$ , a product of the sieving of the used powder, is the product of the multiplication expressed in Equation 14:

$$m_{powder waste} = 0.75 \times m_{sieved} \times n \quad Eq. 14$$

where  $m_{sieved}$  is mass input to the sieve station,  $n$  is number of times, and 0.75 is the percentage of loss powder in the sieve station according to the literature [35].

Consequently, the mass loss ( $m_{loss}$ ) during the SLM process will be the sum of the powder waste and the mass of the support material.

$$m_{loss} = m_{support} + m_{powderwaste} \quad Eq. 15$$

### 2.4.2 LCI for Inert Gas Loss Calculations

For enabling the SLM process, the inert gas is necessary for producing a safe atmosphere of low oxygen within the building chamber; also, it can be useful to avoid the corrosion and oxidation of the fabricated parts. Common inert gases for SLM are helium, argon, and nitrogen [36]. The inert gas is pumped through the system during the process in constant circulation; then it is filtered and released to the room when the process chamber is opened.

The consumption of argon % loss can be measured by the difference between the argon tank  $P_{in}$  at the beginning and end of the process  $P_{out}$  divided by  $P_{tank}$ .

$$\% \text{ loss} = (P_{in} - P_{out})/P_{tank} \quad \text{Eq. 16}$$

The inert gas is filtered and reused when the SLM machine is processing material, in the meanwhile, the machine uses a constant flow during each fabrication cycle.

### 3. Case Study on SLM

In this report, we analyze the detailed energy consumption calculations in the production of a tibia implant using an SLM machine model Renishaw AM400. The relevant machine specifications are listed in table 6.

*Table 2-6. Specifications of a Renishaw 400 SLM system.*

Machine type	Renishaw 400
Maximum build envelope (X × Y × Z)	248 mm × 248 mm × 285 mm
Minimum pressure in chambers (vacuum)	950 mbar-gauge or 5 kPa (-13.8 psi)
Working pressure in chamber (overpressure)	10 to 20 mbar-gauge or 101 to 202 kPa (0.15 to 0.30 psi)
Power supply	220 V to 240 V, 16 A, 45 to 60 Hz, single phase
Chilled water connection	From chiller
Argon gas supply connection	3/8 in BSP male cone fitting
Dry air supply – AM400 only	10 mm diameter pneumatic tube to air drier, 6 mm diameter from drier to AM400. 1.6 bar to 2.4 bar (23 psi to 35 psi) minimum flow of 10 l/min (0.35 ft <sup>3</sup> )
Running argon consumption (after initial fill)	10 L/hr. to 50 L/hr. (0.4 to 1.8 ft <sup>3</sup> /hr.)
Filling / purge consumption	600 L to 1 500 L (21 ft <sup>3</sup> to 53 ft <sup>3</sup> )
Argon quality (greatest permissible impurities)	20 ppm or better (99.998% pure)

#### 3.1 Product Details:

A tibia implant is considered for this case study to present a well-defined product related with AM real applications. The part has the following dimensions 32.71 × 21.23 × 190 mm and other specifications are included in Table 7. The objective of the study is to analyze the energy consumption from the production of the part with the supports.

*Table 2-7. Specifications of the implant.*

Number of test specimens included	1
Mass per part	60.32 gr
Volume deposited	2,029,630 mm <sup>3</sup>
Part volume	6,968 mm <sup>3</sup>
Supports volume	572 mm <sup>3</sup>
Total volume of fabrication	7,540 mm <sup>3</sup>

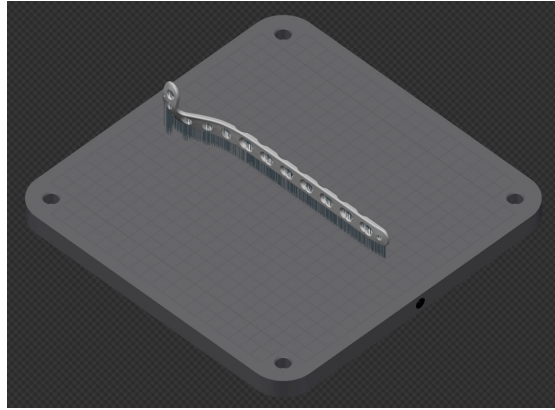


Figure 2.8. Tibia fixation plate

### 3.2 Processing parameters

The process parameters and material specifications are listed in Table 8.

Table 2-8. Processing parameters for the case of study.

Material Properties	
Part material	Stainless steel 316L
Density	4.4 g/cm <sup>3</sup> [tap density] 5.1 g/cm <sup>3</sup> [apparent density]
Particle size	45 ± 15 μm
Volumetric parameters	
Layer Thickness ( <i>LT</i> )	0.05 mm
Number of layers ( <i>n</i> )	660
Laser parameters	
Laser scanning strategy	quad islands [chessboard]
Stripe size	5 mm
Laser Power ( <i>P</i> )	170 W
Exposure Time ( <i>ET</i> )	20 μm
Point Distance ( <i>PD</i> )	20 μm
Exposure Time ( <i>ET</i> )	80 μm
Point Distance ( <i>ET</i> )	80 μm
Laser speed ( <i>v<sub>s</sub></i> )	1000 m/s
Fine tuning parameters	
Border ( <i>B</i> )	1
Fill Contours ( <i>FC</i> )	1
Hatching distance ( <i>HD</i> )	0.06 mm
Rotation Angle	67°
Initial angle	0°
Hatch offset	0.03 mm
Border distance	0.03 mm
Beam Compensation	0.0225 mm



Focus	0
Fill contour distance	0.06 mm
Fill contour offset	0.06 mm

### 3.3 SLM process

The laser strategy selected for the fabrication of this product was quad island (meander) where the laser is divided into small squares and fills the area in a different order. In Figure 2.9, the implant is shown with their supports (Fig 10a), and the laser strategy filling the quad islands in a specific order (filling, upskin filling, contours, borders, upskin border) (Fig 10d-i). Processing parameters for the fabrication of the implant are shown in Table 7.

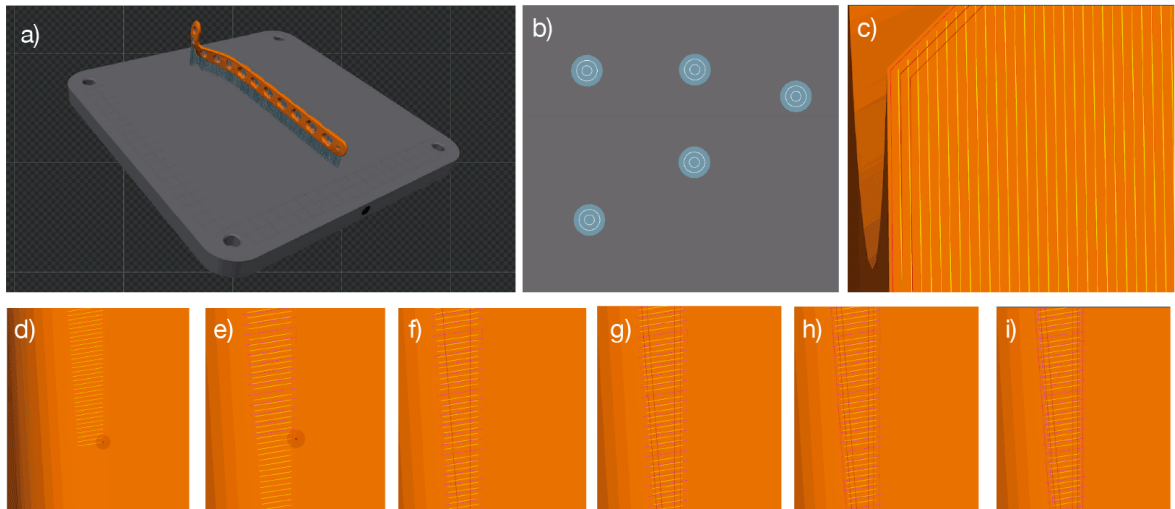


Figure 2.9. Laser strategy and (b) supports system, (c) laser strategy, (d) filling, (e) upskin filling, (f) fill contour 1 (g) fill contour 2, (h) border, (i) upskin border

### 3.4 Time and Energy calculations

The power was quantified through time using an energy logger model Fluke 1732 (Fluke Corporation, Everett, WA, USA). The data was analyzed and identified in Fluke Energy Analyze Plus Software. The time breakdown of the schematics presented in Figure 2.5 (generic power and time profiles) are presented in the same form for the case study in Figure 2.10. The power averages were obtained from the measurements and analyzed with the previous equations to present the LCI data.

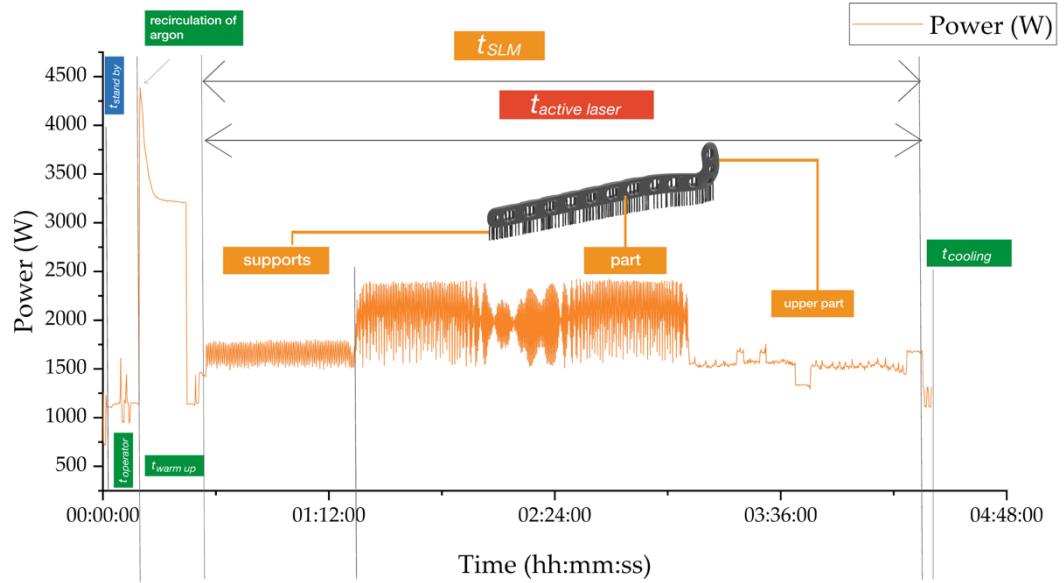


Figure 2.10. Power vs time during the SLM process.

The process can be divided into three main sections, in agreement with the energy breakdown of the generic model presented above.

#### 3.4.1 Basic energy

The basic energy is calculated with Eq. (12), but first  $E_{standby}$  and the  $E_{setup}$  are calculated from the average of power during the time of each step,

$$E_{standby} = P_{standby} \times t_{standby} = 580W \times 1\left(\frac{60s}{1min}\right) = 0.03MJ$$

$$E_{setup} = P_{setup} \times t_{setup} = 1110.2W \times 10\left(\frac{60s}{1min}\right) = 0.66M$$

The power of the peripheral equipment ( $P_{chiller}$  and the  $P_{dehumidifier}$ ) was obtained from the energy logger and is shown in Table 8 using equation 11 as follows,

$$E_{peripheral} = E_{chiller} + E_{dehumidifier} + E_{sieve}$$

Table 2-9. Peripheral equipment and their power consumption and times.

Peripheral equipment	Power (avg) (W)	Time (min)	Energy (MJ)
Chiller	2000	260	31.2
Dehumidifier	165	260	2.57
Sieve station	60	40	0.14
<b>Total</b>			<b>33.91</b>

For the calculation of the  $E_{BASIC}$ , the Equation 12 was used as follows,

$$E_{BASIC} = E_{standby} + E_{setup} + E_{peripheral} = 0.03MJ + 0.66MJ + 33.91MJ = 34.6MJ$$

### 3.4.2 Idle energy

A valid approach for estimating the idle energy is the use of the cooling energy  $E_{cooling}$  which depends on the time set to cool the parts, and the warm up energy  $E_{warmup}$ , which depends on the time spent on the preparatory functions within the building chamber. The idle energy can be calculated with Equation 8 as follows,

$$E_{IDLE} = E_{warmup} + E_{SLM} + E_{cooling}$$

In the case of the  $E_{SLM}$  component of the equation, is unfeasible to extract experimentally the portion of the amount of energy consumed by all the idle devices by separate, from the energy consumed by the devices that are part of the Active Energy (laser and servo motors). Therefore  $E_{SLM}$  was neglected in the Idle Energy calculations and was taken into consideration only for the Active Energy. The resulting calculations are shown in Table 9.

Table 2-10. Stages of the idle energy

Stage	Power (avg) (W)	Time (min)	Energy (MJ)
Warm up	2753	21	3.46
Cooling	1507	5	0.45

Idle time was calculated using Equation 7, including the idle time of the laser and servo motors, in addition to the idle time of all other non-active actuators and sensors.

$$t_{idle} = t_{warm\ up} + t_{SLM} + t_{cooling}$$

$$t_{idle} = 21\ min + 223\ min + 5\ min = 249\ min$$

Finally, from the results shown in Table 9, the  $E_{IDLE}$  is calculated as follows (where  $E_{SLM}$  is considered in the Active Energy).

$$E_{IDLE} = 3.46 \text{ MJ} + 0.45 \text{ MJ} = 3.91 \text{ MJ}$$

### 3.4.3 Active energy

Active energy was calculated from the measurements of the power consumed by the laser and the servo motors during the SLM process. For this calculation, the time can be obtained from Equation 6, and the laser scanning time for each layer can be extracted from the software according to the parameters selected. For this case study, the time was obtained during the whole fabrication cycle and is calculated as follows.

$$t_{SLM} = \sum_0^n t_{zaxis} + \sum_0^{2n} t_{roller (y axis)} + \sum_0^n t_{laser scanning} = 223 \text{ min}$$

where  $n$  was the number of layers (660 in total).

The demanded power during the AM process ( $P_{SLM}$ ) was averaged from 1,357 measurements made with the energy logger through time in intervals of 10 seconds in  $t_{SLM}$ . With the previous data,  $E_{SLM}$  was obtained by using Equation 6 as follows,

$$P_{SLMavg} = 1807 \text{ W}$$

$$E_{SLM} = P_{SLMavg} \times t_{SLM} = 1807 \text{ W} \times 223 \left( \frac{60 \text{ s}}{1 \text{ min}} \right) = 24.17 \text{ MJ}$$

### 3.4.4 Volumetric energy density (VED)

The  $E_{laser}$  can be theoretically calculated according to the volumetric energy density principle (Equations 2 and 3), and the amount of volume melted, estimated with the parameters shown in Table 7.

$$VED = \frac{P}{v_{scan} \times LT \times HD} = \frac{170 \text{ W}}{1000 \frac{\text{mm}}{\text{s}} \times 0.05 \text{ mm} \times 0.06 \text{ mm}} = 56.67 \frac{\text{J}}{\text{mm}^3}$$

$$E_{laser} = 56.67 \frac{\text{J}}{\text{mm}^3} \times 7540 \text{ mm}^3 = 0.4272 \text{ MJ}$$

By subtracting the  $E_{laser}$  and measuring the active actuators consumption of energy from the  $E_{SLM}$ , the  $E_{idle}$  and  $E_{active}$  can be estimated with a higher level of accuracy. Nevertheless, as it was stated before, these estimations are infeasible without specialized equipment, due to the difficulty in separating the energy consumption of each device involved in the process (Galvanomirror, servo motors, and other actuators).

### 3.4.5 Total energy

The total energy is estimated using Equation 1 and considering all the parameters and calculations explained above. The fabricated product is shown in Figure 2.11, and the result is expressed as follows:

$$E_{TOTAL} = E_{BASIC} + E_{IDLE} + E_{SLM(avg)}$$

$$E_{TOTAL} = 34.6 \text{ MJ} + 3.91 \text{ MJ} + 24.17 \text{ MJ} = 62.68 \text{ MJ}$$

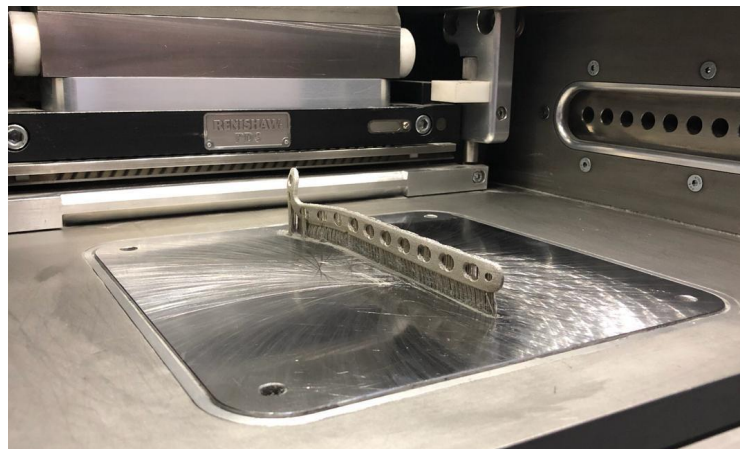


Figure 2.11. Implant with support.

## 3.6 LCI mass loss calculations

### 3.6.1 Inert gas loss calculations

For the calculation of the percentage of gas used during the process, the Equation 16 is required, where % loss is obtained from the difference of pressure at the beginning and at the end of the process and considering the tank used.

$$\%loss = \frac{(P_{in} - P_{out})}{P_{tank}}$$

$$\%loss = (2300 \text{ psi} - 1900 \text{ psi}) = 400 \frac{\text{psi}}{2600} \text{ psi} = 15.38\%$$

### 3.6.2 Material gas loss calculations

For the calculation of the mass losses, Equations 13-15 and Table 7 will be required.

$$Vol_{slm} = Vol_{part} + Vol_{support} = 6968 \text{ mm}^3 + 572 \text{ mm}^3 = 7540 \text{ mm}^3$$

By using the  $\rho_{support}$  from the supplier, the  $m_{support}$  can be determined,

$$m_{support} = Vol_{support} \times \rho_{support} = 0.572 \text{ cm}^3 \times 8 \frac{\text{gr}}{\text{cm}^3} = 4.576 \text{ gr}$$

The total mass loss of this AM process can be estimated with the following calculations,

$$m_{loss} = m_{support} + m_{powder\ waste} = 4.576 \text{ gr} + 0.0075 (10\text{kg}) \times 4 = 5.276 \text{ gr}$$

Losses during the handling of the powder during the process due to the operator are not taken into consideration.

## 4. Conclusions

This research paper presented the application of the unit process life cycle methodology (UPLCI) in Selective Laser Melting, using the calculation of the energy consumed through the process, and the mass and the inert gas losses. The energy was divided for its analysis in active, idle, and basic energies, and later analyzed in the different stages of the process.

Summarizing, UPLCI for SLM can be estimated with the following information:

- The material of the part with the parameters chosen for its production.
- The volume of the part.
- Specifications of the laser system and the machine and its peripheral equipment.
- The real time recording of the energy demands during the fabrication of a part.
- The equations explained in the previous sections, related with power and time consumption during the process.

In the case study presented in this article, a tibia fixation plate was successfully fabricated, and monitored through all the process, from the time in which the operator starts the calibration until the end of the fabrication with a total energy consumption of 62.68MJ. Peripheral equipment such as the chiller can consume more energy than the machine during the selective melting of the part. A small amount of mass losses proved the advantage of using these AM technologies for the fabrication of parts. By using UPLCI, users can improve the energy

consumption of the process and monitor all the inputs and outputs of the process. In addition, it will contribute to the best practices for the use of this technology.

## Future works

The analysis of the energy consumed by the laser and active actuators during the process can be helpful to know the right amount of active and idle energy consumed during the process. In addition, further studies on the efficiency of lasers can provide a better understanding of the proper parameters of each machine and provide a global standard for replicable productions with different machines.

## References

1. ASTM International (2015) ASTM52900-15. Standard Terminology for Additive Manufacturing--General Principles--Terminology. West Conshohocken, PA
2. Terry T., Campbell, Ian, Diegel, Olaf, Kowen, Joseph (2018) Wohlers Report 2018. Wohlers Associates, Inc.
3. Tanchev L (2007) Virtual and Rapid Manufacturing: Advanced Research in Virtual and Rapid Prototyping. CRC Press, London
4. Faludi J, Baumers M, Maskery I, Hague R (2017) Environmental Impacts of Selective Laser Melting: Do Printer, Powder, Or Power Dominate? *Journal of Industrial Ecology* 21:S144–S156
5. Liu ZY, Li C, Fang XY, Guo YB (2018) Energy Consumption in Additive Manufacturing of Metal Parts. *Procedia Manufacturing* 26:834–845
6. Cerdas F, Juraschek M, Thiede S, Herrmann C (2017) Life Cycle Assessment of 3D Printed Products in a Distributed Manufacturing System. *J Ind Ecol* 21:S80–S93
7. Telenko C, Seepersad CC (2012) A comparison of the energy efficiency of selective laser sintering and injection molding of nylon parts. *Rapid Prototyping Journal* 18:472–481
8. Torres-Carrillo S, Siller HR, Vila C, et al (2019) Environmental analysis of selective laser melting in the manufacturing of aeronautical turbine blades. *J Clean Prod* 119068
9. Kellens K, Yasa E, Renaldi R, et al (2011) Energy and resource efficiency of SLS/SLM processes (keynote paper). In: SFF Symposium 2011. pp 1–16
10. Baumers M, Tuck C, Hague R, et al (2010) A Comparative Study of Metallic Additive Manufacturing Power Consumption. In: SOLID FREEFORM FABRICATION PROCEEDINGS. University of Texas, pp 278–288
11. Paul R, Anand S (2015) A combined energy and error optimization method for metal powder based additive manufacturing processes. *Rapid Prototyping Journal* 21:301–312
12. Baumers M, Tuck C, Wildman R, et al (2011) Energy Inputs to Additive Manufacturing: Does Capacity Utilization Matter. In: Proceedings of the Solid Freeform Fabrication (SFF) Symposium. University of Texas, pp 30–40
13. Baumers M, Tuck C, Wildman R, et al (2013) Transparency Built-in: Energy Consumption and Cost Estimation for Additive Manufacturing. *J Ind Ecol* 17:418–431
14. Huang R, Riddle M, Graziano D, et al (2016) Energy and emissions saving potential of additive manufacturing: the case of lightweight aircraft components. *J Clean Prod* 135:1559–1570
15. Muthu SS, Savalani MM (2016) Handbook of Sustainability in Additive Manufacturing. Springer, Singapore
16. Lee H, Lim CHJ, Low MJ, et al (2017) Lasers in additive manufacturing: A review. *International Journal of Precision Engineering and Manufacturing-Green Technology* 4:307–322
17. Segura-Cardenas E, Ramirez-Cedillo EG, Sandoval-Robles JA, et al (2017) Permeability Study of Austenitic Stainless Steel Surfaces Produced by Selective Laser Melting. *Metals* 7:521
18. Rickenbacher L, Spierings A, Wegener K (2013) An integrated cost-model for selective laser melting (SLM). *Rapid Prototyping Journal* 19:208–214

19. Khorasani AM, Gibson I, Awan US, Ghaderi A (2018) The Effect of SLM Process Parameters on Density, Hardness, Tensile Strength and Surface Quality of Ti-6Al-4V. *Additive Manufacturing* 25:176–186
20. Peng T, Chen C (2018) Influence of energy density on energy demand and porosity of 316L stainless steel fabricated by selective laser melting. *International Journal of Precision Engineering and Manufacturing-Green Technology* 5:55–62
21. Cherry JA, Davies HM, Mehmood S, et al (2015) Investigation into the effect of process parameters on microstructural and physical properties of 316L stainless steel parts by selective laser melting. *Int J Adv Manuf Technol* 76:869–879
22. Ilie A, Ali H, Mumtaz K (2017) In-Built Customised Mechanical Failure of 316L Components Fabricated Using Selective Laser Melting. *Technologies* 5:9–21
23. Meier H, Haberland C (2008) Experimental studies on selective laser melting of metallic parts. *Mat-wiss u Werkstofftech* 39:665–670
24. Ramirez-Cedillo E, Sandoval-Robles JA, Ruiz-Huerta L, et al (2018) Process planning guidelines in selective laser melting for the manufacturing of stainless steel parts. *Procedia Manufacturing* 26:973–982
25. Junfeng L, Zhengying W (2017) Process Optimization and Microstructure Characterization of Ti6Al4V Manufactured by Selective Laser Melting. In: *IOP Conference Series: Materials Science and Engineering*. IOP Publishing, p 012026
26. Do DK, Li P (2016) The effect of laser energy input on the microstructure, physical and mechanical properties of Ti-6Al-4V alloys by selective laser melting. *Virtual Phys Prototyp* 11:41–47
27. Han J, Yang J, Yu H, et al (2017) Microstructure and mechanical property of selective laser melted Ti6Al4V dependence on laser energy density. *Rapid Prototyping Journal* 23:217–226
28. Kasperovich G, Haubrich J, Gussone J, Requena G (2016) Correlation between porosity and processing parameters in TiAl6V4 produced by selective laser melting. *Mater Des* 105:160–170
29. Mishurova T, Cabeza S, Artzt K, et al (2017) An Assessment of Subsurface Residual Stress Analysis in SLM Ti-6Al-4V. *Materials* 10:348–362
30. Vandenbroucke B, Kruth J (2007) Selective laser melting of biocompatible metals for rapid manufacturing of medical parts. *Rapid Prototyping Journal* 13:196–203
31. Liverani E, Fortunato A, Leardini A, et al (2016) Fabrication of Co–Cr–Mo endoprosthetic ankle devices by means of Selective Laser Melting (SLM). *Mater Des* 106:60–68
32. Read N, Wang W, Essa K, Attallah MM (2015) Selective laser melting of AlSi10Mg alloy: Process optimisation and mechanical properties development. *Mater Des* 65:417–424
33. Koutiri I, Pessard E, Peyre P, et al (2018) Influence of SLM process parameters on the surface finish, porosity rate and fatigue behavior of as-built Inconel 625 parts. *J Mater Process Technol* 255:536–546
34. Yusuf S, Chen Y, Boardman R, et al (2017) Investigation on Porosity and Microhardness of 316L Stainless Steel Fabricated by Selective Laser Melting. *Metals* 7:64
35. Sůkal J, Paloušek D, Koutny D (2018) The effect of recycling powder steel on porosity and surface roughness of SLM parts. *MM Science Journal* 12:2643–2647
36. Kruth J, Mercelis P, Vaerenbergh JV, et al (2005) Binding mechanisms in selective laser sintering and selective laser melting. *Rapid Prototyping Journal* 11:26–36



## List of symbols

$\%$ loss	percentage of loss	$P_{out}$	out pressure
$B$	border	$P_{slm}$	average power of SLM
$E_{active}$	active energy	$P_{set up}$	set up power
$E_{basic}$	basic energy	$P_{sieve}$	sieve power
$E_{idle}$	idle energy	$P_{stand by}$	stand by power
$E_{total}$	total energy	$\rho_{support}$	density of the support material
$E_{chiller}$	chiller energy	$P_{tank}$	tank pressure
$E_{cooling}$	cooling energy	$P_{warm up}$	warm up power
$E_{dehumidifier}$	dehumidifier energy	SS	spot size
$E_{laser}$	laser energy	$t_{basic}$	basic time
$E_{peripheral}$	peripheral energy	$t_{cooling}$	cooling time
$E_{set up}$	set up energy	$t_{chiller}$	chiller time
$E_{sieve}$	sieve energy	$t_{dehumidifier}$	humidifier time
$E_{stand by}$	stand by energy	$t_{idle}$	idle time
$ET$	exposure time	$t_{laser scanning}$	laser scanning time
$E_{warm up}$	warm up energy	$t_{roller}$	roller movement time
FC	fill contour	$t_{set up}$	set up time
HD	hatch distance	$t_{sieve}$	sieve time
LT	layer thickness	$t_{SLM}$	slm time
$m_{loss}$	mass loss	$t_{stand by}$	stand by time
$m_{powder waste}$	mass of the powder waste	$t_{warm up}$	warm up time
$m_{support}$	mass of the support	$t_{z axis}$	movement z-axis time
$n$	number of layers	$V_{loss}$	volume loss
$P$	power	$Vol_{part}$	part volume
$P_{chiller}$	chiller power	$Vol_{slm}$	volume of part and support
$P_{cooling}$	cooling power	$Vol_{support}$	support volume
PD	point distance	$Vol_{tank}$	tank volume
$P_{humidifier}$	humidifier power	$v_s$	laser scanning speed
$P_{in}$	initial pressure		

## Abbreviations

SLM	Selective Laser Melting
MAM	Metal Additive manufacturing
STL	Standard Tessellation Language
HMI	human-machine interface
ppm	parts per million
UPLCI	unit process life cycle inventory
LCI	life cycle inventory
EBM	electron beam melting
VED	volumetric energy density

# Chapter 3. Process planning of L-PBF of AISI 316L for improving surface quality and relating part integrity with microstructural characteristics

## Abstract:

The optimization and characterization of parts for the processing parameters calibration in laser powder bed fusion has been recently well studied in academia but still under research in the industry, due to the early adoption of this technology in different companies and research centers. Within this context, this paper proposes a process planning workflow for the obtention of calibrated ranges of parameters for AISI 316L samples, and to understand the relationship between the improved parameters, the surface quality and part integrity with the microstructural characteristics. Two principal methods of characterization, (1) Nanoindentation and Electron backscatter diffraction (EBSD) and (2) non-contact profilometry by Focus Variation, were used to validate the influence of the overlap of the point distance (PD) and hatch distance (HD) in the fabrication process. In this study, hardness and the modulus of elasticity exhibited the highest values of 4.59 GPa and 229.7 GPa respectively in the parallel orientation to the build direction. The obtained hardness and modulus of elasticity were correlated with the different grain sizes and the resulting crystallographic orientation product of the thermal history of the process. Roughness (Ra) was improved with the selection of parameters and presented the lowest value of 5.433  $\mu\text{m}$ . Finally, the microstructure was studied on the samples as the final assessment on the improved parameters where finer cellular/dendritic structures were found.

**Keywords:** *laser powder bed fusion; selective laser melting (SLM); optimization of parameters; nanoindentation; surface quality; electron backscatter diffraction; additive manufacturing*

## 1. Introduction

Laser powder bed fusion technologies (L-PBD) have been used more in recent years since machines are more affordable and the process is in continuous improvement. With the advances in the development of more efficient systems and lasers, and in situ monitoring, the productivity of L-PBF machines has increased. The Wohlers report presented that revenue from additive manufacturing (AM) metal machines grew 29.9% in 2018 to an estimated of 947.8 US million dollars [1]. Early adoption in the academy and industry has increased the research and development of final products significantly. In the academic field, according to SCOPUS database, from 1975 to 2019, a total of 5889 documents were published about L-PBF. In the last years, 2016 (624 documents), 2017 (865 documents) and 2018 (1226 documents) have been published,

increasing the scientific and industrial knowledge around this technology, where China, Germany and the US are the countries with more contributions [2]. Another growing market in AM is the powders production. Commercially available alloys commonly used for casting/powder metallurgy have been introduced to L-PBF with successful results. Significant growth of 41.9 % in 2018 of the revenue of different types of commercial alloys in a total of 260.2 US million dollars. However, some critical issues have been limiting the advantages of AM with these available materials, such as balling of the material during the process, defects produced due to the thermal history of the material (solidification cracking/hot tearing), and others [3]. Hence, the development of new alloys that can be weldable avoiding the cracking tendency, has contributed to the exponential growth in the research of this topic. Even though it is a recent technology, and there is a curve of knowledge for early adopters, with the right guidelines, workflow, documentation, and characterization, optimized parameters can be obtained. Thereby machines can be running production as some industries have reported.

To understand the basics of the processing parameters and variables that have inherent in the process is fundamental to generate workflow or process guidelines. Firstly, processing parameters have different names and nomenclatures. Figure 3.1 presents a summary of the most important and well-known processing variables and their equivalences for different machines. Laser Power (P), Layer thickness (LT), laser scanning speed (vs) and hatch distance (HD) are considered to be the most important parameters due to their impact on the integrity of the parts (Figure 3.1A) [4]. Commercial machines have different laser systems that can be programmed in different forms: pulse width modulated (PWM) and continuous (CW). When a laser is working either in PWM, it can provide processing parameters related to the pulse frequency, duration, and peak power [5]. Two of the most relevant processing parameters related to PWM, and commonly reported in the literature are the Point distance (PD) and Exposure time (ET) shown in Figure 3.1B. Since L-PBF is an AM process, where layers (n) are added continuously, process parameters such as the initial and rotation angle of layers can have an impact on the distribution of stresses in all directions [6].

The next points include relevant introductory concepts that could help the industry practitioners in understanding the importance of process calibration and its impact on mechanical behavior and surface quality. There are other concepts related to subsurface part integrity that were not taken into account in order to summarize the most relevant to adopters of this technology, looking to fabricate functional parts in conventional industry.

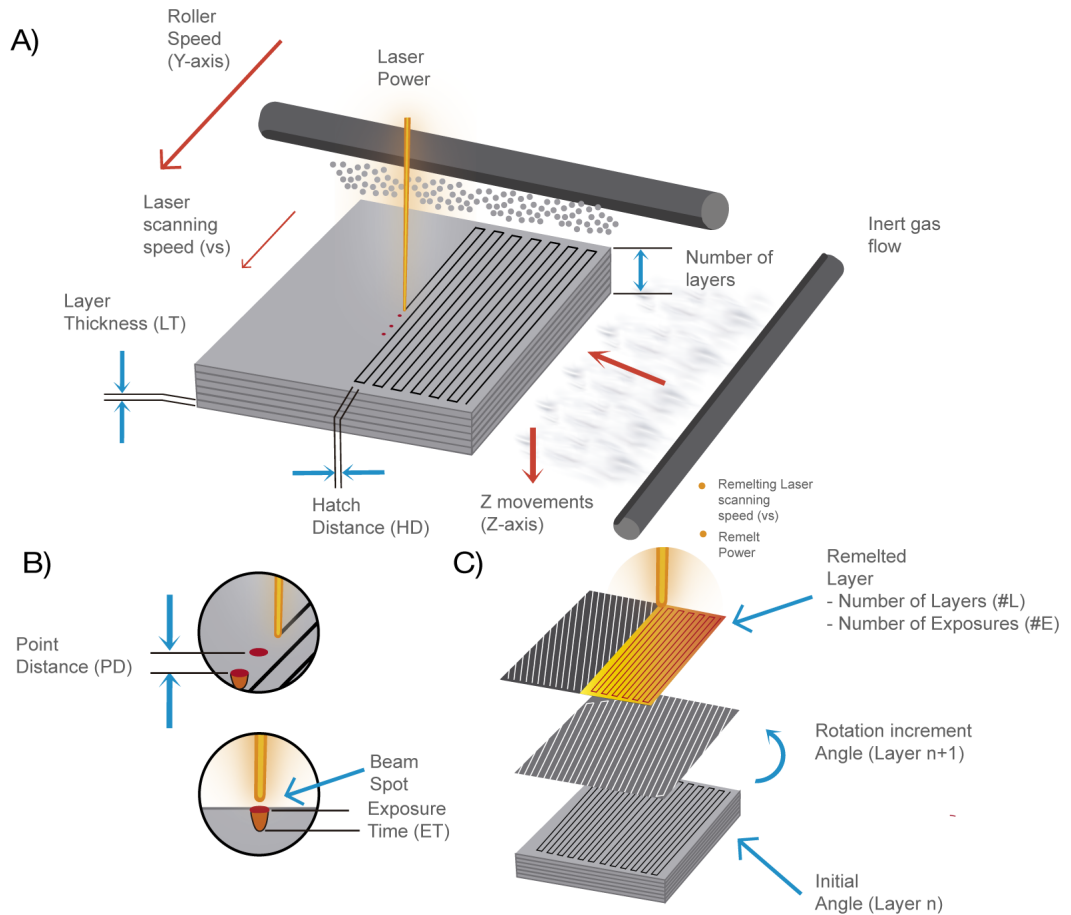


Figure 3.1. Process parameters. (a) Overview of the processing variables in the building chamber. (b) Parameters related to modulated lasers (c) Parameters related remelting and rotation angles through the part.

a) Scanning strategies

Several authors have identified different scanning strategies, and the most representative are presented in Figure 3.2. In some studies, such as Segura-Cardenas et al., the authors found that, by using the meander strategy, the surface quality was improved [7], and additionally, mechanical properties were enhanced. H. Ali et al. found that, with the chessboard scanning strategy, residual stresses were reduced and at the same time, the relative density increased due to the distribution of heat [8,9]. Concentric scanning strategy has been demonstrated to be useful in improving the geometry fidelity in small struts, stents or lattices compared to the hatching strategy (stripes) [10].

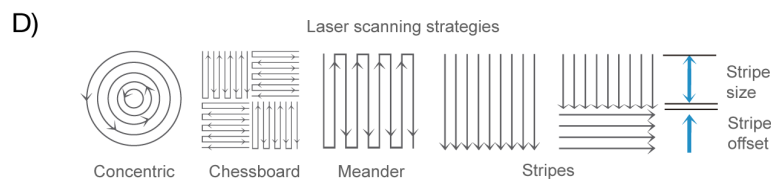


Figure 3.2. Laser scanning strategies.

The energy provided by the laser to the powder through time creates a thermal joining history in which the material is melted and cooled by each layer; therefore, mechanical properties, microstructure and surface quality varied as a result of the combination of processing parameters. The calculation of that energy input has been summarized in different dimensions: linear, areal, and volumetric [11]. Specifically, the investigation presented here addresses the calibration of L-PBF process according to Linear Energy Density (LED) and Volumetric Energy Density (VED), as explained in the following sections.

*b) Linear energy density (LED)*

Firstly, when working with engineered materials, finding the right processing parameters to obtain good weldability is fundamental. Weldability is a function of the reaction taking place in the fusion zone by a heating agent of the metal alloy, leading to the formation of a permanent monolithic welded product [12]. Weldability criteria were stated in some standards, such as in the ISO/TR 581:2005. Accordingly, selection criteria and terminology to evaluate parameters related to weldability have been adapted from [12] for L-PBF, where parameters can produce satisfactory or unsatisfactory results (see Figure 3.3). It is considered that the good/top parameters present continuous weld lines, uniform thickness and height, and no superficial defects. Some ranges of parameters can produce poor results where spatter particles and apparent high porosity appear due to unmelted powder. It is considered unsatisfactory when the following defects appear spatter particles, balling effect, and some concentrations of material with a continuous weld line, but uniformity is compromised.

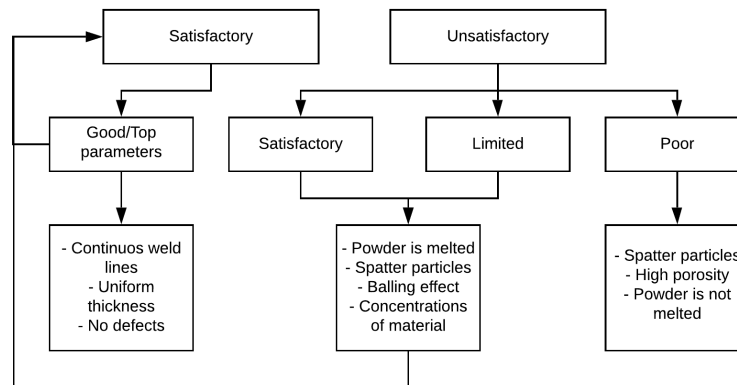


Figure 3.3. Selection criteria for best parameters, adapted from [12]

Equations as linear energy density (LED), which relates power (P) and laser scanning speed ( $vs$ ) (see Equation 1), have been used to capture the interaction between energy, linear feed, and time. Several authors, in their task to optimize processing parameters for different materials, have measured geometrical accuracy, roughness, height, and penetration of the laser, as shown in Table 1. For example, for the case of titanium alloys, Gu et al. found that by increasing the laser speed, an elevated thermal and kinetic undercooling with an associated solidification rate takes place. They found that a balling effect and thermal cracks have resulted from a low viscosity of the

material during the welding process [13]. Also, Hong et al. developed a study of welding lines with different parameters for Co-Cr commercial alloy, in which they found that the previously discussed parameters and hatch distance are key factors to determine the surface quality [14]. On the other hand, with an aluminum alloy, Wei et al. proposed a scope for processing LED values that led to continuous scan weld lines with a smooth surface in the range of 1.5-1.875 J/mm [15]. Another study characterized Inconel 718 processability using LED to prove the weldability of the material by analyzing the average melt line, width, and depth [16].

$$LED = \frac{P}{v_s} \quad (1)$$

Table 3-1. Main studies using Linear Energy Density (LED) for parameters optimization.

Material	Study	LED	Reference
Cp-Ti	Density, Microstructure, Roughness, Hardness	0.3-0.45	[13]
Ti-24Nb-4Zr-8Sn	Density, Hardness, Tensile Test	0.36	[17]
Co-Cr	Roughness, Weld lines	1.4-5.1	[14]
Aluminium, AlSi10Mg alloy	Density, Microstructure, Tensile Test	1.8	[15]
Inconel 718	Weld lines	0.21	[18]
Inconel 718	Microstructure, Hardness, Density	0.33	[16]
Inconel 625	Roughness, Weld lines	0.7	[19]

After the production of weld lines with different LED, authors have presented optimum parameters in terms of surface quality, internal porosity, and microstructure.

c) *Volumetric energy density (VED)*

In the quest to correlate parameters with the mechanical, geometric, surface, and density properties, the volumetric energy density has been widely adopted as an indicator to select the optimum range of parameters. Equation 2 is the representation of VED in terms of the previously presented most influential parameters P (watts),  $v_s$  (mm/s), LT ( $\mu\text{m}$ ), and HD ( $\mu\text{m}$ ).

$$VED = \frac{P}{v_s \times LT \times HD} \quad (2)$$

Some authors discussed if VED is a good approximation for parameter synthesis, drawing several concerns due to the lack of information about the material consideration in the VED equation [20], the lack of understanding on the main characteristics of the laser [21]; and the uncertainty in reproducibility and feasibility. Other authors made profound conclusions of why VED is a thermodynamic quantity without capturing complex physical phenomena such as the Marangoni

flow, hydrodynamic instabilities, and the recoil pressure, which have a direct impact on the consistency of the tracks [22]. Still, VED is widely used to summarize process parameters, in addition to characterization techniques such as porosity analysis, density measurements, tensile and hardness tests. Table 2 presents recent studies where authors have published range values of VED to correlate the effect of specific parameters with different part properties.

*Table 3-2. Main studies with VED for the optimization of parameters*

<b>Application</b>	<b>Study</b>	<b>VED</b>	<b>Reference</b>
Stainless steel, 316L	Porosity and Hardness Test	30-80	[23]
	Part density	104.52	[24]
	Tensile Test, Hardness Test	62	[25]
	Density, Tensile Test, Surface quality	40-90	[26]
	Roughness, Tensile Test	56.67	[27]
	Density, Microstructure	55-60	[28]
Ti6AlV4	Density, Hardness, Microstructure	75	[29]
	Density, Microhardness	120-190	[30]
	Porosity and density	117	[31]
Co-Cr	Residual stresses, Roughness, Porosity	116.7	[32]
	Roughness, Tensile Test, Microstructure	195	[33]
	Roughness, Tensile Test, Microstructure	85	[33]
	Hardness, Compression and Tensile Tests	180 (out), 75 (in)	[34]
Aluminium, AlSi10Mg alloy	Porosity, Tensile Test	60	[35]
Inconel 625	Tensile Test, Fatigue Test, Porosity, Roughness	93.6	[21]

*d) Selection of parameters in range*

Table 3 presents a literature overview of different types of ferrous, titanium, aluminum and nickel-based alloys additively manufactured with L-PBF. These works aimed to find optimum parameters ranges to obtain good mechanical and surface quality properties by using different characterization methods and process guidelines. These authors worked with different systems and varied the parameters according to the machine limitations/configurations. For example, stainless steel 316L has been reported in different ranges of VED, between 30-104 J/mm<sup>3</sup> where it can be additively manufactured [23–27], and different combinations of parameters in the following table produced optimized ranges, but in some cases very different from each other due to the L-PBF system limitations.

Table 3-3. Literature overview of the processing parameters for different materials.

Material	Particle Size ( $\mu\text{m}$ )	P (W)	VS (mm/s)	DS (mm)	HD ( $\mu\text{m}$ )	LT ( $\mu\text{m}$ )	Laser scanning Strategy	L-PBF machine	Reference
Stainless steel, 316L	-	200	750-1000	0.07	110	50	mender	Renishaw AM250	[23]
	15-45	180	400*	0.07	124	50	meander	Renishaw AM250	[24]
	15-40	200	1600	-	-	50	chessboard	Concept Laser M2	[36]
	15-45	200	715*	0.05	90	50	-	Renishaw SLM 125	[25]
	22	90	160	-	-	75	meander*	Realizer 250 SLM	[26]
	15-45	170	1000	0.075	60	50	meander	Renishaw AM400	[27]
AISI Maraging Steel	40	100	180	0,2	-	30	chessboard	SLM Machine	[37]
304L	32-46	95	70	0.2	120	30	chessboard	Concept Laser M3 Linear	[38]
	20-50	200	250	0,1	-	20	stripes	SLM system (LSNF-1)	[39]
Cp-Ti	0-45	70	400*	0.054	-	50	lines	MCP Realizer II,	[40]
	19.5-43.3	200	300	0.07	50	50	meander	SLM system (Fraunhofer LT)	[13]
Ti6AlV4	36	200	1000	0.07	80	30	meander*	DiMetal-100	[41]
	-	320	3000	-	60	30	meander*	SLM 150 Machine	[28]
	20-63	120	400	0.07	80	50	-	SLM Solutions 250	[29]
	18-40	194	800-1100	-	70-120	20	meander	SLM system (LSNF-1)	[30]
	31-53	175	400-600	-	80	30	meander*	SLM Solutions 250	[31]
	15-58	400	50	0.2	630	200	meander	Concept Laser M2	[42]
	<50	175	500	-	100	30	chessboard	SLM Solutions 280HL	[32]
	37	95	125	0.2	130	30	-	Concept Laser M3 Linear	[33]
	25-35	110	700	0.2	75	30	meander	SLM Solutions 125HL	[43]
	10.62-31.46	100	40	34	40	50	stripes	SLM Machine	[44]
-	250	1600	-	60	30	meander*	in house developed	[45]	
Ti-6Al-7Nb	8-64	100	150	0.18	100	50	meander*	SLM Realiser II	[46]
Ti-24Nb-4Zr-8Sn	45-100	200	550	0.08	-	100	linear	MTT SLM 250HL	[17]
Co-Cr	<40	200	128.6	0.08	100	50	stripes	SLM Machine PNUME	[14]
	20-50	325-350	66-88.3	0.15	-	200	-	in house developed	[47]
	-	200	700	0.075	125	30	stripes	Renishaw AM250	[48]
	50	95	200	0.2	140	40	-	Concept Laser M3 Linear	[33]
	15-45	90,126	700,1200	0.05	50, 70	20	chessboard	SISMA MYSINT100 system	[34]
	33	40	333.33	0.75	40	30	concentric	Renishaw AM250	[49]



Aluminium,AlSi10 Mg alloy	20-60	200	1400	0.15	105	30	meander, stripes	Concept Laser M1 Machine	[50]
	35	175	1025	0.15	97.5	30	chessboard	Concept Laser M2	[35]
	20-63	910	<300	0.3	700	50	chessboard	Trumpf Trumaform LF250	[51]
	20-63	350	930	0.08	190	50	chessboard	SLM Solutions 280HL	[52]
	20-63	100	500	-	50	40	meander*	Realizer Gmbh-50	[53]
	25-45	250	500	0.2	150	50	-	Trumpf Trumaform LF130	[54]
	15-30	400	1000	0.1	200	60	stripes	EOSINT M280	[55]
	0-45	180	1000	0.07	50	40	meander*	SLM 150 Machine	[15]
	20-63	350	900	-	120	100	stripes	SLM Solutions 280HL	[56]
	Inconel 718	10-45	180	600	0.15	-	30	chessboard	SLM solutions
-		350-450	300-600	-	80	40	meander	EOS M400	[58]
30		110	400	0.07	60	30	meander	SLM 150 Machine	[59]
-		285	960	0.075	110	20	lines	EOS Sint 280	[18]
15-45		130	400	0,07	-	-	-	in house developed	[16]
Inconel 625	22,5159	550	400	0.8	-	-	lines	in house developed	[19]
	34.63	160	500	0.05-0.08	60	20	meander*	HRPM II	[60]
	10-45	170-180	500-600	0.07	140	50	stripes	SLM Solutions 125HL	[21]

In the present paper, to evaluate, test, and characterize the properties of parts produced through L-PBF, the following techniques are suggested: (1) Optical profilometry through Focus Variation (FV) and (2) a combination of Nanoindentation and Electron Backscatter Diffraction (EBSD). The advantage of these two characterization techniques is that different sections of the parts can be selected, and a correct overview of the product properties of this manufacturing process can be assessed.

## 1.1 Focus Variation

Focus variation is a non-tactile profilometry technique that overcomes the small depth of focus of an optical system with scanning in a vertical direction to improve the topographical resolution and colors as a result of the variation of focus [61]. With this technique, the surface topography is created in a three dimensional form, that can be used as an alternative tool for the measurement of surface roughness, waviness and form, and being compatible with standards ISO 4287 and ISO 4288. Using this technique, some authors have studied the effect of the laser on the surface roughness [7,27,62] and found some trends explaining how the parameters affected the quality. In other work, Triantaphyllou et al. compared two L-PBF processes, SLM and EBM by using this characterization technique, and found an average surface roughness Ra of 4.8µm along and across the layers [63].

## 1.2 Nanoindentation and Electro Backscatter Diffraction

Nanoindentation is a surface mechanics method to study the localized deformation behavior at the nano and micro levels. The efficient approach of this technique to develop a fundamental understanding of the deformation mechanisms can be helpful for multi-scale modeling [64]. Anisotropic behavior of mechanical properties such as elastic modulus and hardness is a common phenomenon in some materials at the nanoindentation scale level [65], which are associated with the activation of various deformation mechanisms when the material is stressed along different crystallographic orientations [66].

To visualize the microstructure, generating a map representation of the grain boundaries is very useful to explain the grain orientation, misorientation, phase, grain size, rotation angle, and distribution of grains. For this purpose, Electron Backscatter Diffraction (EBSD) has been used in additive manufacturing to prove the anisotropy of the L-PBF process [67]. The interface between two grains in a polycrystalline material creates a grain boundary. Grain boundaries have some impacts on material properties because these boundaries are sites for the initiation of corrosion and precipitation of new phases from the solid. Grain boundaries disrupt the movement of the dislocation through a material. Hence, reducing grain size and increasing grain boundaries are ways to improve mechanical properties. With both characterization techniques, nanoindentation, and EBSD, a correlation between the crystallographic orientation and the grain size and their influence on the mechanical properties in a specific zone of the part product of the thermal history of the process can be addressed.

As all the previous works have proposed several alternatives for obtaining optimum parameters, this paper will address the topic looking to report the comparison between dimensional energy equations and defining this process with two levels, (1) by testing the two-dimensional weldability and (2) by analyzing the three dimensional fabrication of a part with a proper calibration (Figure 3.4). *Task Type 1 – Design of Experiments* is the first task where material and application must be selected, and the design of experiments for the previous two levels has to be done. In this paper, an approach of varying PD and HD will be varied to understand the influence of the overlap in the surface quality and part integrity. Afterward, the *Task Type 2 – Sample fabrication* where a number of consecutive *Builds* to prove the design of experiments is suggested. Finally, *Type 3 – Characterization and parameter selection* is presented where different characterization techniques are performed in terms of roughness, topographical characterization, nanoindentation, and a final assessment to report the microstructure of the optimum parameters. By using statistical analysis results, the importance of the parameters of these two levels was identified.

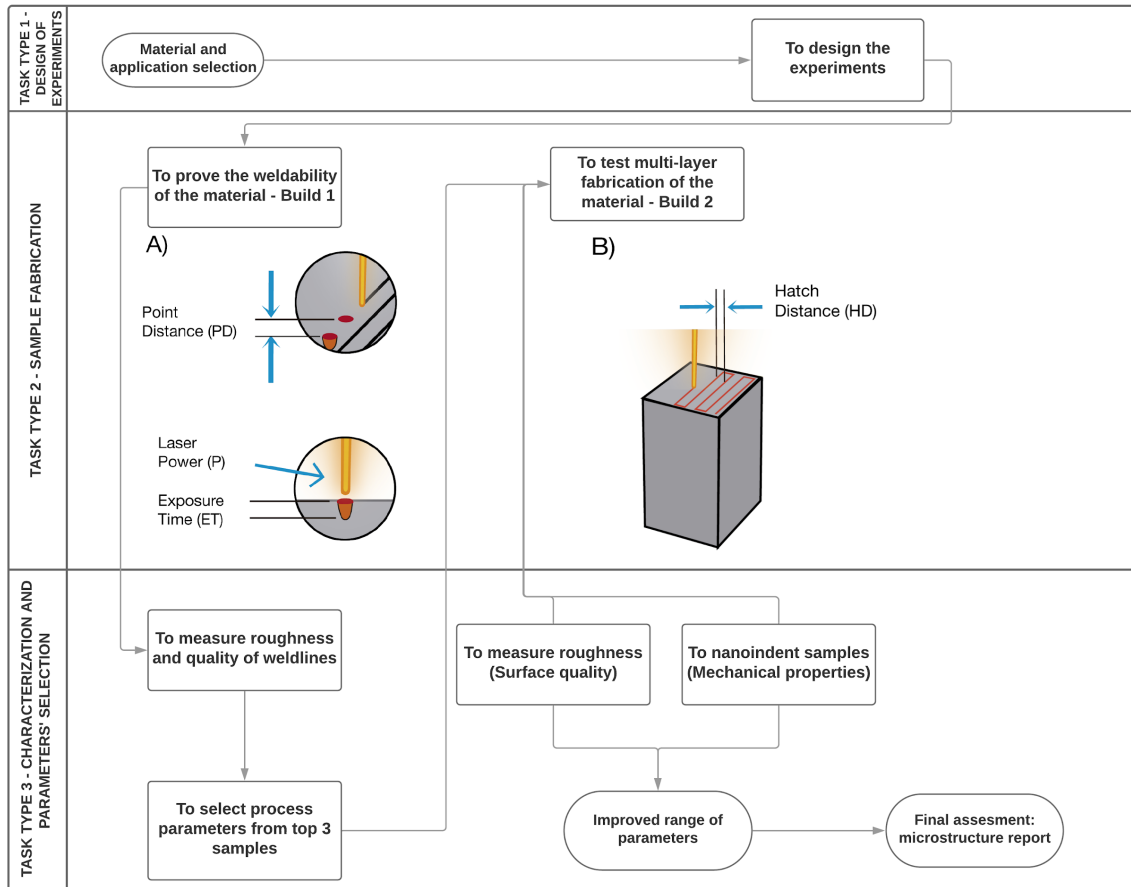


Figure 3.4 Proposed process tasks to obtain parameter ranges.

## 2. Materials and Methods

### 2.1 Materials and Experimental Set-Up

The proposed parameters optimization procedure used a laser powder bed fusion commercial machine. A Renishaw AM 400 (Renishaw, UK) with a maximum building volume of  $250 \times 250 \times 300$  mm was used for producing samples. The radiation source was a modulated laser Yb-fiber with a maximum power of  $P = 400$  W, a wavelength of  $\lambda = 1075$  nm, and a spot size calibrated at  $d = 75$   $\mu\text{m}$ .

The workflow started with the task *Materials and application selection*, in which the selected material for this study was an austenitic stainless steel (designation SS 316L-0410, Renishaw-United Kingdom) with the following composition: Fe (Bal), Cr (16-18%), Ni (10-14%), Mo (2-3%), Mn (<2%), Si N (<0.1%), O (<0.1%), P (0.045%), C (0.03%), S (0.03%). Five samples from the powder container were analyzed with an EVO MA25 ZEISS Scanning Electron Microscope (Zeiss, Jena, Germany) with an accelerating voltage of 20 kV and high vacuum. The average particle size, calculated using *ImageJ* software, presented a normal distribution (Figure 3.5), and a  $D_{90} = 42.84 \mu\text{m}$ .

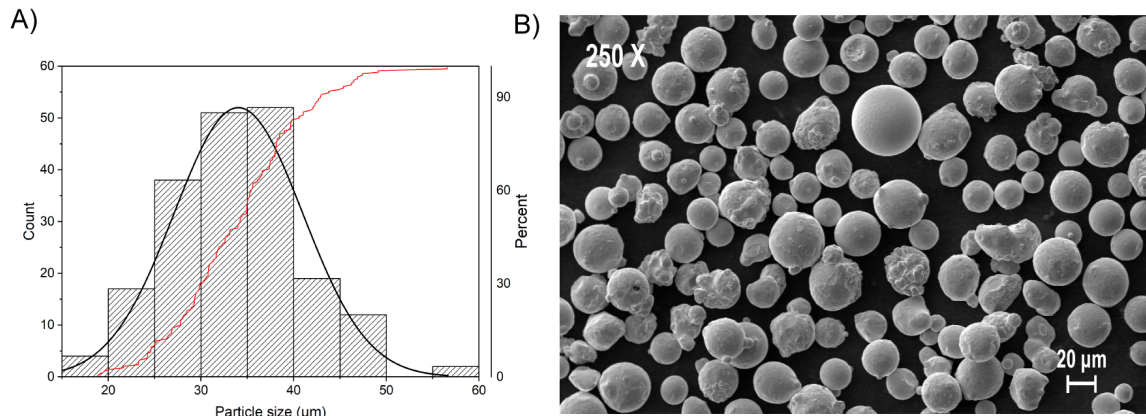


Figure 3.5 (a). Particle size distribution. (b) SEM Micrograph of stainless steel powder with  $D_{90}=42.84 \mu\text{m}$

## 2.2 Samples design

The samples were designed using SolidWorks 2018 at the two levels of experiments (SolidWorks, Dassault Systems SolidWorks Corporation, USA). The first level of testing, *Build 1*, consisted of three replicas of lines of 15 mm with 1, 3, 7 layers of height, and 75 μm of thickness in an array of  $9 \times 9$ , with a separation of 10 mm between weld lines and 15 mm from a different set of weld lines. For the second level of testing, *Build 2*, the experiment consisted in using rectangular prisms of  $10 \times 10$  mm, and 20 mm in height, with a support separation of 10 mm from the building plate, with an array of  $3 \times 3$  and 15 mm from each side.

## 2.3 Design of experiments

According to Figure 3.4, and the previously mentioned arrays, an experimental design was done by taking into consideration the parameters previously mentioned in the literature review, and some constraints for the determination of processing parameters. For this case, and according to the measurement of the particle size and with the found particle size ( $D_{90}$ ), it is recommended to use a layer thickness of 40 μm [68].

At the sample fabrication tasks, the machine was supplied with new powder, the building plate was collocated, and the roller was calibrated. Argon was circulated through the system in an inert ambient of less than 10 ppm of  $\text{O}_2$  [69]. The set of samples were sliced, and process parameters were varied using QuantAM 3.4.0. software (Renishaw, United Kingdom). The design of these two levels of experiment has the objective to prove the weldability of material by melting the powder in a straight line (1), and to verify the fabrication of multi-layer parts (2), which were named *Build 1* and *Build 2* respectively. The building plates were washed with ethyl alcohol to remove the non-melted powder.

The DoE for *Build 1* consisted of three-level experiments with triplicate welding lines were P, ET, and PD were varied. Three values of P were selected: 75, 125, and 175 W. PD was varied according to Figure 3.6 (18, 37, 57 μm), achieving a percentage of overlapping in the construction

of a weld line. The minimum value of the ET (20, 50, 80  $\mu\text{s}$ ) was set according to the laser specifications.

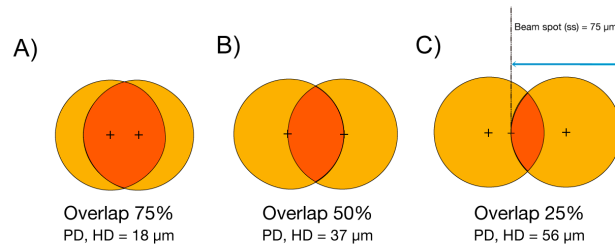


Figure 3.6. Overlapping percentages of PD and HD (a) 75%, (b) 50%, (c) 25%

The purpose of *Build 2* was to test the multilayer capacity of this alloy with the predefined processing parameters from *Build 1*. Therefore, to fabricate *Build 2*, HD and LT were set according to Table 4. HD is the distance between two weld lines and was varied, as shown in Figure 3.6, to validate if the overlapping by the proximity of two lines (25%, 50%, and 75%) can produce better properties in terms of mechanical, surface quality, and part density. After *Build 2* was manufactured, parts were mechanically removed from the building plate, were put in an ultrasonic bath for 20 minutes with distilled water and 10 minutes in acetone, and finally dried using compressed air.

Table 3-4. Processing parameters for *Build 2*.

Sample Number	Power (watts)	Exposure Time ( $\mu\text{s}$ )	Point Distance ( $\mu\text{m}$ )	Hatch Distance ( $\mu\text{m}$ )	Layer Thickness ( $\mu\text{m}$ )
1	175	50	18	18	40
2	125	80	18	18	40
3	175	80	18	18	40
4	175	50	18	37	40
5	125	80	18	37	40
6	175	80	18	37	40
7	175	50	18	56	40
8	125	80	18	56	40
9	175	80	18	56	40

During Task type 3, two types of characterization were used to find the optimum range of parameters: 1) By using a visual characterization and surface topography measurements. External

quality of the part is reported, and parameters that presented the balling effect, non-continuous weld lines, and under/over melting of the material were discarded. 2) In order to propose an assessment of the mechanical properties, microstructure analysis and nanoindentation techniques are suggested.

## 2.4 Visual Characterization and Topography characterization

Visual characterization is important because it shows on a macro level the stability of the processing parameters. For *Builds 1 and Build 2*, the criteria were defined to select the optimum parameters with the information collected firstly by a qualitative analysis, performed using a SteREO Discovery V8 microscope equipped with a CCD camera AxioCam HRC (Carl Zeiss Microimaging GmbH, Jena, Germany), and using AxioVision 4.5 software (Carl Zeiss). In order to create topography images of *Builds 1 and 2* surfaces, a non-contact 3D profilometry method was used. Additionally, the average surface roughness (Ra) was measured to determine the quality of the weld line in the parallel (PAR) and perpendicular (PERP) to the building orientation surfaces of the rectangular prisms made in *Build 2*. The surface topography data was obtained using a non-contact profilometer that works under the principle of Focus Variation, Alicona Infinite Focus microscope G4 (Alicona Imaging GmbH, Graz, Austria) with an objective of 10x, with a vertical resolution of 50  $\mu\text{m}$  and lateral resolution of 3.5  $\mu\text{m}$ . Ra values were calculated with a cut-off length of 2500/8000  $\mu\text{m}$ . The average surface roughness (Ra) measurements were performed according to the ISO 4287 and ISO 4288 standards. For *Build 2*, SEM micrographs were taken using an EVO MA25 ZEISS Scanning Electron Microscope (Zeiss, Jena, Germany) with a 50-150  $\times$ , and common defects were observed such as balling effect, pores and inconsistencies of the weld lines.

## 2.5 Nanoindentation and microstructure

A MTS Nanoindenter<sup>®</sup> XP equipped with TestWorks<sup>®</sup> software and Continuous Stiffness Measurement (CSM) technology were used in nanoindentation. Nanoindentation was performed on the PERP and PAR surfaces (Figure 3.7) with nine (9) measurements in three (3) different locations (1 mm, 5 mm, and 9 mm). Nanoindentation of *Build 2* samples, in a cross section of the rectangular prisms: 10  $\times$  10  $\times$  10 mm, was performed with a standard Berkovich tip with a radius of 50 nm and  $\varphi$  and  $\beta$  angles of 65.3° and 12.95°, respectively. Stainless steel 316L samples fabricated with L-PBF were previously cut by conventional Electrical Discharge Machining (EDM) in order to minimize the temperature and residual stress effects on the microstructures. Afterwards samples were cut and separated according to their orientation with respect to the building direction as parallel (PAR) and perpendicular (PERP) as shown in Figure 3.7. For this study, samples were put in Bakelite and polished with SiC grit paper from 240 to 1200, followed by polishing on micro polishing clothes with 5  $\mu\text{m}$  to 0.05  $\mu\text{m}$  alumina powders and 0.03  $\mu\text{m}$  colloidal silica for the final polishing step. The polished scratch-free samples were then carefully dried with acetone and air blow gun. The samples were collocated on the stage assembly of the MTS Nanoindenter<sup>®</sup> XP for the

nanoindentation testing. The parameters used for nanoindentation testing were a strain rate of  $5 \times 10^{-2} \text{ s}^{-1}$ , poisson's ratio of 0.3, and surface approach velocity of 10 nm/s. The instrument was calibrated before each of the batch tests using a standard fused silica specimen, in an array of  $3 \times 3$  indents with spacing of 100  $\mu\text{m}$  in 'x' and 'y' directions. The machine made an array of indents consecutively by minimizing the traveling distance of the indenter head. The indentation depth limit for each indent was 1500 nm to make it easier to find the indents on SEM imaging. Average hardness and modulus of elasticity were calculated based on all twenty-seven (27) indents of each sample. Statistical analysis was performed on the results to analyze if there was statistical difference between the results of hardness and modulus of elasticity (GPa).

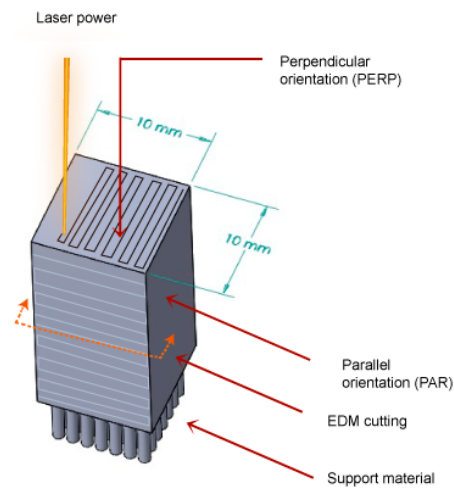


*Figure 3.7. AISI 316L part from which two samples were made by cutting it with EDM on perpendicular (PERP) and parallel (PAR) to build orientation.*

As far as the metal additive manufacturing process is concerned, a complex heat state is created during selective laser melting due to energy dissipation, heat transfer, melting, re-melting, solidification and re-solidification of powder particles, which provides a route to characteristic crystallographic microstructures of solidified melted powder particles [70]. In steels, chemical composition of all the alloying elements, existing phases and their microstructures determine the mechanical properties. Factors such as temperature gradient, variation in cooling rates, the lower conductivity of loose powder as well as process parameters all together contribute to different direction-dependent mechanical properties on the microstructural build up over the printed parts by L-PBF [71].

A FEI Nova NanoSEM 230 with EDAX Octane Elite EDS and Hikari Super EBSD detector with an operating voltage of 20 kV was used to obtain an EBSD map of the nanoindentation region. EBSD provides 2D maps of crystal orientation from cross-sections. The latest version (v8) OIM Analysis™ has reset the standard for EBSD data analysis capability with the addition of new functionality such as Neighbor Pattern Averaging and Reindexing (NPAR™) and other features which enables users to achieve new insight into microstructural characterization. The mirror

polished samples were tilted by  $70^\circ$  to increase the diffraction efficiency during the EBSD acquisition. TEAM™ EBSD analysis system was used for EBSD data acquisition, and TSL OIM Version 8 software was used for the data analysis. The scan area, the step size, and the average Confidence Index (CI) of EBSD acquisition were  $330\ \mu\text{m} \times 275\ \mu\text{m}$ ,  $1.00\ \mu\text{m}$ , and 0.90, respectively. The additively manufactured stainless steel 316L samples have a face-centered cubic (FCC) crystal structure or  $\gamma$ -phase. The selected  $\gamma$ -phase on the OIM software contained the information necessary to model the Electron Backscatter Pattern (EBSP) produced by the expected phase in the sample. The hardness and modulus of elasticity of each indent were identified from the nanoindentation data and thoroughly studied to find out any correlation between different crystallographic planes and mechanical properties.

### 3. Results and discussion

#### 3.1 Visual characterization and surface topography characterization and Roughness (Ra)

On *Build 1*, the weld lines were characterized on the PERP and PAR surfaces with non-contact 3D profilometry, and roughness was measured using the ISO 4287 and ISO 4288 standards. Through the experiment with different P, PD and ET, all the values were in a range of 0.32 to 9.33 J/mm of LED. From the micrographs taken with SteREO Discovery, visual criteria (Figure 3.3) were determined to verify the weldability of the material: by (i) continuous weld lines, by (ii) well-defined thickness, and by (iii) samples without defects (spatter particles, balling effects, voids). Examples of the criteria selection of improved parameters are shown in Figure 3.8. The Marangoni/Gibbs–Marangoni effect is a product of the surface tension gradient where the mass transfers along with an interface between two fluids. It has an essential role in how the material is welded, due to the temperature-driven in the process or the thermocapillary convection [72], and to produce continuous smooth tracks [73]. When the value of surface tension is negative, the cooler liquid pool tends to move the liquid metal away to the center where the material is hotter, and surface tension is lower. This flow is regulated by the Marangoni effect, where the flow on the surface is radically distorted always. Therefore when the liquid pool gets larger than the beam diameter, due to higher laser power [73,74] or a large PD, large surface thermal gradients are obtained, producing the weld lines shown in Figure 3.8 A-B. Thus, weld lines with lower LED (0.32-4.14 J/mm) produce more defects or discontinuities in the melt tacks, as it is shown in Figure 3.8 A) (2.14 J/mm) and Figure 3.8 B) (4.54 J/mm). Due to the low power values, all 75 W lines and samples with PD of  $37\ \mu\text{m}$  or  $56\ \mu\text{m}$  produced a wider melt pool; hence, distributions of thermal gradients resulted in unsatisfactory weldability according to the previously defined criteria, and this level of power was discarded for the upcoming experimentation in *Build 2*. When LED was found in its highest values, satisfactory weldability was found, as shown in Figure 3.8C) with LED of 5.18 J/mm.



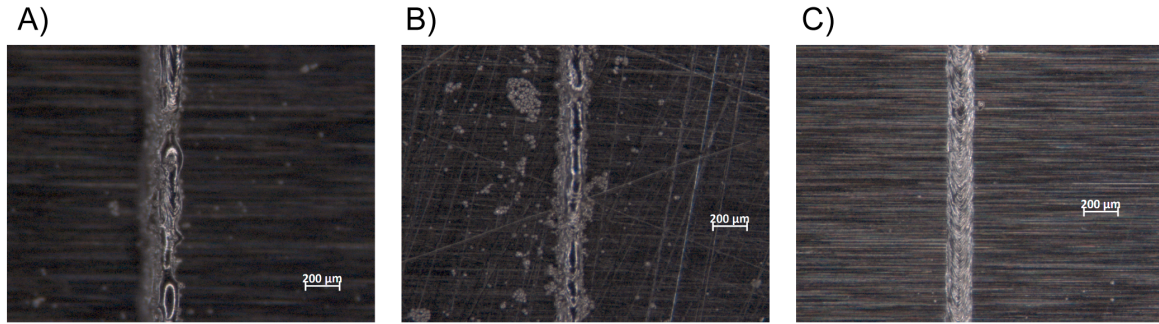


Figure 3.8. Visual selection of (A) Non continuous weld line P: 125W ET: 80  $\mu$ s PD: 56  $\mu$ m (B) Spatter particles surrounding the weld lines P: 175W ET: 80  $\mu$ s PD: 37  $\mu$ m (C) Uniform weld line P: 175W ET: 50  $\mu$ s PD: 18  $\mu$ m

From the visual characterization three values of LED were selected and parameters resulting in (A) LED: 6.66 J/mm (B) LED: 5.83 J/mm and (C) LED: 9.33 J/mm. These three top parameters were characterized by Focus Variation with an objective of 10x and a cut-off length of 8000  $\mu$ m (Figure 3.9). Resulted from the average in Ra of the triplicate of the weld lines of the top parameters fabricated with 7 layers, roughness (Ra) of (a) 12.672 $\mu$ m, (b) 15.163  $\mu$ m and (c) 12.145  $\mu$ m was found.

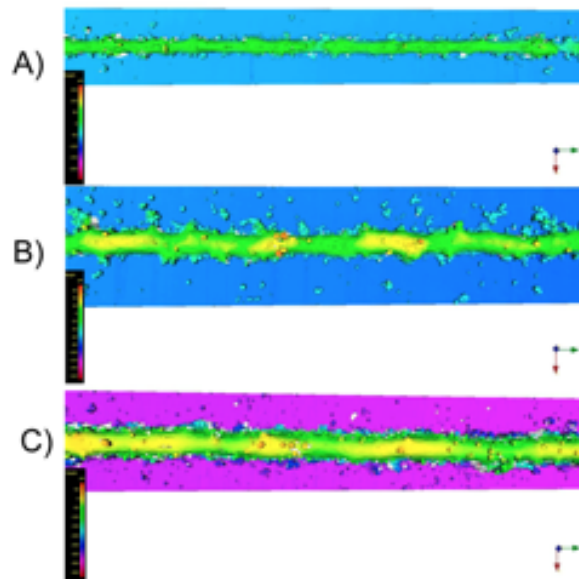


Figure 3.9. Top parameters in Build 1 (A) P: 175W ET: 50  $\mu$ s PD: 18  $\mu$ m (B) Spatter particles surrounding the weld lines, P: 125W ET: 80  $\mu$ s, PD: 18  $\mu$ m, and (C) Uniform weld line P: 175W ET: 80  $\mu$ s PD: 18  $\mu$ m.

The parameters with the best process response from *Build 1* were taken to the next level (*Build 2*), for performing three-dimensional fabrication of sample parts and using the additional parameters from Table 2 (LT and HD). From *Build 2*, geometric characteristics of the weld lines were also modified, and as a result, surface topography was different due to the thermal distribution of the previous layers and the weld lines attached to each other.

Surface roughness (Ra) was measured on the PAR and PERP surfaces of the samples with non-contact 3D profilometry by Focus Variation, without the use of additional post-processing operations. The average Ra from five areas of the PERP surface is shown in Figure 3.10. Results showed that with the highest value of LED (9.33 J/mm), the roughness was lower compared with the product of lower LED values. The lowest roughness Ra of 5.433  $\mu\text{m}$  was found at the highest value of LED and with a HD of 37  $\mu\text{m}$  (Sample 6). By using these parameter combinations in the volumetric energy density equation (VED), the lowest roughness was exhibited at the highest values of VED for the PERP surface.

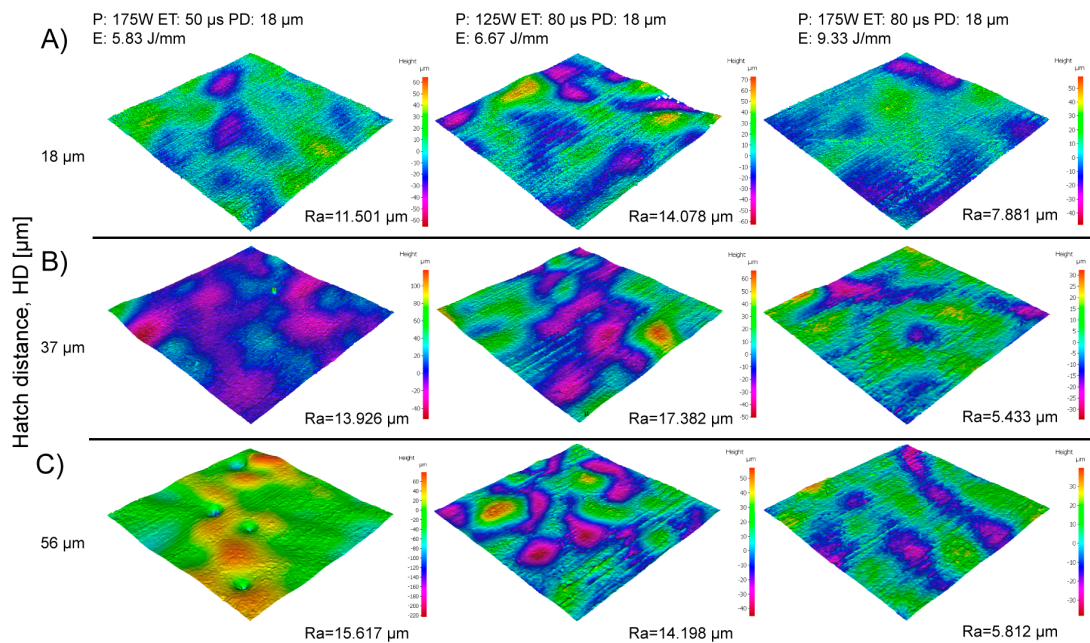


Figure 3.10. Roughness on the PERP orientation of the Build 2 parts (variation of hatch distance): **A)** HD: 18  $\mu\text{m}$ , **B)** HD: 37  $\mu\text{m}$ , and **C)** HD: 56  $\mu\text{m}$ .

Statistical difference was found in PERP oriented samples with a p-value < 0.05, using a one-way Anova test. In agreement with the work of previous authors, where they stated that with a 0° and 90° orientation angle, the roughness is higher on the 0° (PAR) samples due to the influence of the surrounding powder particles in the perimeters (borders) that are not completely melted [7]. A significant difference was found in the results of the PERP orientation samples where parameters influence the topography of the surface where a smooth surface, less defects (balling effects, holes, voids) were presented. On the other side, no significant difference was found on the samples with PAR surfaces. Values of Ra averaged in a range of 29.74 - 46.15  $\mu\text{m}$ , and a similar response of the means was found as shown in Figure 3.11. Processing parameters with higher VED produced higher values of Ra on the PAR oriented surfaces; in comparison, the same processing parameters on the PERP oriented surfaces result in lower Ra values due to the less amount of energy on the edges of the samples.

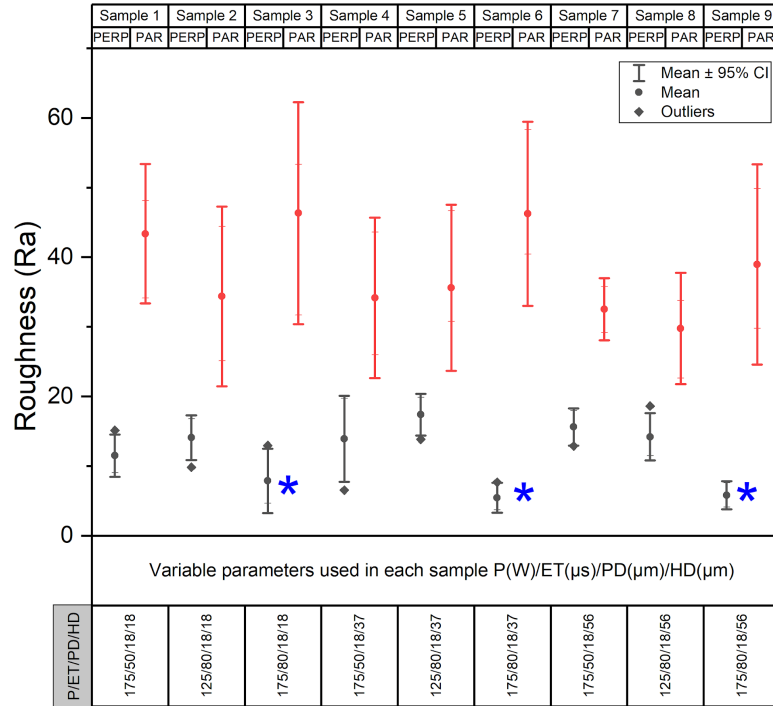


Figure 3.11 Roughness on the perpendicular and parallel orientation of the samples. (Lowest values of Roughness are marked with \* in blue).

### 3.2 Morphological characterization

Morphological characterization was performed on the PERP surfaces of different samples. From the previous analysis, two samples were selected to detect the most common defects in the criteria established in Figure 3.3, and showing smooth surfaces. Figure 3.12A (Sample 6) presented the lowest surface roughness obtained in this study, where the weld lines are continuous and uniform, and no defects were presented in the edges or particles attached to the surface. In contrast, Figure 3.12B-D (Sample 7) show evident defects such agglomeration of particles and voids, balling effects, and critically damaged surfaces due to the lower value of VED. These defects are more evident in the PERP surface and can result in lower density and porosity in the internal layers. Further studies on the density and porosity are needed to have more information about the internal structure of the samples.

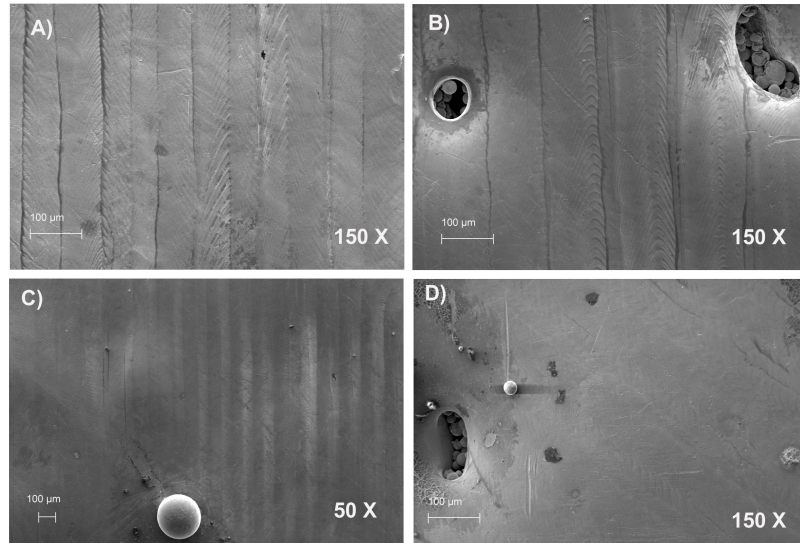


Figure 3.12 SEM Micrographs, (A) Well defined weld lines (150x), (B) Agglomeration of particles and voids (150x), (C) Balling effect and particles concentration (50x), and (D) Critical damaged surface (150x).

### 3.3 Nanoindentation and microstructure

#### 3.3.1 Nanoindentation

Nanoindentation results, hardness, and modulus of elasticity are shown in Figure 3.13. The average values of both modulus of elasticity and hardness values varied in all samples regardless of the orientation to the building direction. The average modulus values were found to be 192.61 GPa and 189.05 GPa for samples fabricated PERP and PAR to build direction respectively. Similarly, the average hardness values for samples fabricated PERP and PAR to build direction were found to be 4.01 GPa and 3.86 GPa respectively. The modulus and hardness results show a strong anisotropy [75] for most of the samples depending on the crystallographic orientation of each grain. The properties of additively manufactured stainless steel parts are known to be anisotropic because of the layer-by-layer melting and solidification of powder particles as well as inhomogeneity, which is related to location-dependent alterations due to extended dwell-times at relatively higher temperatures. This behavior is in agreement with the literature, in which the localized melting of powder particles could lead to inhomogeneous morphologies and, eventually, anisotropic behavior [36]. Post-heat treatment can overcome the inhomogeneity of aluminum-silicon alloys or steel [76,77]. Additionally, the variation of hardness values with the angle of build direction in L-PBF process was observed in previous studies [46,78–80] due to the presence of high residual stresses. These stresses are generated due to inhomogeneity of the melted powder particles layer and was previously discussed as voids and balling effect, which causes variation in layer thickness. During the fabrication of parts, deformation and loss of metallurgical contact with the substrate resulted in the accumulation of heat and redistribution of residual stresses.

In this study, samples 1 and 2 with the highest values of VED (810 and 925 J/mm<sup>3</sup>) presented the most porous surface with high percentage of impurities among all the samples; also exhibited the lowest average elastic modulus of 176.20 GPa and 143.79 GPa in both PAR and PERP orientations due to the high energy and slow laser scanning speed. Lowering the “energy per unit

length”, however, has a negative effect on the microstructure, since the energy input is insufficient, and the powder particles could not be completely melted.

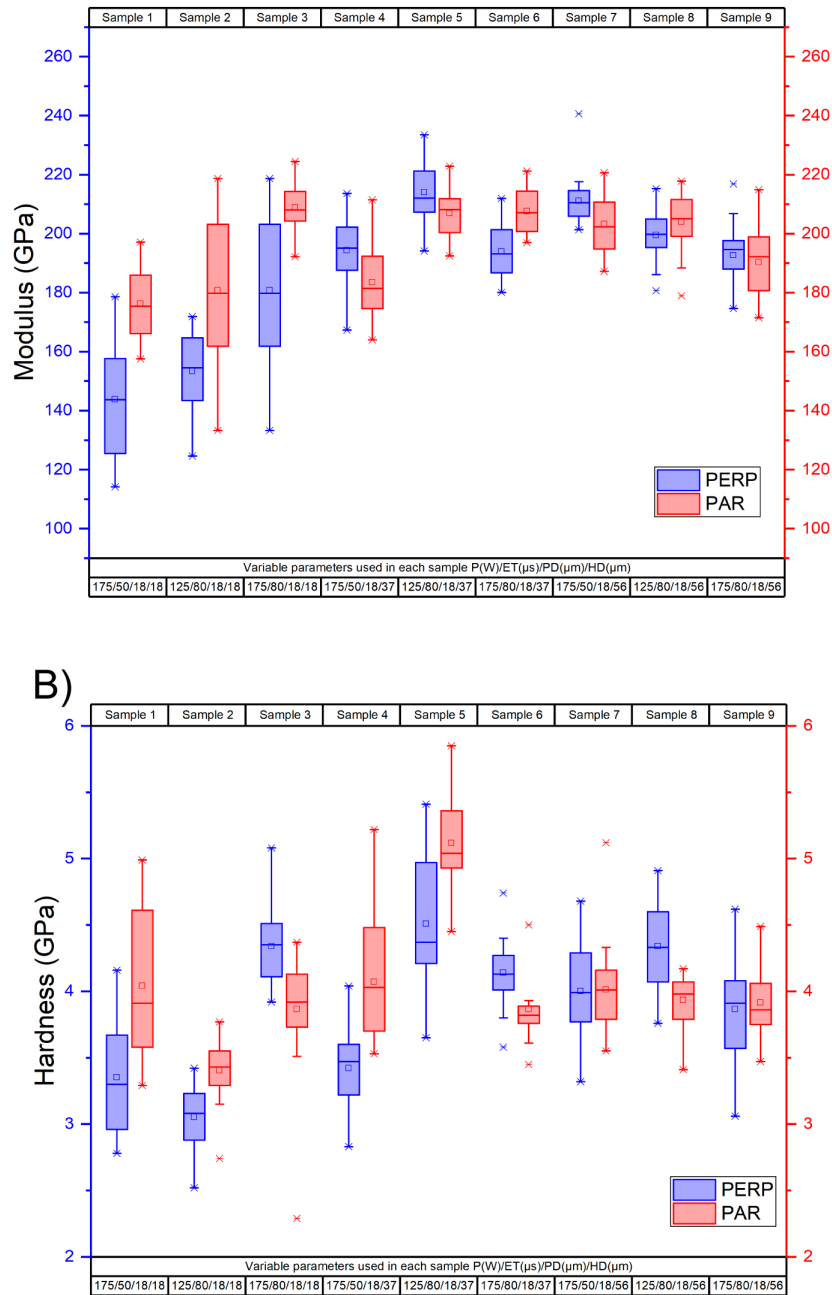


Figure 3.13 Nanoindentation measurements of samples. (A) Modulus of Elasticity (GPa) and (B) Hardness (GPa).

A one-way ANOVA with repeated measures was performed on the results of Modulus of Elasticity and Hardness, and a post-hoc Tukey test was done to compare the means of the samples. From this statistical analysis, a significant difference was presented in the samples with different parameters (P, ET, PD, HD) with a  $p < 0.05$  in both orientations (PAR and PERP). The means of the samples with HD of 56  $\mu\text{m}$  presented similar results where the average of Hardness was in a range of 3.91-4.01 GPa, and no statistical difference was found in the comparison of these samples (Samples 7-9). Samples with an HD of 18  $\mu\text{m}$  and 37  $\mu\text{m}$  presented a higher standard deviation

(0.22-0.55 GPa) compared to HD=56  $\mu\text{m}$  samples of where a standard deviation 0.18-0.31 GPa was found. However, the highest Hardness value was detected in samples of 37  $\mu\text{m}$ , where Sample 5 presented the best values in PAR and PERP orientations of 213.97 GPa (SD: 9.65 GPa) and 206.88 (SD: 7.88 GPa), respectively. On the other hand, the results of the Modulus of Elasticity presented a statistical difference with a  $p < 0.05$  in samples with different parameters. A similar tendency as with the Hardness was identified on samples with a HD of 56  $\mu\text{m}$  where results presented less standard deviation of 7.48-9.69 $\mu\text{m}$ , and samples of 37  $\mu\text{m}$  presented the highest value in the Modulus of Elasticity. The highest values of Hardness were also found in Sample 5 with VED (450.45 J/mm<sup>3</sup>) where PAR and PERP orientations showed values of 5.12 GPa (SD: 0.38 GPa) and 4.20 (SD: 0.24 GPa), respectively. As a result of this characterization stage, there is evidence of the influence of process parameters in surface mechanics, keeping the power at a lower level and the exposure time at the highest level for better nanoindentation response.

### 3.3.2 Electron Backscatter Diffraction

For the EBSD analysis, some works were taken for reference, in which researchers used EBSD maps for microstructural characteristics concerning the crystallographic orientation of L-PBF AISI 316L [67,70,81–91]. In the present study two different conditions were taken into consideration for the selection of samples for performing EBSD mapping: the best mechanical response and the best surface quality exhibited in the previous characterization with nanoindentation and focus variation respectively. Figure 3.14 shows the combination of EBSD Image Quality (IQ) greyscale maps and Inverse Pole Figure (IPF) maps, known as IQ + IPF maps, of additively manufactured AISI 316L samples number 5 (P: 125W ET: 80  $\mu\text{s}$  PD: 18  $\mu\text{m}$  and HD: 37  $\mu\text{m}$  (450.45 J/mm<sup>3</sup>)) and number 6 (P: 175W ET: 80  $\mu\text{s}$  PD: 18  $\mu\text{m}$  and HD: 37  $\mu\text{m}$  (630.63 J/mm<sup>3</sup>)). Figure 3.14 (A) and Figure 3.14 (B) show the IQ + IPF maps for PAR and PERP orientations in sample 5 respectively. Similarly, Figure 3.14 (C) and (D) show IQ + IPF maps of sample 6 in PAR and PERP orientations respectively. The colors on the maps are related to the orientation of crystal structures in the samples on the samples' surface normal direction.

From the visual inspection of IQ + IPF maps, elongated grains in PAR surfaces (Figure 3.14 (A) and (C)) were readily visible and scattered regular gains (coarse and fine) were observed in PERP surfaces (Figure 3.14 (B) and 14(D)) [70,88]. No elongated grains were visible in PERP surfaces, rather irregular but more overlapping grains were noticed due to the re-solidification of more weld pools on the same grains over and over again throughout the melting process. These elongated grains were wider and larger in size on the PAR surface due to directional solidification and thus related to the epitaxial growth and irregular scan strategy in the fabrication of the samples [89]. Additionally, newly nucleated grains of small columnar shapes in zigzag orientations were spotted around the intersections of the molten pool boundaries. In contrast, there were no dominant orientations of the grains found on the sample processed PERP to build direction.

The elastic modulus and hardness of each indent in the nanoindentation array of the two best samples were identified on the EBSD maps and shown in Figure Significant anisotropy

depending on the crystallographic orientation of each grain was observed based on mechanical properties such as modulus of elasticity and hardness by studying IQ + IPF maps with the array of nanoindenters [67,85–87]. Hardness and modulus of elasticity displayed variation on different grain orientations on sample 5, where the closely  $\langle 111 \rangle$  [67] and  $\langle 001 \rangle$  oriented grains exhibited the highest modulus of elasticity (~229.7 GPa) and hardness (~4.59 GPa) in PAR orientation as shown in Figure 3.14 (A). On the contrary, in PERP orientation, the highest modulus of elasticity (~228.8 GPa) and hardness (~4.11 GPa) found to be on  $\langle 101 \rangle$  oriented grains as shown in Figure 3.14 (B). Similar phenomenon was observed for sample 6; the closely  $\langle 111 \rangle$  oriented grains exhibited the highest modulus of elasticity (~212 GPa) and hardness (~4.5 GPa) in PAR orientation as evident in Figure 3.14, and in case of PERP orientation, the highest modulus of elasticity (~220.6 GPa) and hardness (~4.39 GPa) found to be on  $\langle 101 \rangle$  oriented grains as evident in Figure 3.14 (D). However,  $\langle 101 \rangle$  oriented grains in Figure 3.14 (A) found to have the lowest elastic modulus (~204.9 GPa) and hardness (~4.08 GPa). The average grain size (diameter) of sample 5 characterized PAR to build direction and PERP to build direction were 14.70  $\mu\text{m}$  and 11.36  $\mu\text{m}$  respectively, whereas, for sample no. 6 the average grain size (diameter) was 9.78  $\mu\text{m}$  in PAR and 18.50  $\mu\text{m}$  in PERP build directions [Table 6].

**Table 6.** Average grain size and misorientation angle for samples 5 and 6.

Sample #	Avg. grain size (diameter) ( $\mu\text{m}$ )	Avg. misorientation angle ( $^\circ$ )
5 (PERP)	14.7	5.23
5 (PAR)	11.36	5.29
6 (PERP)	9.78	4.92
6 (PAR)	18.5	4.97

The anisotropy and effect of grain orientation on the nanoindentation behavior of austenitic alloy Fe-15Cr-15Ni were thoroughly studied [67]. Their findings matched the results found in this study. The anisotropic behavior in modulus of elasticity was usually observed in uniaxial experiments on single crystals and is attributed to the anisotropy in elastic constants. The anisotropic behavior in hardness can be qualitatively correlated with the resolved shear stresses on slip/twinning systems estimated from Schmid’s law for uniaxial compression. The maximum Schmid factor for the  $\langle 111 \rangle$  compression is considerably lower than those for the  $\langle 001 \rangle$  and  $\langle 101 \rangle$  compressions; that difference could be the reason for the higher measured hardness near the  $\langle 111 \rangle$  pole in the stainless steel 316L samples [90,91]. This correlation proposes that during the loading stage of indentation, as stress increases followed by the expansion of the stress field in the material, the ease of continuous activation of slip/twinning systems acts as an essential role in determining the nanoindentation hardness.

Laser energy density and scanning strategy significantly affect the kind and texture degree of L-PBF fabricated 316L specimens. In the two selected samples, 5 and 6, the impact of the laser

power can be discussed where with a higher P, resulting in crystal growth aligned with build direction, higher texture degree, and higher aspect ratio (length/width) of the grains. As shown in Figure 3.14 (C), higher P= 175 W resulted in more aligned crystal growth in PAR orientation to build direction with a high aspect ratio compared to lower P= 125 W, as shown in Figure 3.14 (A). The orientation data collected with an EBSD system is spatially displayed in the Inverse Pole Figure (IPF). The IPF uses the color from the IPF color key, and the color assigned is based on the measured orientation. Typically low angle boundaries or subgrain boundaries are those with a misorientation less than 5 degrees [83]. High angle grain boundaries have a larger misorientation, generally more significant than 10 degrees. The low misorientation angles ( $5^\circ \pm 0.29$ ) observed for all the EBSD Image Quality (IQ) maps of Figure 3.14 might be due to higher dislocation spacing. This study was not aimed to discuss the dislocation model of grain boundaries. It was found that 78-88% of misorientation angles between adjacent cells were below 5%, where the misorientation angle distributions weighted by the section area. This result shows a similarity with previous studies [81,83]. In this study, misorientation angles were found to decrease for higher laser power of 175 W on both PAR ( $4.92^\circ$ ) and PERP ( $4.97^\circ$ ) orientations compared to lower laser power of 125 W in PAR ( $5.23^\circ$ ) and PERP ( $5.29^\circ$ ) orientations. EBSD map of sample 5 (best mechanical properties with P: 125W ET: 80  $\mu$ s PD: 18  $\mu$ m and HD: 37  $\mu$ m (VED: 450.45 J/mm<sup>3</sup>)) as shown in Figure 3.14 (B) clearly revealed apparent domination of <101> and lack of domination of <111>. EBSD maps additionally revealed the elongated grains in PAR orientation to build direction surfaces (Figure 3.14 (A) and (C)) and scattered regular gains but in different sizes (coarse and fine) and shapes in PERP orientations (Figure 3.14 (B) and (D)) [70,88].



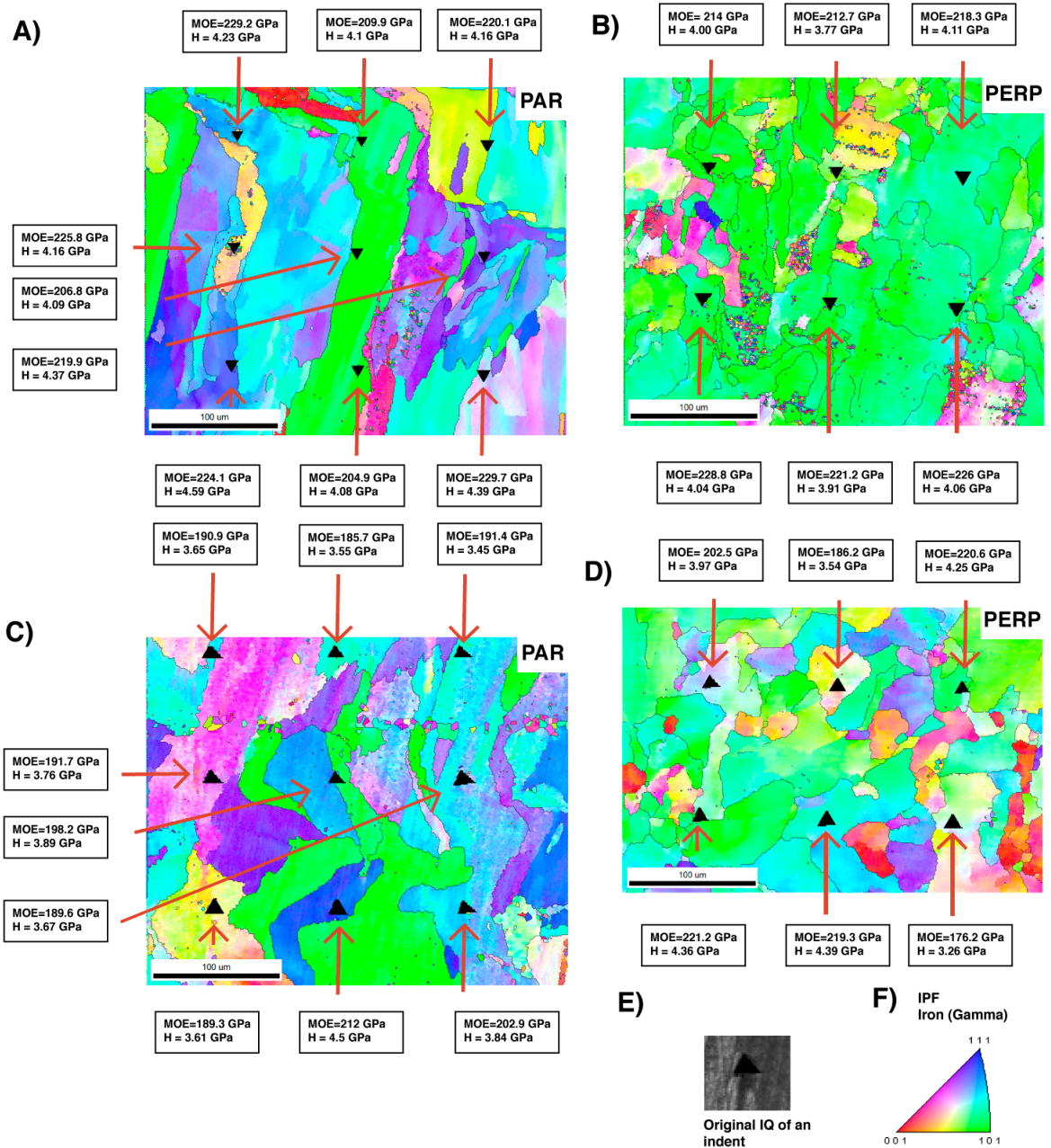


Figure 3.14. NanoSEM EBSD IQ+IPF maps with nanoindentations at 500X (A) PAR orientation and (B) PERP orientation of sample 5 (Parameters: HD: 37  $\mu\text{m}$  P: 125W ET: 80  $\mu\text{s}$  PD: 18  $\mu\text{m}$ ) (best mechanical properties) (C) PAR orientation (D) PERP orientation of sample 6 ( Parameters: HD: 37  $\mu\text{m}$  P: 175 W ET: 80  $\mu\text{s}$  PD: 18  $\mu\text{m}$ ) (best roughness) (E) Original IQ of an indent, and (F) IPF Iron (Gamma).

### 3.4 Microstructure analysis

L-PBF processed samples with different laser powers (125 and 175 watts) were mirror polished, and cellular dendritic structures were found under high magnification of the FE-SEM instrument. Detailed microstructure characteristics located in layer-layer melt pool boundary and track-track melt pool boundary are shown in Figure 3.15. Different regions of microstructural characteristics were found in the metallographic study, which confirmed some distinct morphologies, as observed in many recent studies of additive manufacturing of SS 316L [81–83,88,89,92–99]. Larger areas under FE-SEM are shown in Figure 3.15 (A) and (C) and Figure 3.15

(B) and 15(D) are magnified versions of selected regions selected from Figure 3.15(A) and (C). Cellular morphologies (region I) were found to appear in every sample. Variation in growth orientation of dendrites was observed. Some regions showed random and unexpected microstructural patterns marked as the region (III) in Figure 3.15 (B) and (D) for both lower and higher laser power, respectively. FE-SEM images exhibited finer cellular/dendritic structures for lower laser power (125 W) compared to higher laser power (175 W). This type of granulometry/microstructure was formed due to rapid solidification from high temperatures as well as repeated heating-cooling cycles of the melt pool regions of current and previously solidified layers underneath, which are very common microstructures found in laser processing techniques for similar stainless-steel grades. Planar interface growth was observed as the principal crystal growth pattern in the black dashed area (region II). The growth of new crystalline layers of cellular dendrite formed epitaxially at the solidified planar grains along the fusion line in the normal direction shown in Figure 3.15 (B) and 15(D), which is true according to theory. Although the angle between the growth orientation of dendrites and tangential of fusion may be affected not only by heat flux direction, but also by preferred growth orientation related to the crystal structure. Researchers studied and determined the reason for the variation of the planar grains in the melt pool [92]. They analyzed the connection between the preferred growth direction and preferred crystal orientation of the planar grains. In another study, it was predicted that Marangoni flow could change the heat flux direction which could cause convective heat transfer and flow of fluid within a melt pool and eventually could lead to altering growth orientation of those type of grains from the normal orientation and force to develop along the fusion line as shown in Figure 3.15(B) with black dash lines [93]. Primarily in SLM, grains choose to develop in the crystallographic orientation of the parent grains, and simultaneously, grains like to grow along the heat transfer direction, arising the competitive process among grains. Likewise, part of the previously solidified layer is subjected to the melting and cooling cycle during the printing process. In this way, the occurrence of remelting of the same solidified layers unquestionably refrains from nucleation for solidification. It allows the initial epitaxial growth at the partially remelted grains, which favors the growth of grains perpendicular to the curvature of the weld lines, as evident from Figure 3.15 (A) to (D).

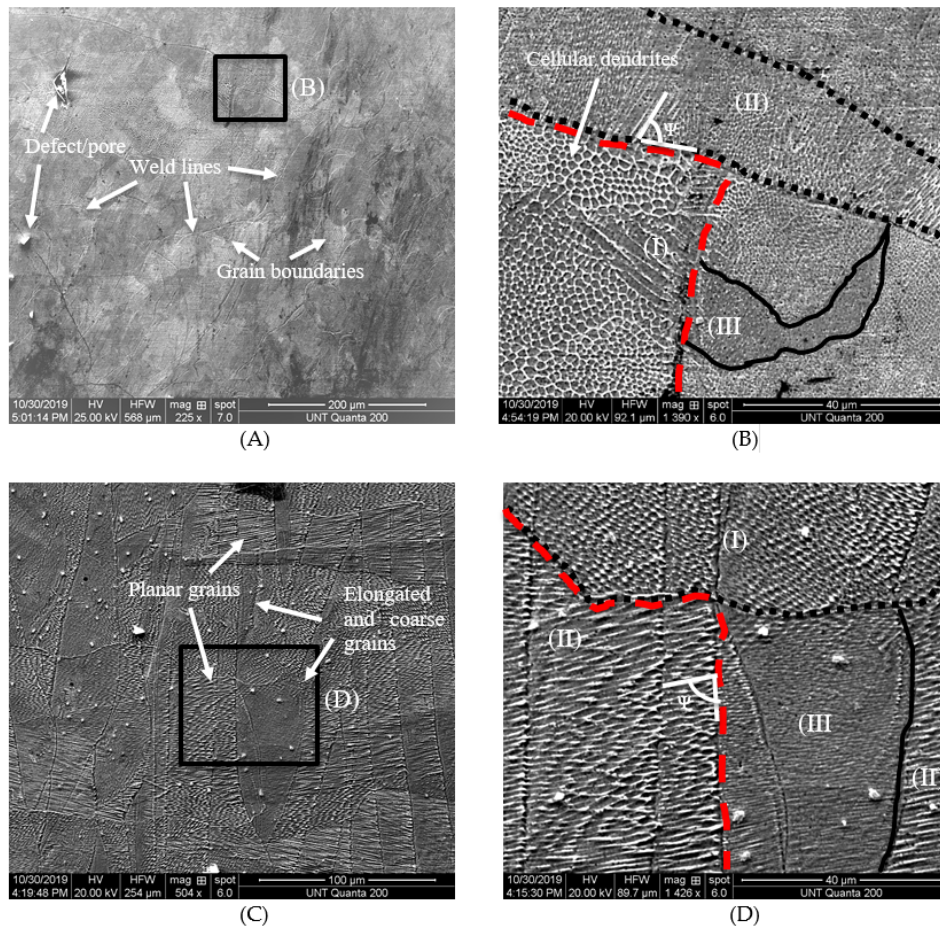


Figure 3.15. FIB/SEM images showing microstructures of two different laser powers, (A) and (B) Microstructural characteristics with layer-layer fusion pool boundary with laser power of 125 watts, (C) and (D) Microstructural characteristics of higher laser power of 175 watts.

Microstructural characteristics were studied using an optical microscope. These characteristics are shown in Figure 3.16A to F with details. Mirror polished samples were dried following standard procedure, where defects and pores were visible even with naked eyes and etched with Marble's (4g CuSO<sub>4</sub> and 20 ml HCl added to 20 ml distilled water) reagent. Few noticeable features were the presence of elongated and coarse grains as well as clearly visible cellular dendrites and planar grains on the samples printed perpendicular to the build directions as shown in Figure 3.16 (A), 16(C), and 16(E). These coarse elongated grains correspond to higher laser power (175 W) compared to lower laser power (125 W) due to solidification from higher temperatures. This phenomenon is clearly shown and marked with arrows as are visible in Figure 3.16 (C) and 16(D). PAR oriented to build direction samples revealed a mixture of coarse and fine grain microstructure as shown in Figure 3.16 (B), 16(D), and 16(E), but there was no presence of elongated grains.

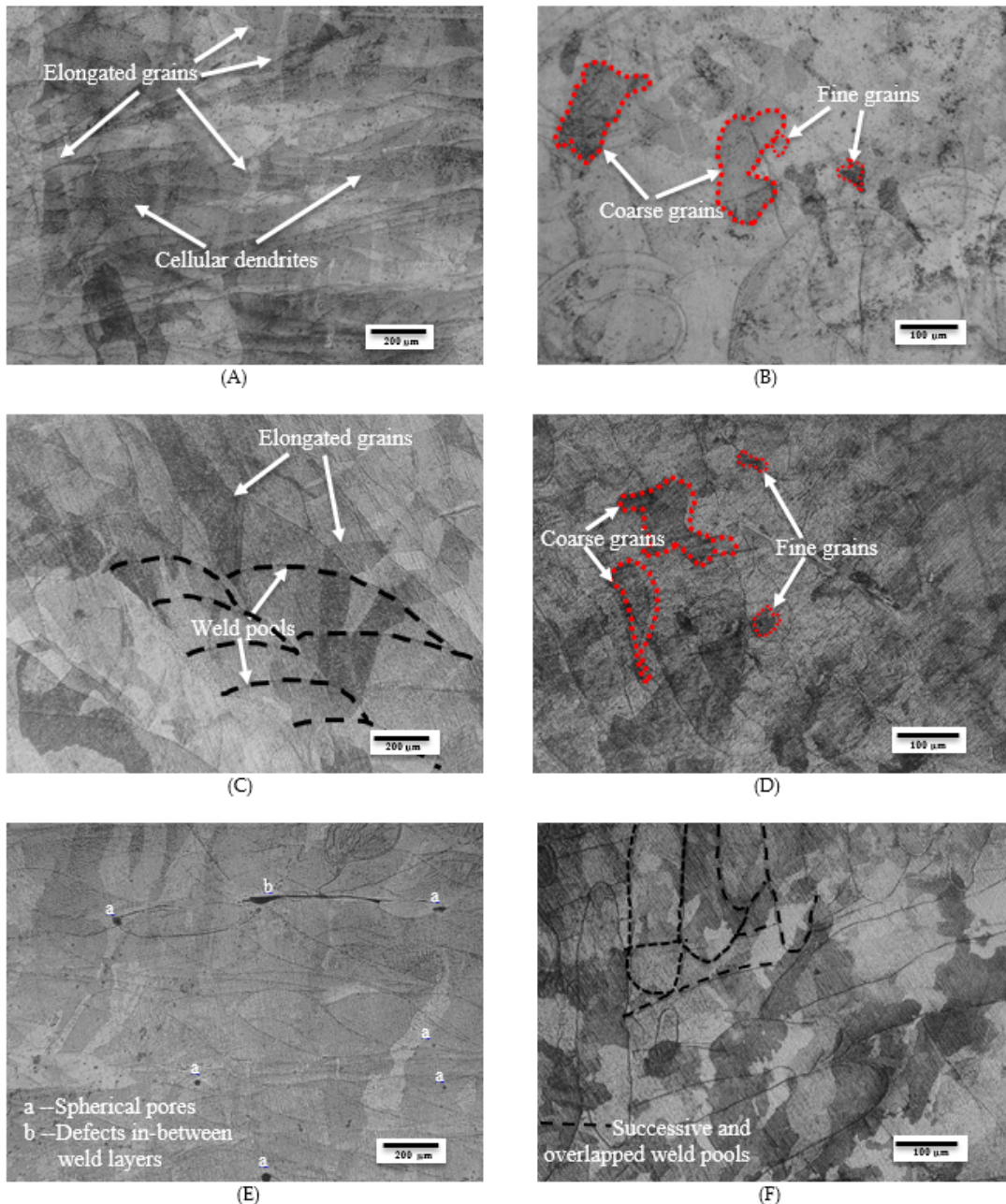


Figure 3.16 Microstructures of various laser power with various hatch distances on both parallel and perpendicular to build direction are shown (HD: 37  $\mu\text{m}$  P: 125W ET: 80  $\mu\text{s}$  PD: 18  $\mu\text{m}$ ) (A) and (B) show the microstructural characteristics in PERP and PAR respectively. (C) and (D) show the microstructural characteristics in PERP and PAR (HD: 37  $\mu\text{m}$  P: 175W ET: 80  $\mu\text{s}$  PD: 18  $\mu\text{m}$ ), and lastly for (E) and (F) show microstructural characteristics in PAR and PER of (HD: 56  $\mu\text{m}$  P: 175W ET: 80  $\mu\text{s}$  PD: 18  $\mu\text{m}$ ).

As shown in Figure 3.16 (C), 16(D), and 16(F), the overlapping nature of the melt pool is a confirmation of the successful fusion of powder particles and strong bonding within successive layers [93]. The planar grains crossed and grew further beyond the weld line. The growth of planar grain did not stop at fusion lines. Semicircular shaped weld lines were observed for all the samples perpendicular to building direction as in Figure 3.16 (A), 16(C), and 16(D) even in very low magnification.

Most of the pores exhibited a spherical shape and formed due to entrapment of gas bubbles during solidification from high temperatures in the L-PBF process [94]. The spherical gas bubbles

were found to be randomly distributed within individual melt pools, and elongated larger defects were preferentially seemed to form between melt pools corresponding to two successive layers, as shown in Figure 3.16 (E). These elongated defects have appeared more on samples built perpendicularly to build direction than samples built parallel to build direction. Unmelted SS316L powders particles might be the reason associated with these defects. In detail, instability of the melt pool due to thermocapillary phenomena [81], or the lack of proper wetting of the melt pool on the material that had been previously solidified [98] was responsible for the formation of these larger defects. Hence, sufficient remelting of the previous layers is mandatory to produce a clean surface upon solidification. The absence of such sufficient remelting, as well as unmelted powder particles, contributed to a large number of elongated defects on the samples perpendicularly built to build direction.

## 4. Conclusions

The methodology of two levels presented in this work leads to the selection of appropriate SLM process parameters, useful for the improvement of surface quality and mechanical properties, microstructure characterization.

- The microstructural analysis of the samples allowed establishing a set of optimized L-PBF process parameters. This qualitative analysis threw that the best weldability was obtained at high values of LED by the combination of the PD = 18  $\mu\text{m}$ , ET = 80  $\mu\text{s}$  and P = 175 W resulting in 9.33J/mm of LED. The laser power showed a high impact on the consolidation of the samples. Elongated grains were even coarser in samples that correspond to the highest Power, P = 175 W, than compared to the lower Power, P = 125 W due to solidification from higher temperatures. A clear effect is seen in the overlapping of the melt pool, which is an indicator of successful fusion of powder particles and strong bonding within successive layers.
  - Another indicator of the parameter's optimization is observed in the surface quality found in the PERP surfaces. PERP surfaces with LED of 9.33 J/mm with different HD overlapping produced the lowest values of Ra. The best Roughness (Ra) value was 5.433  $\mu\text{m}$  (PERP oriented surface), and the sample was fabricated with the following parameters P=175W, ET=80  $\mu\text{s}$ , PD=18  $\mu\text{m}$ , HD= 37 $\mu\text{m}$ .
  - Nanoindentation results were related with the crystallographic orientations of the grains. The highest values of Hardness and Modulus of Elasticity were 229.7 GPa and 4.59 GPa respectively for the sample with P=125W, ET=80  $\mu\text{s}$ , PD=18  $\mu\text{m}$ , HD = 37  $\mu\text{m}$  with the closely oriented grains in <111> and <101> with an average grain size of 11.36  $\mu\text{m}$  for PAR orientation.
  - Based on the EBSD results, it can be determined that the best mechanical properties are found in normal loads applied to the manufacturing directions (PAR surface), therefore, if it is sought to apply this to an application, it is necessary that the part be oriented in favor of that crystallographic region.

From the previous methodology a range of parameters with good mechanical properties and roughness can be obtained. Further studies should be made on the interaction between layers and how the microstructure changes through the part and compared with density and porosity.

## Abbreviations

<i>AM</i>	<i>Additive manufacturing</i>
<i>CAD</i>	<i>computer-aided design</i>
<i>CI</i>	<i>Confidence Index</i>
<i>CW</i>	<i>continuous pulse</i>
<i>EDM</i>	<i>Electrical Discharge Machining</i>
<i>EBM</i>	<i>Electron Beam Melting</i>
<i>EBP</i>	<i>Electron Backscatter Pattern</i>
<i>EBSD</i>	<i>Electron Backscatter Diffraction</i>
<i>FCC</i>	<i>face-centered cubic</i>
<i>FV</i>	<i>Focus Variation</i>
<i>LED</i>	<i>linear energy density</i>
<i>L-PBF</i>	<i>laser powder bed fusion</i>
<i>PAR</i>	<i>orientation parallel to the build direction</i>
<i>PERP</i>	<i>orientation perpendicular to the build direction</i>
<i>ppm</i>	<i>parts per million</i>
<i>PWM</i>	<i>pulse width modulated</i>
<i>SLM</i>	<i>Selective Laser Melting</i>
<i>STL</i>	<i>Standard Tessellation Language</i>
<i>VED</i>	<i>volumetric energy density</i>

## Nomenclature

<i>ET</i>	<i>Exposure Time</i>
<i>HD</i>	<i>Hatch Distance</i>
<i>L</i>	<i>number of layers</i>
<i>LT</i>	<i>Layer thickness</i>
<i>P</i>	<i>laser power</i>
<i>PD</i>	<i>Point Distance</i>
<i>vs</i>	<i>laser scanning speed</i>

## References

- [1] T. Wohlers, I. Campbell, O. Diegel, Others, Wohlers Report 2018, Fort Collins: Wohlers Associates. (2018).
- [2] Document search by keywords: selective laser melting, Wwww.scopus.com. (n.d.). <https://www.scopus.com/> (accessed December 9, 2019).
- [3] K.G. Prashanth, S. Scudino, H.J. Klauss, K.B. Surreddi, L. Löber, Z. Wang, A.K. Chaubey, U. Kühn, J. Eckert, Microstructure and mechanical properties of Al–12Si produced by selective laser melting: Effect of heat treatment, *Materials Science and Engineering: A*. 590 (2014) 153–160. <https://doi.org/10.1016/j.msea.2013.10.023>.
- [4] T. Kurzynowski, E. Chlebus, B. Kuźnicka, J. Reiner, Parameters in selective laser melting for processing metallic powders, in: *High Power Laser Materials Processing: Lasers, Beam Delivery, Diagnostics, and Applications*, International Society for Optics and Photonics, 2012: p. 823914.
- [5] J. Kim, S. Ji, Y.-S. Yun, J.-S. Yeo, A Review: Melt Pool Analysis for Selective Laser Melting with Continuous Wave and Pulse Width Modulated Lasers, *Appl. Sci. Converg. Technol.* 27 (2018) 113–119.
- [6] J.H. Robinson, I.R.T. Ashton, E. Jones, P. Fox, C. Sutcliffe, The effect of hatch angle rotation on parts manufactured using selective laser melting, *Rapid Prototyping Journal*. 25 (2019) 289–298.

- [7] E. Segura-Cardenas, E.G. Ramirez-Cedillo, J.A. Sandoval-Robles, L. Ruiz-Huerta, A. Caballero-Ruiz, H.R. Siller, Permeability Study of Austenitic Stainless Steel Surfaces Produced by Selective Laser Melting, *Metals* . 7 (2017) 521.
- [8] H. Ali, H. Ghadbeigi, K. Mumtaz, Effect of scanning strategies on residual stress and mechanical properties of Selective Laser Melted Ti6Al4V, *Materials Science and Engineering: A*. 712 (2018) 175–187.
- [9] D. Koutny, D. Palousek, L. Pantelejev, C. Hoeller, R. Pichler, L. Tesicky, J. Kaiser, Influence of Scanning Strategies on Processing of Aluminum Alloy EN AW 2618 Using Selective Laser Melting, *Materials* . 11 (2018). <https://doi.org/10.3390/ma11020298>.
- [10] A.G. Demir, B. Previtali, Additive manufacturing of cardiovascular CoCr stents by selective laser melting, *Mater. Des.* 119 (2017) 338–350.
- [11] Z.Y. Liu, C. Li, X.Y. Fang, Y.B. Guo, Energy Consumption in Additive Manufacturing of Metal Parts, *Procedia Manufacturing*. 26 (2018) 834–845.
- [12] G.M. Grigorenko, V.A. Kostin, Criteria for evaluating the weldability of steels, *Weld. Int.* 27 (2013) 815–820.
- [13] D. Gu, Y.-C. Hagedorn, W. Meiners, G. Meng, R.J.S. Batista, K. Wissenbach, R. Poprawe, Densification behavior, microstructure evolution, and wear performance of selective laser melting processed commercially pure titanium, *Acta Mater.* 60 (2012) 3849–3860.
- [14] M.-H. Hong, B.K. Min, T.-Y. Kwon, The Influence of Process Parameters on the Surface Roughness of a 3D-Printed Co–Cr Dental Alloy Produced via Selective Laser Melting, *NATO Adv. Sci. Inst. Ser. E Appl. Sci.* 6 (2016) 401.
- [15] P. Wei, Z. Wei, Z. Chen, J. Du, Y. He, J. Li, Y. Zhou, The AlSi10Mg samples produced by selective laser melting: single track, densification, microstructure and mechanical behavior, *Appl. Surf. Sci.* 408 (2017) 38–50.
- [16] Q. Jia, D. Gu, Selective laser melting additive manufacturing of Inconel 718 superalloy parts: Densification, microstructure and properties, *J. Alloys Compd.* 585 (2014) 713–721.
- [17] L.C. Zhang, D. Klemm, J. Eckert, Y.L. Hao, T.B. Sercombe, Manufacture by selective laser melting and mechanical behavior of a biomedical Ti–24Nb–4Zr–8Sn alloy, *Scr. Mater.* 65 (2011/6) 21–24.
- [18] M. Sadowski, L. Ladani, W. Brindley, J. Romano, Optimizing quality of additively manufactured Inconel 718 using powder bed laser melting process, *Additive Manufacturing*. 11 (2016) 60–70.
- [19] K. Mumtaz, N. Hopkinson, Top surface and side roughness of Inconel 625 parts processed using selective laser melting, *Rapid Prototyping Journal*. 15 (2009) 96–103.
- [20] K.G. Prashanth, S. Scudino, T. Maity, J. Das, J. Eckert, Is the energy density a reliable parameter for materials synthesis by selective laser melting?, *Materials Research Letters*. 5 (2017) 386–390.
- [21] I. Koutiri, E. Pessard, P. Peyre, O. Amlou, T. De Terris, Influence of SLM process parameters on the surface finish, porosity rate and fatigue behavior of as-built Inconel 625 parts, *J. Mater. Process. Technol.* 255 (2018) 536–546.
- [22] U.S. Bertoli, A.J. Wolfer, M.J. Matthews, J.-P.R. Delplanque, J.M. Schoenung, On the limitations of Volumetric Energy Density as a design parameter for Selective Laser Melting | Elsevier Enhanced Reader, (n.d.). <https://doi.org/10.1016/j.matdes.2016.10.037>.
- [23] T. Peng, C. Chen, Influence of energy density on energy demand and porosity of 316L stainless steel fabricated by selective laser melting, *International Journal of Precision Engineering and Manufacturing-Green Technology*. 5 (2018) 55–62.
- [24] J.A. Cherry, H.M. Davies, S. Mehmood, N.P. Lavery, S.G.R. Brown, J. Sienz, Investigation into the effect of process parameters on microstructural and physical properties of 316L stainless steel parts by selective laser melting, *Int. J. Adv. Manuf. Technol.* 76 (2015) 869–879.
- [25] A. Ilie, H. Ali, K. Mumtaz, In-Built Customised Mechanical Failure of 316L Components Fabricated Using Selective Laser Melting, *Technologies*. 5 (2017) 9.
- [26] H. Meier, C. Haberland, Experimental studies on selective laser melting of metallic parts, *Mat.-Wiss. U. Werkstofftech.* 39 (2008) 665–670.

- [27] E. Ramirez-Cedillo, J.A. Sandoval-Robles, L. Ruiz-Huerta, A. Caballero-Ruiz, C.A. Rodriguez, H.R. Siller, Process planning guidelines in selective laser melting for the manufacturing of stainless steel parts, *Procedia Manufacturing*. 26 (2018) 973–982.
- [28] L. Junfeng, W. Zhengying, Process Optimization and Microstructure Characterization of Ti6Al4V Manufactured by Selective Laser Melting, in: *IOP Conference Series: Materials Science and Engineering*, IOP Publishing, 2017: p. 012026.
- [29] D.K. Do, P. Li, The effect of laser energy input on the microstructure, physical and mechanical properties of Ti-6Al-4V alloys by selective laser melting, *Virtual Phys. Prototyp.* 11 (2016) 41–47.
- [30] J. Han, J. Yang, H. Yu, J. Yin, M. Gao, Z. Wang, X. Zeng, Microstructure and mechanical property of selective laser melted Ti6Al4V dependence on laser energy density, *Rapid Prototyping Journal*. 23 (2017) 217–226.
- [31] G. Kasperovich, J. Haubrich, J. Gussone, G. Requena, Correlation between porosity and processing parameters in TiAl6V4 produced by selective laser melting, *Mater. Des.* 105 (2016) 160–170.
- [32] T. Mishurova, S. Cabeza, K. Artzt, J. Haubrich, M. Klaus, C. Genzel, G. Requena, G. Bruno, An Assessment of Subsurface Residual Stress Analysis in SLM Ti-6Al-4V, *Materials* . 10 (2017). <https://doi.org/10.3390/ma10040348>.
- [33] B. Vandenbroucke, J. Kruth, Selective laser melting of biocompatible metals for rapid manufacturing of medical parts, *Rapid Prototyping Journal*. 13 (2007) 196–203.
- [34] E. Liverani, A. Fortunato, A. Leardini, C. Belvedere, S. Siegler, L. Ceschini, A. Ascari, Fabrication of Co–Cr–Mo endoprosthetic ankle devices by means of Selective Laser Melting (SLM), *Mater. Des.* 106 (2016) 60–68.
- [35] N. Read, W. Wang, K. Essa, M.M. Attallah, Selective laser melting of AlSi10Mg alloy: Process optimisation and mechanical properties development, *Mater. Des.* 65 (2015) 417–424.
- [36] S. Yusuf, Y. Chen, R. Boardman, S. Yang, N. Gao, Investigation on Porosity and Microhardness of 316L Stainless Steel Fabricated by Selective Laser Melting, *Metals* . 7 (2017) 64.
- [37] C. Casavola, S.L. Campanelli, C. Pappalettere, Preliminary investigation on distribution of residual stress generated by the selective laser melting process, *J. Strain Anal. Eng. Des.* 44 (2009) 93–104.
- [38] K. Abd-Elghany, D.L. Bourell, Property evaluation of 304L stainless steel fabricated by selective laser melting, *Rapid Prototyping Journal*. 18 (2012) 420–428.
- [39] K. Guan, Z. Wang, M. Gao, X. Li, X. Zeng, Effects of processing parameters on tensile properties of selective laser melted 304 stainless steel, *Mater. Des.* 50 (2013) 581–586.
- [40] R. Stamp, P. Fox, W. O'Neill, E. Jones, C. Sutcliffe, The development of a scanning strategy for the manufacture of porous biomaterials by selective laser melting, *J. Mater. Sci. Mater. Med.* 20 (2009) 1839–1848.
- [41] D. Wang, W. Dou, Y. Yang, Research on Selective Laser Melting of Ti6Al4V: Surface Morphologies, Optimized Processing Zone, and Ductility Improvement Mechanism, *Metals* . 8 (2018) 471.
- [42] W. Shi, Y. Liu, X. Shi, Y. Hou, P. Wang, G. Song, Beam Diameter Dependence of Performance in Thick-Layer and High-Power Selective Laser Melting of Ti-6Al-4V, *Materials* . 11 (2018). <https://doi.org/10.3390/ma11071237>.
- [43] A.M. Khorasani, I. Gibson, U.S. Awan, A. Ghaderi, The Effect of SLM Process Parameters on Density, Hardness, Tensile Strength and Surface Quality of Ti-6Al-4V, *Additive Manufacturing*. 25 (2018) 176–186.
- [44] B. Song, S. Dong, B. Zhang, H. Liao, C. Coddet, Effects of processing parameters on microstructure and mechanical property of selective laser melted Ti6Al4V, *Mater. Des.* 35 (2012/3) 120–125.
- [45] B. Van Hooreweder, D. Moens, R. Boonen, J.-P. Kruth, P. Sas, Analysis of Fracture Toughness and Crack Propagation of Ti6Al4V Produced by Selective Laser Melting, *Adv. Eng. Mater.* 14 (2012) 92–97.
- [46] E. Chlebus, B. Kuźnicka, T. Kurzynowski, B. Dybała, Microstructure and mechanical behaviour of Ti–6Al–7Nb alloy produced by selective laser melting, *Mater. Charact.* 62 (2011/5) 488–495.
- [47] K. Monroy, J. Delgado, L. Sereno, J. Ciurana, N.J. Hendrichs, Geometrical feature analysis of Co-Cr-Mo single tracks after selective laser melting processing, *Rapid Prototyping Journal*. (2015).



<https://doi.org/10.1108/RPJ-11-2013-0122>.

- [48] X. Zhou, D. Wang, X. Liu, D. Zhang, S. Qu, J. Ma, G. London, Z. Shen, W. Liu, 3D-imaging of selective laser melting defects in a Co–Cr–Mo alloy by synchrotron radiation micro-CT, *Acta Mater.* 98 (2015) 1–16.
- [49] A.G. Demir, L. Monguzzi, B. Previtali, Selective laser melting of pure Zn with high density for biodegradable implant manufacturing, *Additive Manufacturing.* 15 (2017/5) 20–28.
- [50] L. Thijs, K. Kempen, J.-P. Kruth, J. Van Humbeeck, Fine-structured aluminium products with controllable texture by selective laser melting of pre-alloyed AlSi10Mg powder, *Acta Mater.* 61 (2013) 1809–1819.
- [51] C. Weingarten, D. Buchbinder, N. Pirch, W. Meiners, K. Wissenbach, R. Poprawe, Formation and reduction of hydrogen porosity during selective laser melting of AlSi10Mg, *J. Mater. Process. Technol.* 221 (2015) 112–120.
- [52] L.P. Lam, D.Q. Zhang, Z.H. Liu, C.K. Chua, Phase analysis and microstructure characterisation of AlSi10Mg parts produced by Selective Laser Melting, *Virtual Phys. Prototyp.* 10 (2015) 207–215.
- [53] N.T. Aboulkhair, N.M. Everitt, I. Ashcroft, C. Tuck, Reducing porosity in AlSi10Mg parts processed by selective laser melting, *Additive Manufacturing.* 1-4 (2014) 77–86.
- [54] E. Brandl, U. Heckenberger, V. Holzinger, D. Buchbinder, Additive manufactured AlSi10Mg samples using Selective Laser Melting (SLM): Microstructure, high cycle fatigue, and fracture behavior, *Mater. Des.* 34 (2012) 159–169.
- [55] I. Rosenthal, M. Nahmany, A. Stern, N. Frage, Structure and Mechanical Properties of AlSi10Mg Fabricated by Selective Laser Melting Additive Manufacturing (SLM-AM), 1111 (2015) 62–66.
- [56] A.B. Anwar, Q.-C. Pham, Selective laser melting of AlSi10Mg: Effects of scan direction, part placement and inert gas flow velocity on tensile strength, *J. Mater. Process. Technol.* 240 (2017) 388–396.
- [57] Y. Lu, S. Wu, Y. Gan, T. Huang, C. Yang, L. Junjie, J. Lin, Study on the microstructure, mechanical property and residual stress of SLM Inconel-718 alloy manufactured by differing island scanning strategy, *Opt. Laser Technol.* 75 (2015) 197–206.
- [58] Z. Baicheng, L. Xiaohua, B. Jiaming, G. Junfeng, W. Pan, S. Chen-nan, N. Muiling, Q. Guojun, W. Jun, Study of selective laser melting (SLM) Inconel 718 part surface improvement by electrochemical polishing, *Mater. Des.* 116 (2017) 531–537.
- [59] M. Xia, D. Gu, G. Yu, D. Dai, H. Chen, Q. Shi, Influence of hatch spacing on heat and mass transfer, thermodynamics and laser processability during additive manufacturing of Inconel 718 alloy, *Int. J. Mach. Tools Manuf.* 109 (2016) 147–157.
- [60] S. Li, Q. Wei, Y. Shi, Z. Zhu, D. Zhang, Microstructure Characteristics of Inconel 625 Superalloy Manufactured by Selective Laser Melting, *J. Mater. Sci. Technol.* 31 (2015) 946–952.
- [61] R. Danzl, F. Helml, S. Scherer, Focus variation--a new technology for high resolution optical 3D surface metrology, in: *The 10th International Conference of the Slovenian Society for Non-Destructive Testing*, Citeseer, 2009: pp. 484–491.
- [62] T. Özel, A. Altay, B. Kaftanoğlu, R. Leach, N. Senin, A. Donmez, Focus Variation Measurement and Prediction of Surface Texture Parameters Using Machine Learning in Laser Powder Bed Fusion, *J. Manuf. Sci. Eng.* 142 (2020). <https://doi.org/10.1115/1.4045415>.
- [63] A. Triantaphyllou, C.L. Giusca, G.D. Macaulay, F. Roerig, M. Hoebel, R.K. Leach, B. Tomita, K.A. Milne, Surface texture measurement for additive manufacturing, *Surf. Topogr.: Metrol. Prop.* 3 (2015) 024002.
- [64] E. Renner, Y. Gaillard, F. Richard, F. Amiot, P. Delobelle, Sensitivity of the residual topography to single crystal plasticity parameters in Berkovich nanoindentation on FCC nickel, *Int. J. Plast.* 77 (2016) 118–140.
- [65] Y. Liu, S. Varghese, J. Ma, M. Yoshino, H. Lu, R. Komanduri, Orientation effects in nanoindentation of single crystal copper, *Int. J. Plast.* 24 (2008) 1990–2015.
- [66] Y.Z. Xia, H. Bei, Y.F. Gao, D. Catoor, E.P. George, Synthesis, characterization, and nanoindentation response of single crystal Fe–Cr–Ni alloys with FCC and BCC structures, *Materials Science and Engineering: A.* 611 (2014) 177–187.

- [67] T. Chen, L. Tan, Z. Lu, H. Xu, The effect of grain orientation on nanoindentation behavior of model austenitic alloy Fe-20Cr-25Ni, (n.d.).
- [68] A.B. Spierings, N. Herres, G. Levy, Influence of the particle size distribution on surface quality and mechanical properties in additive manufactured stainless steel parts, (n.d.). [https://www.icvr.ethz.ch/ConfiguratorJM/publications/Influence\\_\\_132039575561997/Spierings\\_2011\\_\\_\\_Influence\\_of\\_the\\_particle\\_size\\_distribution\\_on\\_surface\\_quality\\_and\\_mechanical\\_properties\\_in\\_A.pdf](https://www.icvr.ethz.ch/ConfiguratorJM/publications/Influence__132039575561997/Spierings_2011___Influence_of_the_particle_size_distribution_on_surface_quality_and_mechanical_properties_in_A.pdf).
- [69] L. Tanchev, *Virtual and Rapid Manufacturing: Advanced Research in Virtual and Rapid Prototyping*, CRC Press, 2007.
- [70] C. Mutke, K. Geenen, A. Röttger, W. Theisen, Interaction between laser radiation and metallic powder of 316L austenitic steel during selective laser melting, *Mater. Charact.* 145 (2018) 337–346.
- [71] Crystal structure analysis of M2 high speed steel parts produced by selective laser melting, (n.d.). <https://doi.org/10.1016/j.matchar.2013.07.010>.
- [72] B. Xiao, Y. Zhang, Numerical Simulation of Direct Metal Laser Sintering of Single-Component Powder on Top of Sintered Layers, *J. Manuf. Sci. Eng.* 130 (2008). <https://doi.org/10.1115/1.2951948>.
- [73] K. Antony, N. Arivazhagan, STUDIES ON ENERGY PENETRATION AND MARANGONI EFFECT DURING LASER MELTING PROCESS, (2016). <https://www.semanticscholar.org/paper/fb584353fa9fcf85fb2bb16699eab921d0d10d6b> (accessed December 7, 2019).
- [74] T.-N. Le, Y.-L. Lo, Effects of sulfur concentration and Marangoni convection on melt-pool formation in transition mode of selective laser melting process, *Mater. Des.* 179 (2019) 107866.
- [75] L. Hitzler, J. Hirsch, B. Heine, M. Merkel, W. Hall, A. Öchsner, On the Anisotropic Mechanical Properties of Selective Laser-Melted Stainless Steel, *Materials* . 10 (2017). <https://doi.org/10.3390/ma10101136>.
- [76] L. Hitzler, C. Janousch, J. Schanz, M. Merkel, B. Heine, F. Mack, W. Hall, A. Öchsner, Direction and location dependency of selective laser melted AlSi10Mg specimens, *J. Mater. Process. Technol.* 243 (2017) 48–61.
- [77] R. Rashid, S.H. Masood, D. Ruan, S. Palanisamy, R.A. Rahman Rashid, M. Brandt, Effect of scan strategy on density and metallurgical properties of 17-4PH parts printed by Selective Laser Melting (SLM), *J. Mater. Process. Technol.* 249 (2017) 502–511.
- [78] M S I, W.S.W. Harun, N.Z. Khalil, F. Ahmad, M.H. Ismail, S. Sharif, Effect of heat treatment on mechanical properties and microstructure of selective laser melting 316L stainless steel, *IOP Conf. Ser.: Mater. Sci. Eng.* 257 (2017) 012021.
- [79] B. Vrancken, V. Cain, R. Knutsen, J. Van Humbeeck, Residual stress via the contour method in compact tension specimens produced via selective laser melting, *Scr. Mater.* 87 (2014) 29–32.
- [80] P. Rangaswamy, M.L. Griffith, M.B. Prime, T.M. Holden, R.B. Rogge, J.M. Edwards, R.J. Sebring, Residual stresses in LENS® components using neutron diffraction and contour method, *Materials Science and Engineering: A.* 399 (2005) 72–83.
- [81] I. Yadroitsev, P. Krakhmalev, I. Yadroitsava, S. Johansson, I. Smurov, Energy input effect on morphology and microstructure of selective laser melting single track from metallic powder, *J. Mater. Process. Technol.* 213 (2013) 606–613.
- [82] A. Röttger, K. Geenen, M. Windmann, F. Binner, W. Theisen, Comparison of microstructure and mechanical properties of 316L austenitic steel processed by selective laser melting with hot-isostatic pressed and cast material, *Materials Science and Engineering: A.* 678 (2016) 365–376.
- [83] T. Kurzynowski, K. Gruber, W. Stopyra, B. Kuźnicka, E. Chlebus, Correlation between process parameters, microstructure and properties of 316 L stainless steel processed by selective laser melting, *Materials Science and Engineering: A.* 718 (2018) 64–73.
- [84] C.A. Bronkhorst, J.R. Mayeur, V. Livescu, R. Pokharel, D.W. Brown, G.T. Gray, Structural representation of additively manufactured 316L austenitic stainless steel, *Int. J. Plast.* 118 (2019) 70–86.
- [85] J. Suryawanshi, K.G. Prashanth, U. Ramamurty, Mechanical behavior of selective laser melted 316L stainless steel, *Materials Science and Engineering: A.* 696 (2017) 113–121.

- [86] C. Tromas, J.C. Stinville, C. Templier, P. Villechaise, Hardness and elastic modulus gradients in plasma-nitrided 316L polycrystalline stainless steel investigated by nanoindentation tomography, *Acta Mater.* 60 (2012) 1965–1973.
- [87] J.M. Jeon, J.M. Park, J.-H. Yu, J.G. Kim, Y. Seong, S.H. Park, H.S. Kim, Effects of microstructure and internal defects on mechanical anisotropy and asymmetry of selective laser-melted 316L austenitic stainless steel, *Materials Science and Engineering: A*. 763 (2019) 138152.
- [88] R. Casati, J. Lemke, M. Vedani, Microstructure and Fracture Behavior of 316L Austenitic Stainless Steel Produced by Selective Laser Melting, *J. Mater. Sci. Technol.* 32 (2016) 738–744.
- [89] Y. Yang, Y. Zhu, M.M. Khonsari, H. Yang, Wear anisotropy of selective laser melted 316L stainless steel, *Wear*. 428-429 (2019) 376–386.
- [90] H. Ljungcrantz, M. Odén, L. Hultman, J.E. Greene, J. -E Sundgren, Nanoindentation studies of single-crystal (001)-, (011)-, and (111)-oriented TiN layers on MgO, *J. Appl. Phys.* 80 (1996) 6725–6733.
- [91] C.A. Brookes, J.B. O'Neill, B.A.W. Redfern, D. Tabor, Anisotropy in the hardness of single crystals, *Proc. R. Soc. Lond. A Math. Phys. Sci.* 322 (1971) 73–88.
- [92] D. Wang, C. Song, Y. Yang, Y. Bai, Investigation of crystal growth mechanism during selective laser melting and mechanical property characterization of 316L stainless steel parts, *Mater. Des.* 100 (2016) 291–299.
- [93] W.M. Tucho, V.H. Lysne, H. Austbø, A. Sjolyst-Kverneland, V. Hansen, Investigation of effects of process parameters on microstructure and hardness of SLM manufactured SS316L, *J. Alloys Compd.* 740 (2018) 910–925.
- [94] A. Mertens 1a, S. Reginster 1b, Q. Contrepois 1c, T. Dormal 2d, O. Lemaire 3e, J. Lecomte-Beckers 1f, Microstructures and Mechanical Properties of Stainless Steel AISI 316L Processed by Selective Laser Melting, (n.d.). <https://doi.org/10.4028/www.scientific.net/MSF.783-786.898>.
- [95] Y. Zhong, L. Liu, S. Wikman, D. Cui, Z. Shen, Intragranular cellular segregation network structure strengthening 316L stainless steel prepared by selective laser melting, *J. Nucl. Mater.* 470 (2016) 170–178.
- [96] E. Yasa, J.-P. Kruth, Microstructural investigation of Selective Laser Melting 316L stainless steel parts exposed to laser re-melting, *Procedia Engineering*. 19 (n.d.) 389–395.
- [97] E. Liverani, S. Toschi, L. Ceschini, A. Fortunato, Effect of selective laser melting (SLM) process parameters on microstructure and mechanical properties of 316L austenitic stainless steel, *J. Mater. Process. Technol.* 249 (2017) 255–263.
- [98] J. -P. Kruth, G. Levy, F. Klocke, T.H.C. Childs, Consolidation phenomena in laser and powder-bed based layered manufacturing, (n.d.). <https://doi.org/10.1016/j.cirp.2007.10.004>.
- [99] J.P. Kruth, L. Froyen, J. Van Vaerenbergh, P. Mercelis, M. Rombouts, B. Lauwers, Selective laser melting of iron-based powder, *J. Mater. Process. Technol.* 149 (2004) 616–622.

# Chapter 3 Overall Conclusions

As a product of this work, an integral approach of the LPBF technology, commercially named as SLM has been presented where the following results contribute to the literature and the industry to have a better standardization and documentation of all internal y external variables of this manufacturing process.

- UPLCI has been implemented on the SLM manufacturing process by using the calculation of the energy consumed through the process, and the mass and the inert gas losses. The energy was divided for its analysis in active, idle, and basic energies, and later analyzed in the different stages of the process.

- A Process guideline for the improvement of surface integrity and mechanical properties for SLM with different characterization methods contributes to the analysis of the different responses of the process by changing various parameters. An optimized range of parameters was developed for the following materials SS316L, SS174PH, TI6ALV4.

A few medical applications were validated and improved with the previous results where process Chains for the Fabrication of three customized implants were proposed. All the cases of study in this work were presented to treat osteosarcoma cancer: Cranial, Tibia, Mandible and Humerus, and medical devices were also optimized by using lattice structures, topology optimization, and weight reduction.

# Appendix A

Process planning guidelines in selective laser melting for the manufacturing of stainless steel parts  
June 2018  
Conference: North American Manufacturing Research Conference 46At: College Station, TX  
Project: Additive Manufacturing in Metals  
Lab: Leopoldo Ruiz-Huerta's Lab



46th SME North American Manufacturing Research Conference, NAMRC 46, Texas, USA

## Process planning guidelines in selective laser melting for the manufacturing of stainless steel parts

Erick Ramirez-Cedillo<sup>1,4</sup>, Jesús A. Sandoval-Robles<sup>1,4</sup>, Leopoldo Ruiz-Huerta<sup>2,4</sup>, Alberto Caballero-Ruiz<sup>2,4</sup>, Ciro A. Rodriguez<sup>1,4</sup>, and Hector R. Siller<sup>3,4\*</sup>

<sup>1</sup>Tecnológico de Monterrey, Av. Eugenio Garza Sada #2501 Sur, Monterrey, N.L. 64849, Mexico

<sup>2</sup>Centro de Ciencias Aplicadas y Desarrollo Tecnológico (CCADET)  
Universidad Nacional Autónoma de México (UNAM)

Circuito Exterior S/N, Ciudad Universitaria AP 70-186, C.P. 04510, Ciudad de México, México

<sup>3</sup>Department of Engineering Technology, University of North Texas, Denton Tx., 76207, United States of America  
<sup>4</sup>Laboratorio Nacional de Manufactura Aditiva, Digitalización 3D y Tomografía Computarizada (MADiT), México

\* Corresponding author. Tel.: +1.940.565.2362

E-mail address: [Hector.Siller@unt.edu](mailto:Hector.Siller@unt.edu)

---

### Abstract

Selective laser melting (SLM) is now, one of the most widespread Additive Manufacturing processes, due to presence in the market and known capabilities for the fabrication of mechanical components, with acceptable levels in geometrical accuracy, surface quality and mechanical properties. However, the metalworking industry is still skeptical for its full adoption in realistic production schemes, because of the lack of non-scholarly knowledge for calibrating process parameters among other technical barriers. In this work, several process planning guidelines are presented as a result of a SLM process calibration for a selected material (stainless steel 316L), with the intention of contributing in process parameters selection in net shape manufacturing. In order to conceive a proper set of guidelines for selective laser melting set up, several parameters were taken into account such as point distance, hatch distance, exposure time among others, with the aim of obtaining appropriate surface quality and good mechanical tensile behavior. Parts were obtained with good surface quality, presenting stable and well-defined weld lines and low presence of partially sintered particles adhered to the surface. After the application of the methodology, top and lateral surface roughness were improved, reaching values of Ra 5.81 and 9.61  $\mu\text{m}$  respectively. In addition, good mechanical properties were obtained, of up to 500 MPa of ultimate tensile strength and 400 MPa of yield stress, comparable to the properties of sintered stainless steels alloys studied in previous works.

© 2018 The Authors. Published by Elsevier B.V.

Peer-review under responsibility of the scientific committee of the 46th SME North American Manufacturing Research Conference.

*Keywords:* selective laser melting, process planning, powder bed laser melting, surface quality, roughness

---

## Nomenclature

AM	Additive Manufacturing
B	Border
BC	Beam Compensation
BD	Border Distance
DS	Downskin
E	Energy Density
ET	Exposure Time
FC	Fill Contour
FCD	Fill Contour Distance
FCO	Fill Contour Offset
HD	Hatch Distance
HO	Hatch Offset
L	Layers
LT	Layer Thickness
PD	Point Distance
Q	Specific Energy
M	Meander
NE	Number of Exposures
SLM	Selective Laser Melting
STL	STL file format
US	Upskin

## 1. Introduction

Powder bed fusion technologies such selective laser melting (SLM), are nowadays used in a variety of applications for the manufacturing of metallic components, to tailor particular needs in biomedical devices and other applications requiring high degrees of customization [1,2]. Manufacturing processes of these components have to be highly controlled, especially at the post-processing steps, in order to achieve the suitable surface conditions for such applications. Depending on the component and its application, the desired surface roughness may differ. For example, surgical instruments, hip, ankle and shoulder joints require a smooth surface; while for prosthetic components that require osseointegration like pins, implants, and screws, surfaces must have customized properties [3]. Regarding the Additive Manufacturing technologies, several process parameters can be modified to improve the roughness of the final part, achieving acceptable values to minimize the post-processing.

The research work to date is extensive and covers several aspects like process parameters calibration and optimization, laser scanning strategies, materials

characterization, mechanical properties testing, powder modification, among others. However, the industrial users of this technology are still skeptical about the general performance of additively manufactured components.

Many researchers have presented studies of the correlation between parameters with microstructure or mechanical properties [4], aspects like the effects of the alloy during the process [5], and the use of re-melting layers [6]. For example, Sun et al. obtained a parameters optimization using the Taguchi method and regression analysis. They found that most significant factors for the process could be classified in this order: powder thickness > scanning strategy > linear energy density > hatching distance [7]. Hong et al. made its analysis of the impact of processing parameters on surface roughness, using a single line test. They analyzed hatch distance (*HD*), point distance (*PD*), and exposure time (*ET*), and found that by reducing the laser power and increasing scan rate, balling effect was avoided [8]. K. Abd-Elghany and D.L. Bourell studied the impact of the scanning speed and the layer thickness on the surface roughness. They used cubic samples, and found porosity and under melted areas in large layer thicknesses [9]. Liverani et al. worked with different laser power, scan speed, hatching and tilt angles, and found optimized parameters by iterations, and by further mechanical testing and microstructure characterization [10].

Zhang et al. studied the mechanical properties of SLM of stainless steel. They found that with a combination of *HD* of 80  $\mu\text{m}$ , a laser speed of 0.3 m/s and a specific energy of  $6.67 \times 10^4 \text{ J/m}^2$ , the mechanical behavior of stainless steel exhibited a good tensile strength of between 501.1 and 547.6 MPa [11]. Other researchers found that with a layer thickness of 50  $\mu\text{m}$ , a laser power of 100 W, and a laser speed of 0.3 m/s, 625 MPa of ultimate tensile strength and 525–547 of yield strength can be obtained [12].

According to the literature reviewed, the most important effects related with product integrity and surface quality are the following:

- Balling effect and agglomeration of particles on the top surface.
- Voids or distortion of the weld lines, due to the excess of temperature in a specific area.
- Porosity related with under melting or high values of *HD*.

This work aims to present a set of guidelines for the process planning of selective laser melting, and to provide quality assessment, which could be used for

the evaluation of the full adoption of this technology for rapid fabrication of personalized stainless steel devices.

## 2. Methodology

### 2.1. Experimental set-up

For this experimental trial, we used powder bed laser fusion, specifically Selective Laser Melting. The system (Renishaw AM400, UK) allows the manufacture of metal parts within a volume of  $250 \times 250 \times 300$  mm. The radiation source was a laser Yb-fiber with a maximum power  $P=400$  W, a wavelength of  $\lambda=1075$  nm and a spot size calibrated at  $d=75$   $\mu\text{m}$ . The powder used was austenitic stainless steel (designation SS 316L-0410, Renishaw-United Kingdom) with the following composition: Fe (Bal), Cr (16-18%), Ni (10-14%), Mo (2-3%), Mn (<2%), Si N (<0.1%), O (<0.1%), P (0.045%), C (0.03%), S (0.03%). The average particle size was  $45 \pm 15$   $\mu\text{m}$  and the working layer thickness ( $LT$ ) was 50  $\mu\text{m}$ .

The procedure of parameters selection is graphically represented in Fig 1. This diagram is divided into three groups of activities: (1) design of experiments, (2) samples fabrication, (3) characterization and selection of parameters. Each stage will be explained across the following subsections.

At *Activity 1*, the design of experiments was structured to get lower surface roughness values for diminishing post-processing operations. In this regard, 170W of laser power was fixed as a setting point, according to the optimal parameters of other researchers, who found the laser power in a range of 150 - 175W, to avoid porosity and to exhibit higher mechanical properties [10,13,14].

### 2.2 Samples design

Samples were designed using SolidWorks (SolidWorks, Dassault Systems SolidWorks Corporation, USA). In the first group of test pieces, named *Build 1*, squared parts of  $15 \times 15$  mm and 75  $\mu\text{m}$  of thickness were used, in an array of  $6 \times 6$  with a separation of  $15 \text{ mm} \times 15 \text{ mm}$ . For *Builds 2* to *Build 4*, bullet shaped cylinders were fabricated, for allowing easy removal from the build plate. The bullets designs have diameter of 15 mm and different heights: 22 mm for *Build 2* (array:  $6 \times 5$ ) and *Build 3* (array:  $1 \times 4$ ), and 13 mm for *Build 4* (array:  $9 \times 6$ ).

### 2.3 Experimental design

The parameters combinations were settled taking into account the boundaries imposed by the powder size and the range of possible values in the melting process.

At *Activity 2*, the set of geometries explained before was fabricated by varying process parameters, and edited in QuantAM 3.4.0. software (Renishaw-United Kingdom). The fabrication of samples was grouped by using the four *Build* geometries and by relating them with a particular process-planning feature: (1) weld lines, (2) bulk hatching, (3) side superficial characteristics, and (4) volume areas with some angle. After the melting process, the samples were removed from the building plate and were brought to a cleaning process. All samples were washed in ultrasonic bath for 10 minutes in distilled water, 10 minutes in acetone and dried.

During the *Activity 3*, two characterization types were needed for establishing the most appropriate set of parameters: morphological characterization and surface topography measurement.

### 2.4 Morphological characterization

During morphological characterization, the samples were visually inspected in order to discard samples that did not accomplish the appropriate weld lines or bulk construction. Qualitative analysis was performed using a SteREO Discovery V8 microscope equipped with a CCD camera AxioCam (Carl Zeiss Micro imaging GmbH, Jena, Germany), using LM Image Manager (Leica Microsystems), and AxioVision 4.5 software (Carl Zeiss). Additionally, the morphology was analyzed by using an EVO MA25 ZEISS Scanning Electron Microscope (Zeiss, Jena, Germany) with an accelerating voltage of 20 kV and high vacuum.

### 2.5 Surface topography measurement

The surface roughness ( $R_a$ ) was measured in three areas of *Builds 1* to *4*. The average surface roughness ( $R_a$ ) measurements were performed using the ISO 4287 standard with a non-contact 3D profilometer ( Alicona Infinite Focus microscope, IFM G4), with 20x of magnification, vertical resolution of 50  $\mu\text{m}$ , lateral resolution of 3.5  $\mu\text{m}$  and cut-off length of 2500  $\mu\text{m}$ .



## 2.6 Procedure details

a) On *Build 1* (weld lines and squared parts), continuous and uniform weld lines are the criteria for parameters selection. For this experiment, two parameters were modified in the fabrication of simple geometries. The selected parameters were the ones that influenced the creation of a weld line: *PD* and *ET*. The *PD* is the distance between each pulse of the laser that sinters the material (Fig. 1-A), and was varied in a range from 20 to 120  $\mu\text{m}$ . The *ET* represents how long the pulse is maintained in a point, and the range was varied from 20 to 120  $\mu\text{s}$  (Fig. 1-B). Both parameters were varied in steps of 20, and Thirty-six samples were fabricated. With these two parameters, the specific energy dissipated in the powder layer can be calculated as follows:

$$Q = \frac{P \cdot ET}{PD \cdot LT} \quad \text{Eq. (1)}$$

where the Specific energy ( $Q$ ) is given in  $\text{J}/\text{m}^2$ ;  
 $P$  is the power used in  $W$ ;  
 $ET$  is the exposure time and is given in seconds;  
 and  $PD$  and  $LT$  are given in meters.

For the characterization of weld lines, a qualitative analysis was performed to the samples by visual inspection. Parameters were selected according to the following criteria: (i) continuous weld lines, (ii) well-defined corners, and (iii) samples without accumulation of particles by the excess of temperature or lower powder sintering. The top 5 parameters were used for the next *Build*.

b) However, in agreement with the literature, with high values of  $HD$ , porosity may appear and may affect part integrity [16] (Fig. 1-D). Accordingly,  $HD$  values were varied in a range between 0.60 to 0.16 mm, in intervals of 0.2 mm in *Build 2*. With this parameter, energy density ( $E$ ) applied to the sintered volume can be calculated by the following equation:

$$E = \frac{Q}{HD} \quad \text{Eq. (2)}$$

where the Energy density ( $E$ ) is given in  $\frac{\text{GJ}}{\text{m}^3}$ .

The selection of the bulk hatching was made by a qualitative analysis using the following criteria: (i) over melted bulk, (ii) under melted bulk, and (iii) particles not melted over the top surface.

c) *Build 3* was fabricated to have an improvement of the lateral surface roughness by using a number of

borders ( $B$ ) and fill contours ( $FC$ ). Borders are weld lines on the outside of the bulk hatching. The beam compensation ( $BC$ ) was established at 0.0225 mm, which is distance between the digital file boundary (STL file) and  $B$ . Border distance ( $BD$ ), the separation between the hatching lines and the  $B$ , was defined at 0.06 mm. The fill contour distance ( $FCD$ ) is the distance between  $FC$ s, and it was set at 0.06 mm. Fill contour offset ( $FCO$ ) is the distance between the first  $B$  and the last  $FC$ , and it was set at 0.06 mm. On the other hand,  $FC$ s were programmed to be inside the hatching volume and at the half of the distance between the  $FC$  and the outside  $B$  (Fig 1-E).

Surface roughness ( $R_a$ ) was measured on the lateral surfaces of the samples. The parameters of bulk hatching, with different quantities of  $B$  and  $FC$  were selected by the lower  $R_a$ .

d) For the last set of experiments *Build 4*, two different scanning strategies were used: meander ( $M$ ) and stripes ( $S$ ) (Figure 1-G). In addition, two QuantAm proprietary configurations, upskin ( $US$ ) and downskin ( $DS$ ) were added to the fabrication parameters, and several power values were used for a re-melting mode ( $P=130, 150, \text{ and } 170W$ ), to reduce the marks produced by the overlapping of the scan paths and weld lines. The upskin and downskin parameters were set in a range of 0-2 exposures ( $NE$ ) and 1-3 layers ( $L$ ) of re-melting. These are layers without power dosing, and consequently the layer could be re-melted, improving the final roughness in these surfaces. The hatch offset ( $HO$ ) was defined as 0.03 mm (Fig 1-F). Roughness ( $R_a$ ) was measured on the top and lateral surface of the samples. Top parameters were selected as the ones that improve part quality.

## 2.7 Tensile test

For the analysis of mechanical strength of the specimens fabricated, five samples were taken with a width range of 6.81-6.82 mm and a thickness range of 6.31-6.34 mm. Samples were then vertically mounted between the mechanical grippers of a universal testing machine (AGS-X 100kN, Shimadzu Co., Kyoto, Japan). According to the standard for metal tensile test ASTM-E8, the test speed was set at 2.7 mm/min for all of the tested specimens.

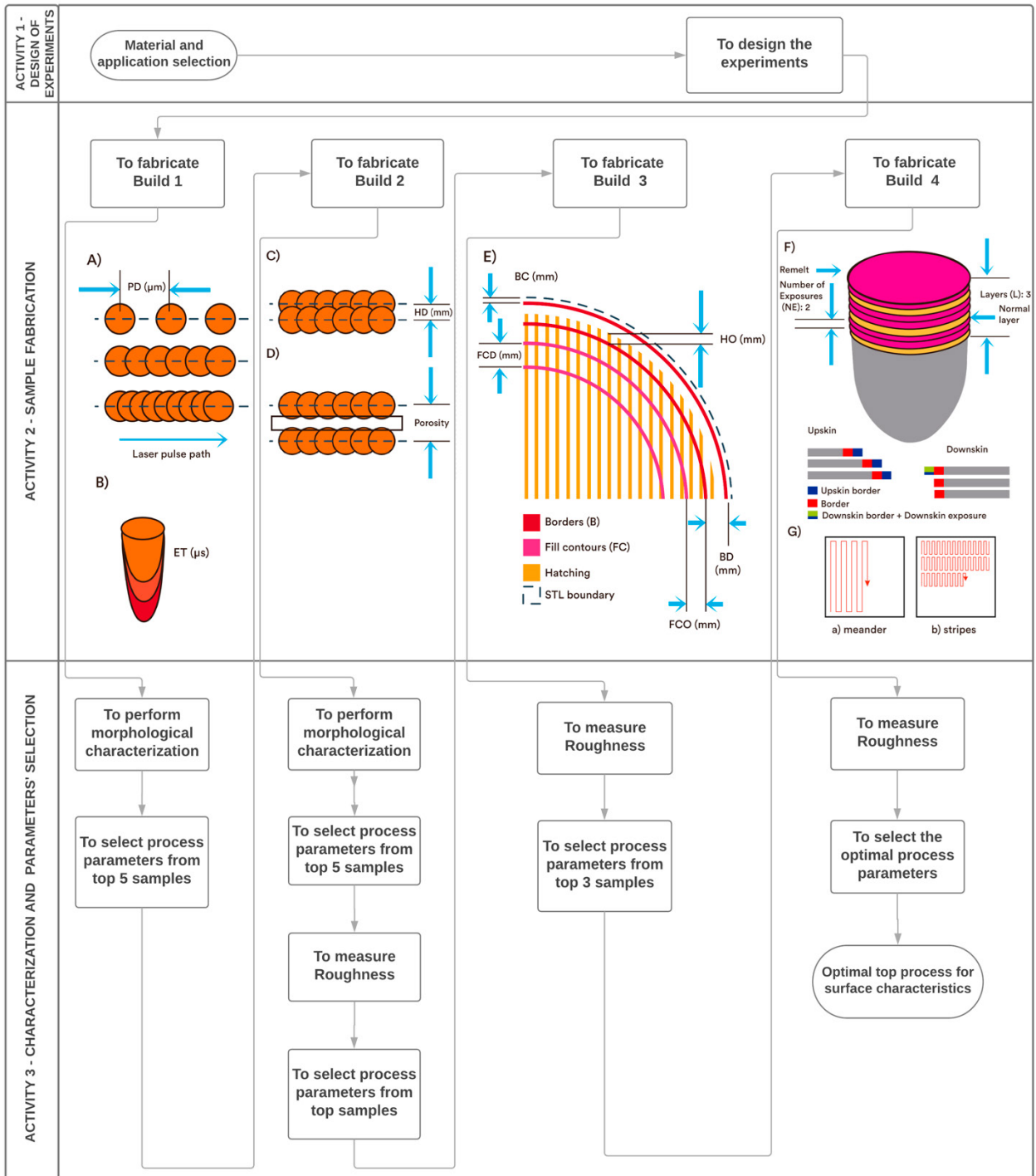


Figure 1. Graphical representation of parameters selection procedure for SLM process. A) Schematics of *PD* parameter variation, B) 3D view of laser spot and its *ET*, C) Schematics of the Hatch Distance (*HD*), D) Porosity related with a large *HD*, E) Schematics of Borders (*B*) and Fill Contour (*FC*) parameters and F) Schematics of the relationship of downskin and upskin configurations, G) Stripes and meander laser pattern.

### 3. Results and discussion

After the execution of the methodology described above, the experimental outcomes are explained, taking special attention in the description of the proposed stages, and explaining the characterization results of the fabricated *Builds*.

#### 3.1 Morphological characterization

At *Build 1*, thick squares were fabricated considering the *PD* and *ET* values shown in Table 1. With Eq. (1), Specific energy (*Q*) was calculated (Table 1). In gray, the parameters selected from the criteria of visual inspection are presented.

Table 1. Specific energy, *Q* (J/m<sup>2</sup>) for the fabricated samples of the first build. Selected combination of parameters is marked in gray.

<i>ET</i> ( $\mu$ s)	<i>PD</i> ( $\mu$ m)					
	20	40	60	80	100	120
20	3.4	1.7	1.13	0.85	0.68	0.57
40	6.8	3.4	2.27	1.7	1.36	1.13
60	10.2	5.1	3.4	2.55	2.04	1.7
80	13.6	6.8	4.53	3.4	2.73	2.27
100	17	8.5	5.67	4.25	3.4	2.83
120	20.4	10.2	6.8	5.1	4.08	3.4

Fig 2. shows how the criteria were followed for the selection of the top parameters. No continuous weld line was presented in Figure 2-A where the energy was insufficient to melt the powder. Another important factor is to obtain precise geometries, so the corners should be well defined, contrary as in Figure 2-B, in which several defects are noticed. This phenomenon is related to the viscosity of the weld line and to the excess of specific energy over the building platform. An over-melted weld line can be observed in Figure 2-C, where more *Q* is occurring given a *PD* at its highest value. With lower levels of *PD* and *ET*, good uniform weld lines can be obtained as shown in Figure 2-D. This outcome agreed literature results, where was found that *PD* has a more important effect in roughness than *ET* [17].

The relationship between the estimated *Q* and laser speeds was stable in a range of 0.59-1.69 m/s, with similar behavior as reported in literature [16]. Our study was also consistent with the work of Khairallah and Anderson, who proved that with lower speeds, the melt surface is much smoother than with higher speeds [18,19]. In addition, lower laser speeds require higher

specific energy, with effect on the surface tension that binds the melted particles and forms a smoother surface. This effect increases the contact with the building platform where heat transfer is faster, and cools the melted weld lines avoiding balling [18].

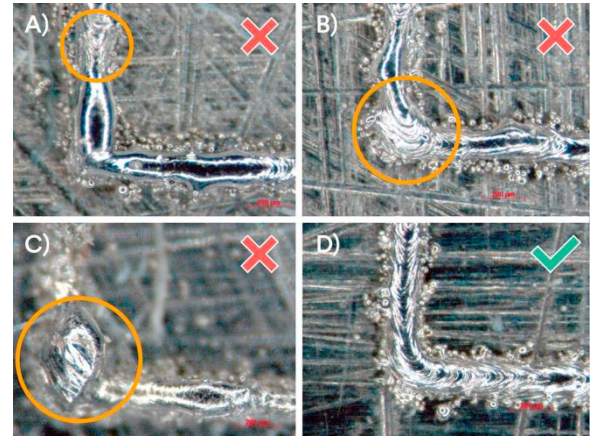


Figure 2. Weld lines. A) *ET*: 100  $\mu$ s *PD*: 60  $\mu$ m No continuous weld lines, B) *ET*: 60  $\mu$ s, *PD*: 20  $\mu$ m. Not uniform corners. C) *ET*: 120  $\mu$ s, *PD*: 120  $\mu$ m. Over melted weld lines. D) *ET*: 20  $\mu$ s, *PD*: 40  $\mu$ m Uniform weld line.

The main parameter for *Build 2* (*HD*) was varied as explained in the section 2.6, and Energy density was calculated with Eq. (2) as it is shown in Table 2. The best three combinations of parameters were selected (highlighted in gray), according to criteria for the stage of morphology characterization and roughness measurements explained before.

An under melted bulk with high amount of porosity is presented in Figure 3-A, where some particles are partially melted producing voids, due to a mismatch of the melt pool width and the higher hatch space, in agreement with the literature [20].

When a sample is over melted, a different shade and irregularities on the surface can be observed, which have been produced by the reflection of the particles on the surface (Fig 3-B). Some samples presented non-melted particles attached on the top surface (balling effect), as indicated with circles in Fig. 3-C. Finally, the test sample that presented the best surface morphology with uniform weld lines was obtained by using the next set of parameters: *PD*=20  $\mu$ m, *ET*= 20  $\mu$ s, and *HD*= 0.06 mm (Fig. 3-D).

Table 2. Energy density (GJ/m<sup>3</sup>) for the fabricated samples of the *Build 2*. Selected combination of parameters is marked in gray.

ET (μs)	PD (μm)	HD (mm)					
		0.06	0.08	0.10	0.12	0.14	0.16
20	20	56.67	42.5	34	28.33	24.29	21.25
20	40	28.33	21.25	17	14.17	12.14	10.62
40	60	37.78	28.33	22.67	18.89	16.19	14.17
80	80	56.67	42.5	34	28.33	24.28	21.25
40	120	18.89	14.17	11.33	9.44	8.1	7.08

From table 2, the combinations of parameters highlighted in gray presented a top surface without defects and smooth topography. When characterizing with SEM to provide redundancy, voids and balling effect were visible in figures 4-B and 4C respectively. In Fig. 4-C, different scales of gray can be observed, those are related with the excess of temperature on the top surface, in addition to distortion of the weld lines and holes. The best resultant surface quality can be seen in Fig. 4-D, in which well-defined weld lines can be observed, as a result of the process calibration for *Build 2*. It can be observed that an increase of *HD* leads to porosity due to the separation between weld lines (Fig 4-E).

### 3.2 Surface topography characterization

*Build 2* surface roughness (Ra) was measured on top and lateral surfaces of the samples with non-contact 3D profilometry, without additional post-processing. When modifying *HD*, geometric characteristics of the weld lines were also modified and as result surface topography was different. From the results shown in Table 3, low values of *HD* resulted in a decreased roughness. Decreasing *HD* had a direct influence in changes of thermo-physical conditions of the process where the laser interacts with the powder, the substrate, and the previous weld line.

*Build 3* was fabricated to have an improvement of the lateral surface roughness by setting border (*B*) and fill contour (*FC*) options, in combination with the best *PD*, *ET* and *HD* parameters found for the previous *Builds*. The set of experiments consisted in a variation of 1 to 2 for (*B*) values and 1 to 2 for (*FC*) values.

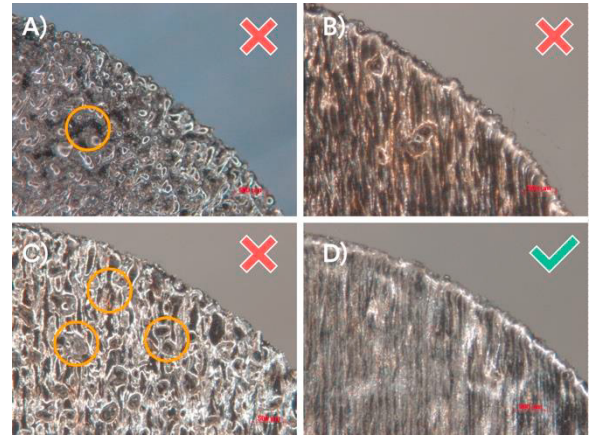


Figure 3. Bulk hatching A) ET: 40 μs, PD: 60 μm, HD: 0.12 mm Under melted bulk. B) ET: 40 μs PD: 120 μm HD: 0.06 mm. Over melted bulk, C) ET: 80 μs PD: 80 μm HD: 0.16 mm. Particles not melted over the top surface, D) ET: 20 μs PD: 20 HD: 0.06 mm Very uniform weld line.

Table 3. Roughness Ra (μm) on the top and side surfaces for *Build 2*.

Sample	ET (μs)	PD (μm)	HD (mm)	Ra [Top] (μm)	Ra [Side] (μm)
1	20	20	0.06	7.5	16.7
2	20	40	0.06	9.29	22.24
6	80	80	0.06	7.7	15.73

From the results of surface roughness measurement of *Build 3*, the lowest values were Ra=10.65 μm and 9.61 μm, with the variation of 1*B* and 1*FC*, 2*B* and 2*FC* respectively. Both sets of *B/FC* were obtained by using the bulk parameters from *Build 2* (higher values for *PD* and *ET*). The relationship between *B* and *FC* levels and the response (surface roughness) was not statistically significant after an Analysis of Variances, so it can be inferred that just by adding borders and fill contours the surface quality will be improved, independently to the programmed value of these variables.

For *Build 4*, parameters with a lower Ra (*NE*, *P* and *L* combinations) are presented in Figure 5. The top parameters for this *Build* were the set for top surface parameters of weld lines from *Build 1*, with the lateral surface parameters obtained from *Build 2*, and the parameters 2*B*-2*FC* from *Build 3*. *PD*, *ET* and *HD* values were fixed in order to provide an assessment of the variability of the results with the set of most significant parameters.

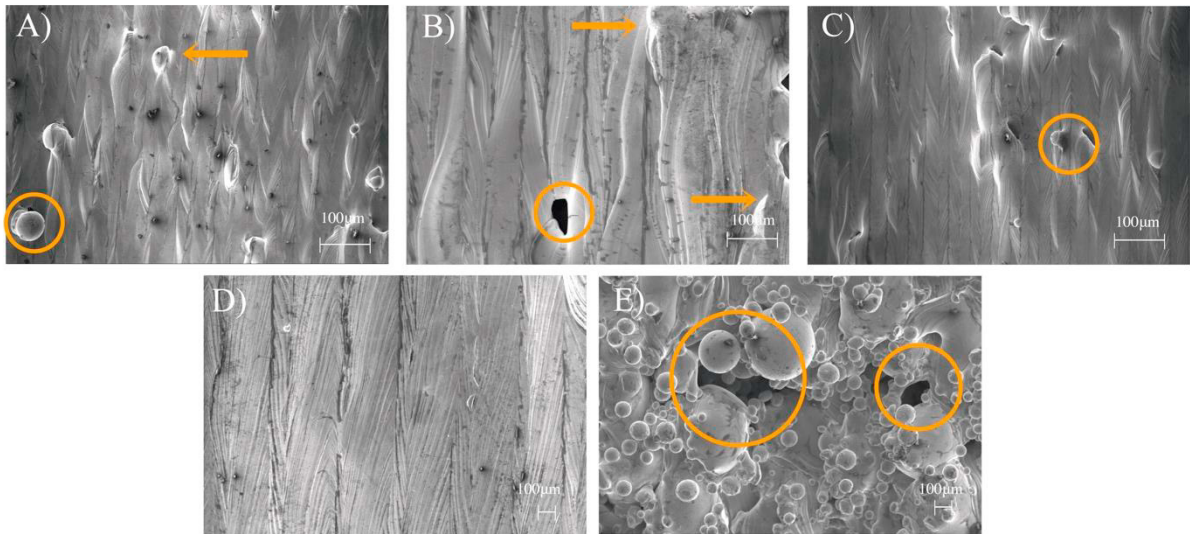


Figure 4. SEM Micrographs. A) Balling effect and particles concentration (50X). B) Distorted weld lines due to the excess of temperature (50X). C) Agglomeration of particles, and holes on the top surface (50X). D) Well defined weld lines (150X). E) Lateral view of a sample with porosity in circles open pores are presented (150X).

In Figure 5, several parameters combinations have the lowest surface roughness values, showing slight differences among others, but showing an improvement in comparison with the surface roughness values from *Build 2* (Table 3). Fig. 6 shows two topographies of the lowest surface roughness obtained from *Build 4* samples, on the top and lateral surfaces of the sample. From Fig. 6A can be observed the geometric variation of the surface, of about +/- 30 μm, which is a good descriptor of the flatness that can be achieved by this method.

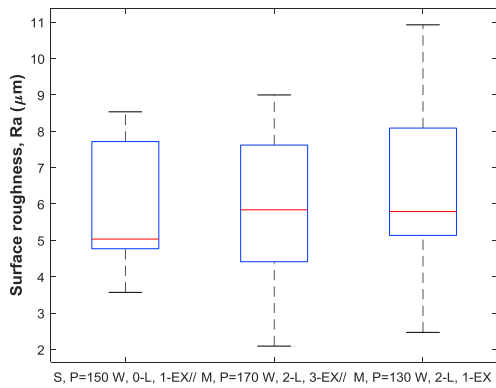


Figure 5. *Build 4* Samples with the lowest values of surface roughness, measured on the top surface.

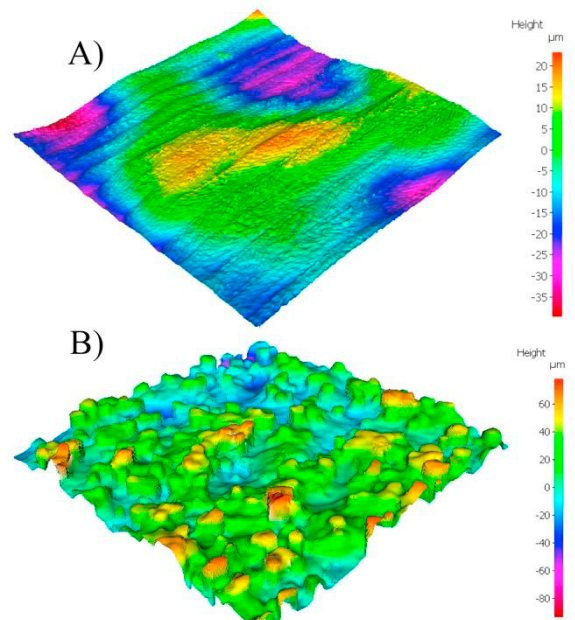


Figure 6. Surface topography of the selected parameters. A) Top surface, B) Lateral surface.

### 3.3 Tensile test

Fig. 7 shows mechanical strength test results of the specimens produced by SLM with optimized parameters for the lowest roughness on the top and lateral surfaces. All specimens presented UTS above 400 MPa, a yield stress ranging from 390 to 450 MPa in close agreement to the values found in literature [23]. Due the samples were fabricated with the same process parameters, the 33.6 MPa standard deviation on the results shows a low reproducibility of the experiment due to porosity. Pores are commonly found with spherical shapes, and can be formed by several reasons: incomplete melting, over melting and tension forces acting during the melting process [24].

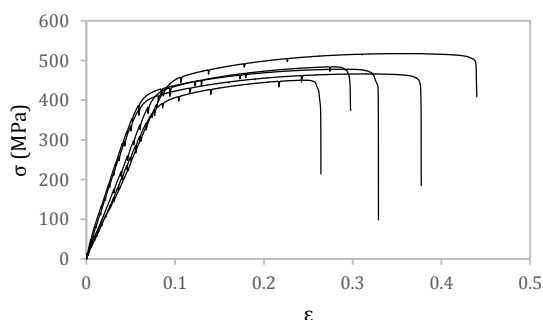


Figure 6. Data from tensile test for specimens built with the best set of parameters.

## 4. Conclusions

The methodology presented in this work leads to the selection of appropriate SLM process parameters, useful for the improvement of surface quality in the fabrication of stainless steel mechanical components. From this work, these parameters were successfully obtained from a design of experiments, which may be performed without carrying extensive experimentation and by using four testing trials. The approach presented here delivered the following tangible outcomes:

- The *Build 4* process configurations reached appropriate values of  $R_a$ : 5.81  $\mu\text{m}$  in the top surface and 9.61  $\mu\text{m}$  in the case of the side surface of the samples.
- The scan path itself may explain lower values of  $R_a$  obtained for the *M* scan technique. In meander

technique (*M*), the laser melts the top surface area line by line, fulfilling it; while, for the *S* scan technique, the laser fulfills such area with lines, built from smaller lines, which can create a weld line patterns in two axes, incrementing the roughness.

- Mechanical tests were made through specimens fabricated with these parameters resulting in mechanical properties commonly obtained from annealed bars obtained by casting. Inconsistency on the tests may be due to the inherent porosity obtained by the process. The porosity affects the stiffness of the material. A decrement on the modulus of elasticity can be related to an increase on the porosity of the sample. This porosity cannot be eliminated, but can be highly diminished, especially near the components surface. This can be done by modifying the *B*, *BC*, *FD* and the *FCD* parameters, assuring that the laser path fulfills the building area. Such parameters were tested, and effects on the density of the parts will be addressed on future work.

The results of this work presents guidelines for the process planning in SLM operations, however, there is the need to test the set of guidelines to other materials and building parameters in order to fully contribute in the understanding of the process in a real production environment. Furthermore, the addition of more process parameters like layer thickness modification will increase the comprehensiveness of this study

### Acknowledgements:

The authors want to acknowledge the support of The National Council on Science and Technology (CONACYT) grant for postdoctoral researchers, CVU#265858 and the National Lab in Additive Manufacturing, 3D Digitization and Computed Tomography (MADiT) LN280867 and LN294415. The Research Group in Advanced Manufacturing at Tecnológico de Monterrey provided additional support

### References:

- [1] I. Yadroitsev, P. Krakhmalev, I. Yadroitsava, Selective laser melting of Ti6Al4V alloy for biomedical applications: Temperature monitoring and microstructural evolution, *J. Alloys Compd.* 583 (2014) 404–409.
- [2] A. Sidambe, Biocompatibility of Advanced Manufactured Titanium Implants—A Review, *Materials*. 7 (2014) 8168–8188.

- [3] Z.M. Jin, J. Zheng, W. Li, Z.R. Zhou, Tribology of medical devices, *Biosurface and Biotribology*. 2 (2016) 173–192.
- [4] A. Yadollahi, N. Shamsaei, S.M. Thompson, D.W. Seely, Effects of process time interval and heat treatment on the mechanical and microstructural properties of direct laser deposited 316L stainless steel, *Materials Science and Engineering: A*. 644 (2015) 171–183.
- [5] M. Rombouts, J.P. Kruth, L. Froyen, P. Mercelis, Fundamentals of Selective Laser Melting of alloyed steel powders, *CIRP Ann.* 55 (2006) 187–192.
- [6] E. Yasa, J.-P. Kruth, Microstructural investigation of Selective Laser Melting 316L stainless steel parts exposed to laser remelting, *Procedia Engineering*. 19 (2011) 389–395.
- [7] J. Sun, Y. Yang, D. Wang, Parametric optimization of selective laser melting for forming Ti6Al4V samples by Taguchi method, *Opt. Laser Technol.* 49 (2013) 118–124.
- [8] M.-H. Hong, B.K. Min, T.-Y. Kwon, The Influence of Process Parameters on the Surface Roughness of a 3D-Printed Co–Cr Dental Alloy Produced via Selective Laser Melting, *NATO Adv. Sci. Inst. Ser. E Appl. Sci.* 6 (2016) 401.
- [9] K. Abd-Elghany, D.L. Bourell, Property evaluation of 304L stainless steel fabricated by selective laser melting, *Rapid Prototyping Journal*. 18 (2012) 420–428.
- [10] E. Liverani, S. Toschi, L. Ceschini, A. Fortunato, Effect of selective laser melting (SLM) process parameters on microstructure and mechanical properties of 316L austenitic stainless steel, *J. Mater. Process. Technol.* 249 (2017) 255–263.
- [11] W. Zhang, Y. Shi, B. Liu, L. Xu, W. Jiang, Consecutive sub-sector scan mode with adjustable scan lengths for selective laser melting technology, *Int. J. Adv. Manuf. Technol.* 41 (2009) 706.
- [12] B. Zhang, L. Dembinski, C. Coddet, The study of the laser parameters and environment variables effect on mechanical properties of high compact parts elaborated by selective laser melting 316L powder, *Materials Science and Engineering: A*. 584 (2013) 21–31.
- [13] O.O. Salman, A. Funk, A. Waske, J. Eckert, S. Scudino, Additive Manufacturing of a 316L Steel Matrix Composite Reinforced with CeO<sub>2</sub> Particles: Process Optimization by Adjusting the Laser Scanning Speed, *Technologies*. 6 (2018) 25.
- [14] K.G. Prashanth, L. Löber, H.-J. Klauss, U. Kühn, J. Eckert, Characterization of 316L Steel Cellular Dodecahedron Structures Produced by Selective Laser Melting, *Technologies*. 4 (2016) 34.
- [15] I. Yadroitsev, P. Bertrand, I. Smurov, Parametric analysis of the selective laser melting process, *Appl. Surf. Sci.* 253 (2007) 8064–8069.
- [16] M.M. Dewidar, K.W. Dalgarno, C.S. Wright, Processing conditions and mechanical properties of high-speed steel parts fabricated using direct selective laser sintering, *Proc. Inst. Mech. Eng. Pt. B: J. Eng. Manuf.* 217 (2003) 1651–1663.
- [17] J.A. Cherry, H.M. Davies, S. Mehmood, N.P. Lavery, S.G.R. Brown, J. Sienz, Investigation into the effect of process parameters on microstructural and physical properties of 316L stainless steel parts by selective laser melting, *Int. J. Adv. Manuf. Technol.* 76 (2015) 869–879.
- [18] S.A. Khairallah, A. Anderson, Mesoscopic simulation model of selective laser melting of stainless steel powder, *J. Mater. Process. Technol.* 214 (2014) 2627–2636.
- [19] T.H.C. Childs, C. Hauser, M. Badrossamay, Selective laser sintering (melting) of stainless and tool steel powders: Experiments and modelling, *Proc. Inst. Mech. Eng. Pt. B: J. Eng. Manuf.* 219 (2005) 339–357.
- [20] X. Zhou, K. Li, D. Zhang, X. Liu, J. Ma, W. Liu, Z. Shen, Textures formed in a CoCrMo alloy by selective laser melting, *J. Alloys Compd.* 631 (2015) 153–164.
- [21] I. Yadroitsev, I. Smurov, Surface Morphology in Selective Laser Melting of Metal Powders, *Phys. Procedia*. 12 (2011) 264–270.
- [22] E. Segura-Cardenas, E.G. Ramirez-Cedillo, J.A. Sandoval-Robles, L. Ruiz-Huerta, A. Caballero-Ruiz, H.R. Siller, Permeability Study of Austenitic Stainless Steel Surfaces Produced by Selective Laser Melting, *Metals*. 7 (2017) 521.
- [23] K. Saeidi, X. Gao, F. Lofaj, L. Kvetková, Z.J. Shen, Transformation of austenite to duplex austenite-ferrite assembly in annealed stainless steel 316L consolidated by laser melting, *J. Alloys Compd.* 633 (2015) 463–469.
- [24] G. Kasperovich, J. Haubrich, J. Gussone, G. Requena, Correlation between porosity and processing parameters in TiAl6V4 produced by selective laser melting, *Mater. Des.* 105 (2016) 160–170.

# Appendix B

Structural design optimization of knee replacement implants for Additive Manufacturing

December 2018

DOI: 10.1016/j.promfg.2019.06.222

LicenseCC BY-NC-ND 4.0





47th SME North American Manufacturing Research Conference, Penn State Behrend Erie,  
Pennsylvania, 2019

## Structural design optimization of knee replacement implants for Additive Manufacturing

Marinela Peto<sup>a</sup>, Erick Ramírez-Cedillo<sup>b,c</sup>, Adriana Hernández<sup>d</sup>, Hector R. Siller<sup>a\*</sup>

<sup>a</sup>Department of Engineering Technology, University of North Texas, Denton Tx., 76207, United States of America

<sup>b</sup>Tecnológico de Monterrey, Av. Eugenio Garza Sada #2501 Sur, Monterrey, N.L. 64849, Mexico

<sup>c</sup>Laboratorio Nacional de Manufactura Aditiva y Digital (MADiT), México

<sup>d</sup>Hospital Universitario "Dr. Jose' E. González", Monterrey, N.L., 64480, Mexico.

\* Corresponding author. Tel.: +1.940.565.2362. E-mail address: [Hector.Siller@unt.edu](mailto:Hector.Siller@unt.edu)

### Abstract

Recent developments in additive manufacturing (AM) have led the way to extraordinary opportunities in the development and fabrication of surgical implants due to advantages that AM offers. The study of structural design optimization (SDO) involves strategies such as topology optimization (TO), shape optimization, and size optimization to achieve a desired functionality for a given set of loads and constraints while optimizing specific qualities such as the structure weight or uniform stress distribution. Thus, integration of structural design optimization (SDO) and additive manufacturing (AM) is a powerful way for designing and fabricating lightweight medical implants that replicate the biomechanical properties of the host bones, and minimize stress shielding related problems. This study is focused in proposing a setup of a proper methodology for the rapid development of optimized surgical implants. A tibia intramedullary implant for an 8-year old osteosarcoma patient is designed and optimized, through TO in Abaqus/Tosca, to reduce the weight of the implant and minimize stress shielding related problems. A weight reduction of about 30 % was achieved from structural design optimization. The overall viability of the proposed design concept was validated using finite element analysis (FEA), and a stainless steel 316 L prototype was fabricated via SLM. After analysing results, in order to address osseointegration it is proposed that lattice structures to be incorporated in future work. In addition to that, there will be structural modifications for the implant to be able to adjust as the patient grows.

© 2019 The Authors. Published by Elsevier B.V.

This is an open access article under the CC BY-NC-ND license (<http://creativecommons.org/licenses/by-nc-nd/3.0/>)

Peer-review under responsibility of the Scientific Committee of NAMRI/SME.

**Keywords:** Knee arthroplasty; structural design optimization (SDO); topology optimization (TO); additive manufacturing (AM); stress shielding

### 1. Introduction

The human knee joint, which is the largest, most stressed and one of the most complex joint in the human body [1], consists of: femur, tibia, fibula, patella, cartilages, menisci, different ligaments and muscles. Knee arthroplasty is a surgical procedure that is used on diseased knee joints for diminishing pain or restoring function, and it can be performed as partial or

total knee replacement [2]. The earliest model of knee implant, the Tibial Plateau Prosthesis, was developed in the late 1960s by MCKeever [3] and consisted of a single metal component. Further improvements of knee prosthesis have been effected by important findings such as the introduction of "high-density" polyethylene plastic as a bearing surface in 1963, the popularization of the use of methyl- methacrylate as a fixation grout in 1960, and the Federal Drug Administration's (FDA's)

2351-9789 © 2019 The Authors. Published by Elsevier B.V.

This is an open access article under the CC BY-NC-ND license (<http://creativecommons.org/licenses/by-nc-nd/3.0/>)

Peer-review under responsibility of the Scientific Committee of NAMRI/SME.

10.1016/j.promfg.2019.06.222

approval of methyl methacrylate for general use in the United States in 1971 [4]. Since 1960 there was a continuous design evolution in total knee replacement satisfying new necessities [5] such as: anatomic congruence, articulation, less material wear cost reduction, and better resistance to weight and stresses. Today, knee implants have characteristics such as [6]: increased mobility; multiple components; closer to natural knee geometry; reduced wear; different materials and coatings.

The most commonly used metallic biomaterials for bone fixation implants are [7,8]: stainless steel (ISO 5832-1), pure titanium (ISO 5832-2) and its alloys, and cobalt-chromium-based alloys (e.g. CoCrMo). These materials demonstrate an adequate combination of [7–9] bio-functionality (e.g. modulus of elasticity, strength, ductility, hardness and toughness) and biocompatibility (corrosion resistance and cytotoxicity of corrosion products). However, there are problems associated with the use of metallic implants [10,11] such as a possible release of metal ions, inflammatory reactions, possible toxicity, and problems related to stress shielding and bone loss.

Commercial metallic implants are five to six times stiffer than bone [10], and when an implant is inserted into a bone canal, the loads that before were carried by the bone only, will be shared between the implant and the bone. According to Wolff's law the bone adapts in accordance with mechanical stress acting upon it. If the loading on the bone increases, the bone will remodel itself over time increasing bone mass to become stronger, and vice versa [12]. Therefore, when an implant is introduced/fixated to the bone, the bone is subjected to reduced stresses resulting in significant problems associated with stress shielding [11] such as less dense and weaker bone. In addition to that, high stiffness of metallic implants may lead to cracking issues, loosening or failure of the implant [11]. Thus, a lot of work has been continuously done on materials, design optimization, and manufacturing processes to find adequate approaches to reduce or avoid stress shielding at the bone-implant interface. The stiffness of an implant results from material properties (modulus of elasticity) and its structural design (shape and dimensions) [8]. Attempts have been made to produce implants with similar stiffness as bone by using plastic or carbon reinforced composites instead of metals. However, according to Richards and Perren [8]: implants with very low material stiffness do not as a rule offer an acceptable balance between biological and mechanical advantages. In many studies stress shielding phenomena is minimized by reducing the equivalent stiffness of metallic implants through the use of topology optimization (TO) [11], to create bone fixation designs with reduced material volumes.

Structural design optimization (SDO) methods provide the "best" values of system design and operating policy variables that will lead to the highest levels of system operating performance [13]. Topology optimization (TO), shape optimization, and size optimization are three broad categories of structural optimization, which focus on different aspects of the structure. TO can attain any shape within the design space, while shape and size optimization proceed with predefined configurations. Gradient-based or non-gradient-based mathematical techniques are used to achieve optimization. Today, there is a great interest in designing implants using topology optimization approach and producing them by AM

techniques due its complex shape options of fabrication [7]. Thus, incorporating AM constraints into SDO techniques has drawn increasing attention [14] due to its promising benefits.

Topology optimization, which refers to the internal member configuration of a structure, is the most commonly used structural design optimization method. Since its introduction in 1988 in a seminal paper by Bendsoe and Kikuchi, TO has developed enormously in many different directions, and based on literature findings of the last 25 years, the most popular TO methods are: (a) Evolutionary based algorithms (EA), (b) Solid Isotropic Microstructure with Penalization (SIMP), (c) Evolutionary Structural Optimization (ESO), (d) Soft-Kill Option (SKO), and (e) Level-set methods (LSMs) [15,16]. In biomedical applications TO is used to improve implants [17]. The difficulty of solving an optimization problem is related to [18] the number of variables present and the mixture of the variables (discrete, continuous, Boolean). Therefore, the aid of computational tools become crucial in solving an optimization problem, which typically involves iteration. The assistance of finite element analysis is usually required to determine the satisfaction of constraints in problem solving. Commonly, topology optimized parts are too complex to be fabricated using conventional manufacturing methods. Additive manufacturing (AM) [19], which represents a class of manufacturing processes for fabricating parts from digital information by joining materials usually layer upon layer, provides great opportunity to fabricate designs that result from TO.

AM of biomaterials [9,20] is making significant progress towards numerous biomedical applications due to numerous advantages [21,22] that AM offers compared to conventional manufacturing such as the ease in which medical imaging data can be converted into solid objects; high customizability; ability to fabricate highly complex shapes; good dimensional accuracy; clean build environment; and less material used. Design for Additive Manufacturing (DfAM) [23] has been used to take full advantages of the unique capabilities from AM processes in creating optimally complex and efficient designs featuring intricate geometries, pores, and lattice structures. The powder bed fusion (PBF) processes are of particular interest, especially for fabrication of metallic medical devices [20]. For instance, selective laser melting (SLM) [24] and selective electron beam melting (SEBM) [25] have huge potential in orthopedic implants [26] and in direct customizable manufacturing of metallic cellular scaffolds. Fused deposition modeling (FDM) and stereolithography have found many applications in manufacturing of polymeric biomaterials. Also, due their cost advantages both processes have been used to produce biomodels. Bose et al. [20] presented a comprehensive review of AM techniques used for fabrication of different medical devices and medically relevant materials.

The main objective of this study is to assess a methodology for the improvement and optimization of customized medical implants in general. A case study is presented where the proposed procedure is applied to design, optimize, and fabricate a tibia intramedullary implant for an osteosarcoma patient. A schematic representation of the overall process followed for development of a customized tibia intramedullary implant is presented in Fig. 1 and explained forward.

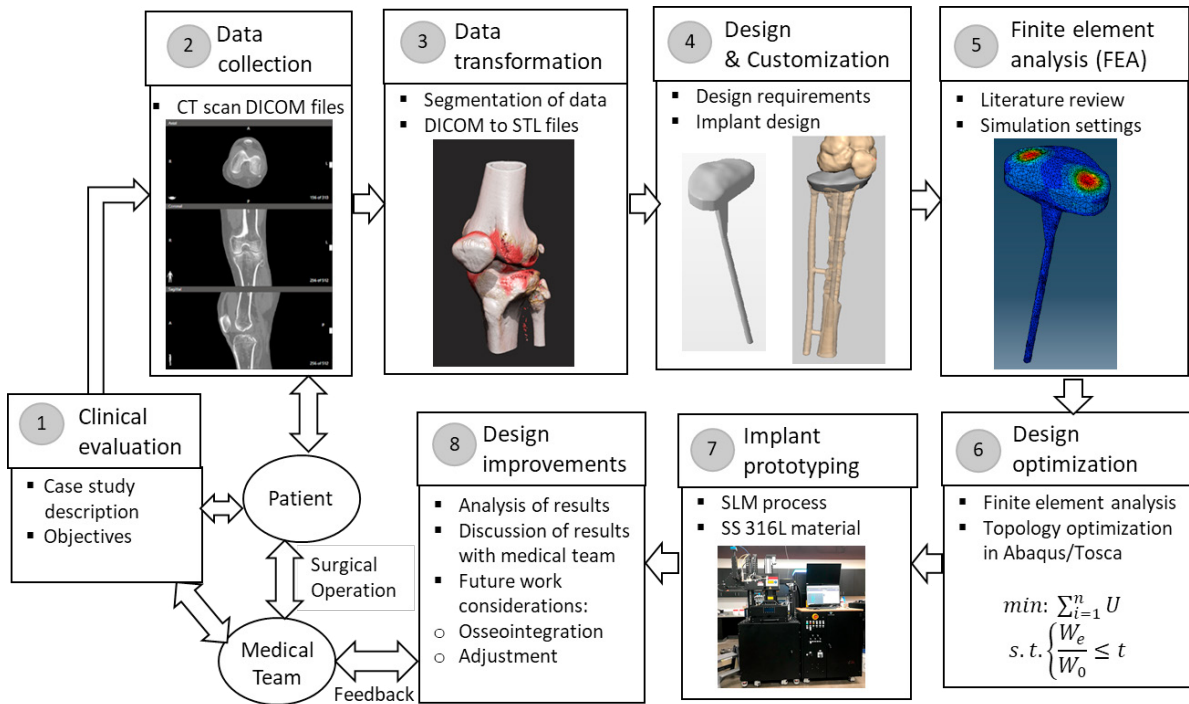


Fig. 1 Schematic of overall procedure for development of customized tibia intramedullary medical implant.

## 2. Materials and methods

The study was designated into five main stages which are: data preparation, customized design, structural optimization, prototype fabrication, and evaluation and future improvements. The data preparation phase involved CT scan data collection and data transformation. The transformation of data consisted of converting DICOM files into STL files, and furthermore STL files into IGES files. Evaluation phase incorporated virtual validation and frequent communication between medical team and engineering team. Finally, future design improvements were provided based on analysis of results and feedback from medical team. The next sections contain the explanation in more details of the entire processes and procedures used for this development.

### 2.1. Clinical evaluation

Case: An 8-year old child who is an osteosarcoma patient, had the tumor removed by surgical procedure from the right knee. Computed tomography (CT) scan and 3D joint images are presented in Fig. 2. The difference between the healthy knee and the diseased one is shown in Fig. 2, along with the original fixation plate. The weight of patient is 40 kg, and fixation method that will be used for the designed tibia intramedullary implant is press fit method.

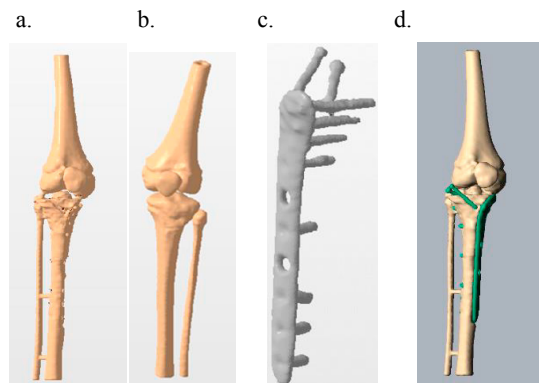


Fig. 2 STL images (not to scale) of (a) diseased right knee; (b) healthy left knee; (c) fixation plate; (d) original fixation assembly.

### 2.2. Imaging and scanning

After receiving a complete description about the case study and identifying objectives with medical team, data for the first step of the process chain for the tibia intramedullary implant design was collected from the patient through a CT scanner and processed as DICOM files (GE LightSpeed VCT 64 Slice CT). Since the design geometry of the implant is based on the CT scan of the healthy knee, the quality of the CT scan is crucial. Therefore, cuts of 1mm were performed to achieve accuracy on the STL.

### 2.3. Data transformation

After acquiring CT scan, the region of interest (tibia and femur bone) is identified and selected. The conversion of DICOM files into STL files is realized by means of a segmentation process using an open source software 3DSlicer 4.8 (Surgical Planning Lab, Harvard Medical School, Harvard University, Boston, USA).

### 2.4. Implant design and customization

The design requirements are identified based on three categories: (1) implant geometry; (2) implant fixation; (3) mechanical loads. The geometry of the designed implant is required to be as close as possible to the patient's tibia geometry. Therefore, the patient's healthy left knee files are used to construct the geometry of the implant in terms of mimicking the shape of the tibia. Modifications were made accordingly to the requirements from the medical team regarding dimensions and the capability of the designed implant to fit into the patient's bone. The implant was required to be bigger compared to the original tibia since the patient is a child and she will grow. The dimensions for height, width, and length of the implant are 152 mm, 62 mm, and 43 mm, respectively. The implant will be placed into the bone using press fit method by pushing the intramedullary stem inside the remaining bone and fastening with bone cement below the upper part of the implant. Geomagic Freeform [27] is used for sculpting and generating the initial biomodel design. Mechanical loadings applied in finite element analysis are defined based on literature review [28–33], and calculated accordingly for the body weight (BW) of the patient which is 40 kg.

### 2.5. Materials

Considering requirements of material properties used in surgical implants [9] such as biocompatibility, bulk properties and surface properties, it was decided to use stainless steel (SS) 316L for the simulation and fabrication of the part via selective laser melting (SLM) technology. Since stainless steel 316L is the most corrosion resistant when it comes in contact with biological fluid [34], it is commonly used in surgical procedures to replace biological tissue or to help stabilize a biological structure supporting the healing process [34]. The cortical-trabecular bone matrix material properties were selected based upon pre-existing published data [35]. Table 1 shows a summary of implemented material properties of the austenitic AISI SS 316 L [36] employed for simulation of the tibia intramedullary implant in Abaqus/CAE, and fabrication of the prototype. The chemical composition of SS316L used for SLM was Fe (Balance), Cr (17.5-18%), Ni (12.5-13.00%), Mo (2.25-2.50%), Mn (<2%), Si (<0.75%), Cu (<0.5%), N (<0.1%), O (<0.1%), P (0.025%), C (0.03%), S (0.01%) with an average particle size of 45±15 µm (LPW technology, Widness, UK). The mechanical properties of additively manufactured components using the austenitic AISI SS 316 L are shown in Table 2.

Table 1 Generic data – SS 316L-0407 wrought material [36].

	SS 316L-0407
Density [g/cm <sup>3</sup> ]	7.99
Thermal conductivity [W/mK]	15.6
Melting range [°C]	1,371-1,399
Coefficient of thermal expansion [K <sup>-1</sup> ]	16x10 <sup>-6</sup>
Poisson's Ratio	0.265

Table 2 Mechanical properties of additively manufactured components [36].

	As-Built Direction	
	Horizontal (XY)	Vertical (Z)
Upper tensile strength (UTS)	590 - 690 MPa	485 - 595 MPa
Yield strength	470 - 590 MPa	380 - 560 MPa
Elongation at break	25 - 55%	30 - 70%
Modulus of elasticity	197 GPa ± 4 GPa	190 GPa ± 10 GPa
Hardness (Vickers)	210 - 214 HV0.5	114 - 226 HV0.5

### 2.6. Finite element analysis

#### 2.6.1. Biomechanics of knee joint

The biomechanics of the knee joint are highly complicated [28] due to complexity related to: structural and mechanical properties of bone, cartilage and other soft tissues; forces experienced by certain structures during different activities and displacements occurring across multiple planes of motion; contact pressures, and joint kinematics. Therefore, there are various modelling approaches [28–31] that have been used for computation of knee forces. The determination of knee forces has been studied by mathematical modeling [28] or direct measurements using instrumented knee prosthesis [30]. Inverse dynamics and forward dynamics are the most popular mathematical modelling approaches used to relate knee kinematics and external forces to internal joint contact forces [29]. Since the accurate modeling of the knee hinders due to many factors, there are significant differences in predictions of knee forces due to diversity of approaches, modeling assumptions, and algorithms used [29]. Several software packages, such as Abaqus, Comsol, LS-Dyna, ANSYS, etc. are used for simulation and analysis work as an important tool for understanding knee biomechanics.

Due to different daily life physical activities, the peak forces acting on the tibia plateau vary significantly [29]. Previous studies have found, from measuring forces in distal femur replacement and transforming to the knee joint, that during typical normal level walking a resultant joint reaction force is equivalent to approximately three times the body weight (BW) [29,33,35]. Kutzner et al. [37] determined loading of knee joint during activities of daily livings using in vivo measurements. According to their in vivo experiments it was reported that the average peak resultant forces in terms of body weight (BW) from the highest to the lowest are: stair descending (3.46 BW), stair ascending (3.16 BW), level walking (2.61 BW), one legged stance (2.59 BW), knee bending (2.53 BW), standing up (2.46 BW), sitting down (2.25BW) and two legged stance (1.07BW). Therefore, for most daily activities according to

Kutzner et al. the resultant forces fall typically in the range of 220 – 350% BW [37].

### 2.6.2. Simulation settings

Normal walking activity consists of two main phases: stance phase and the swing phase. During the normal gait cycle approximately 60% of the time is compromised by stance phase and 40% by the swing phase. Morrison [38] has shown that the maximum joint loading occurs during the stance phase only. There are six sub-phases in the stance phase which are: heel strike, foot flat, mid-stance, heel off, and toe off. The loading used in this paper is based on the work of Morrison [38] who used analytical musculo-skeletal models and gait data for calculation of the maximum mean tibio-femoral compressive force. According to Morrison [38], the maximum mean tibio-femoral compressive force was calculated to be about three times body weight (BW) at the stance phase during level walking. The heel-strike stance phase during normal gate is simulated, where no ligament loading is applied to the system, using a static analysis with a dynamic load magnification factor adopted from the work of Bautista [35]. Furthermore pressure is used instead of concentrated loads guided by the work of Müller-Karger et al. [39].

The correction of the STL file geometry and the conversion from STL files into IGES files was done using SolidWorks 2017 (Dassault Systèmes SolidWorks Corporation, Waltham, MA, USA). The IGES files were imported to Abaqus/CAE 2018 (Dassault Systèmes Simulia Corp, Johnston, RI, USA) for the finite element analysis. A loading with a magnitude of 1,177.2 N (three times the patient's body weight) is distributed between the medial and lateral condyles, as constant distributed force, approximately covering contact areas of 178.6 mm<sup>2</sup> and 159.5 mm<sup>2</sup>, as shown in Fig. 3.

The encastre function is used for boundary condition in Abaqus/CAE 2018, simulating the situation where an assumed fully fixed condition exists [35]. This boundary condition function restricts the bottom faces and all the connecting nodes on it in three directions, preventing the displacement and rotation. A mesh with a total 80979 nodes and 55009 total number of quadratic tetrahedral elements of type C3D10, was used as shown in Fig. 3-a.

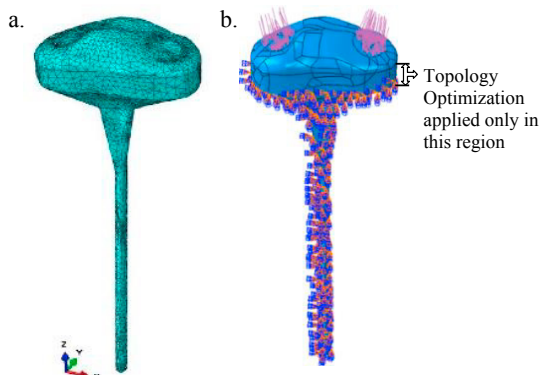


Fig. 3 (a) Meshed model of initial customized tibia intramedullary implant using C3D10 element type. (b) Loadings and boundary conditions applied on tibia intramedullary implant for FEA, and topology optimization work space.

## 2.7. Structural design optimization

### 2.7.1. Topology optimization using Solid Isotropic Material with Penalization (SIMP) approach

Topology optimization (TO) [13] of solid structures refers to the internal member configuration of a structure indicating the regions where holes will be located, the amount of the holes, their shapes, and the connectivity of the domain. TO is a mathematical method that determines the material placement in given domain to achieve a desired functionality for a given set of loads and constraints while optimizing for certain qualities such as minimal material usage or uniform stress distribution [23]. Guided by gradient computation or non-gradient algorithms TO builds on a repeated analysis and design update steps [40]. TO was introduced in 1988 in a seminal paper by Bendsoe and Kikuchi [41], and since then it has developed immensely in many different directions. General form of a TO problem to find the material distribution that minimizes an objective function  $F$ , subject to volume constraint  $g_0 \leq 0$ , and possibly other constraints  $g_i \leq 0$ ,  $i = 1, \dots, n$ , can be written as [42]:

$$\min: \quad \mathbf{F} = F(\mathbf{u}(\rho), \rho) = \int_0^\varphi f(\mathbf{u}(\rho), \rho) dV \quad (1)$$

$$\begin{aligned} g_0(\rho) &= \int_0^\varphi \rho dV - V_0 \leq 0 & (2) \\ \text{subject to: } & g_j(\mathbf{u}(\rho), \rho) \leq 0 \quad \text{with } j = 1, \dots, n \\ & \rho(x) = 0 \text{ or } 1 \quad \forall x \in \varphi \end{aligned}$$

The density variable  $\rho(\mathbf{x})$  describes the material distribution, and it can be either 0 (void) or 1 (solid) in any point in the design domain  $\varphi$ . Linear or non-linear state equations are satisfied by the state field  $\mathbf{u}$ .  $V$  represents the volume of the structure.

A widely used density-based TO approach is solid isotropic material with penalization (SIMP) [13,43,44] where the geometry is described via a material distribution which is typically discretized using element-wise invariable or nodal shape functions. SIMP is also known by different names such as density method, power law, or material interpolation. This method uses a “density”  $\rho(x)$  of a finite element as only design variable for each element [45]. The design variable and is normalized to have a value between zero (void) and one (solid). The relation between the design function “density”  $\rho(x)$  and properties of an isotropic material  $E_{ijkl}^0$  is given by power law as follows [13]:

$$E_{ijkl}(x) = \rho(x)^P \times E_{ijkl}^0, \quad P > 1 \quad (3)$$

$$\int \rho(x) d\psi \leq V; \quad 0 \leq \rho(x) \leq 1, \quad x \in \psi \quad (4)$$

The density is interposed between material properties  $E_{ijkl}(\rho = 0) = 0$  and  $E_{ijkl}(\rho = 1) = E_{ijkl}^0$ . The volume of the structure is evaluated as  $\int \rho(x) d\psi$ , where:  $\psi$  is the reference domain. “P” is a penalty factor that is used to penalize design variables not equal to 0 or 1, and its value is increased gradually from unity and is usually between 2 and 4 [46]. Tamimi et al. [11] employed a topology optimization using the SIMP method with minimizing the strain energy (maximizing the stiffness), constraining the volume. Tamimi et al. found out [11] that even though the TO used intended to increase stiffness

of each element, due to high percentage of volume reduction it was observed that the lightweight effect contributes to decrease of the equivalent stiffness of the component resulting in reducing stress shielding phenomena. Therefore, based on the work of Tamimi et al. [11], it was decided to use an objective function that minimizes strain energy for the topology optimization of the tibia intramedullary implant under a weight constraint.

2.7.2. Computational design optimization process

The design optimization process is performed using topology optimization method in Abaqus/Tosca Structure 2018 (Dassault Systèmes Simulia Corp, Johnston, RI, USA), and the workflow of the computational design optimization is presented in Fig. 4.

The objective function used is to minimize design response values of strain energy. The density update strategy used in Abaqus is normal, and initial density used the optimization product default. The values of minimum density, maximum density, and maximum change per design cycle used were 0.001, 1, and 0.25 respectively. The convergence criteria to be fulfilled is 0.001 for objective function delta criterion and 0.005 for element density delta criterion. A penalty factor of 3 is used for material interpolation technique.

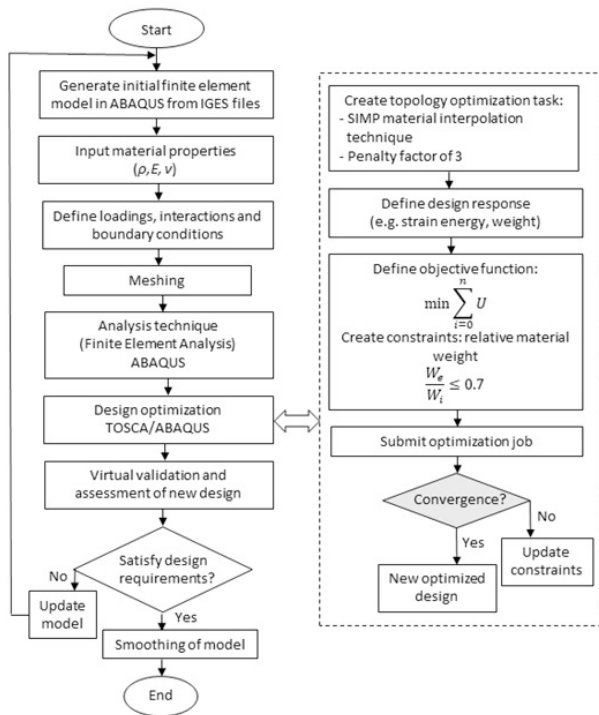


Fig. 4 Computational design optimization workflow using Abaqus/Tosca.

The weight constraint for a fraction of the initial value less or equal than 0.7 was used. This value was decided based on specified design requirements and topology optimizations attempts performed in Abaqus/Tosca. The stem of the implant is required to be solid and the geometry of the upper and bottom portions of the tibia to be kept the same as the original biomodel. Therefore, the workspace of the topology

optimization was determined to be the middle portion of the tibia (Fig. 3), which is 145 grams comprehending 45% of the entire weight of the implant which is 321.6 grams. Several topology optimization attempts were performed starting with values of weight constraint for a fraction of the initial value greater than 0.56, until it was found that the value of 0.7 was optimal for achieving weight reduction and allowing for further improvements such as incorporating lattice structures in the next phase. Load regions and boundary condition regions were kept frozen in the topology optimization task.

2.8. Implant fabrication using Selective Laser Melting (SLM)

The intramedullary tibia implant was fabricated by SLM using an Aconity 3D MIDI (Aconity GmbH, Herzogenrath, Germany). This system has a laser beam source (CW fiber laser with a  $\lambda = 1070$  nm) with a maximum power of 1000W and a diameter spot in a range of 80-500  $\mu$ m, and it has a working volume of a cylinder of 170 mm and height of 150mm. Argon was used as an inert gas to reduce corrosion, avoid contamination, and oxidation of the powder with a flow of 7 L/min. Laser process parameters are shown in Table 3.

Table 3 Selective laser melting process parameters.

Laser parameter	Value
Laser Power [W]	170
Laser modulation frequency [MHz]	1
Laser modulation width [ $\mu$ s]	10,000
Laser off delay [ $\mu$ s]	5
Laser on delay [ $\mu$ s]	20
Beam spot [mm]	0.08
Scanning laser speed [mm/s]	500

The optimized implant was converted into STL and introduced into Netfabb Premium 2019 (Autodesk, California, USA) for the generation of the layers (CLI files) where a layer thickness of 50  $\mu$ m was selected. The quad islands strategy was used as the laser scanning strategy with a quad height and width of 10 mm X 10 mm, a hatch distance of 0.12 mm, an initial and rotation angle per layer of 0° and 67° respectively and a translation layer of 0.001 mm. Quad islands strategy also named chessboard by other authors, and with a rotation angle between layers has been proved to have less presence of the residual stresses on the parts [47]. Even though roughness is higher [48] with this laser scanning strategy, the resulting topography can be suitable for the interaction between bones, and osteoblasts responded better in proliferation and adhesion with altered surfaces higher than 30  $\mu$ m [49]. The support material was designed with solid lines with small unions with the platform and the implant for easy removal. Each one of the CLI files was compressed into an ILT file and introduced into Aconity Studio (Aconity 3D, Herzogenrath, Germany) for its fabrication.

3. Results and discussion

3.1. Initial customized tibia intramedullary implant

Following the procedure that was described in section 2.4, an initial biomodel of tibia intramedullary implant was designed. The front view and the side view of the designed implant are shown in Fig. 5-a and Fig. 5-b respectively. The dimensions for the customized designed tibia intramedullary implant are: 152 mm high, 62 mm wide, and 43 mm long. The weight of the customized biomodel using stainless steel 316L material is calculated to be 321.58 g.

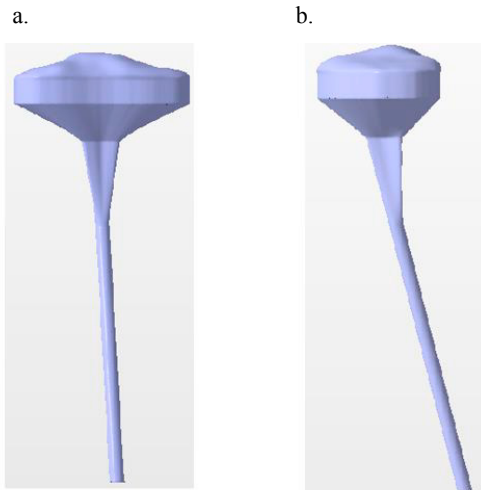


Fig. 5 Designed tibia intramedullary implant: (a) front view; (b) side view.

3.1.1. Finite element analysis initial customized tibia intramedullary implant

The finite element analysis (FEA) was performed in Abaqus using the loadings and boundary conditions defined in section 2.6. The results of finite element analysis for contour plots of displacement and von Mises stress are shown in

Fig. 6. From the displacement and Von Mises contour plots can be seen that the maximum magnitude of displacement is  $1.643 \times 10^{-4}$  mm and maximum Von Mises stress is 7.32 MPa.

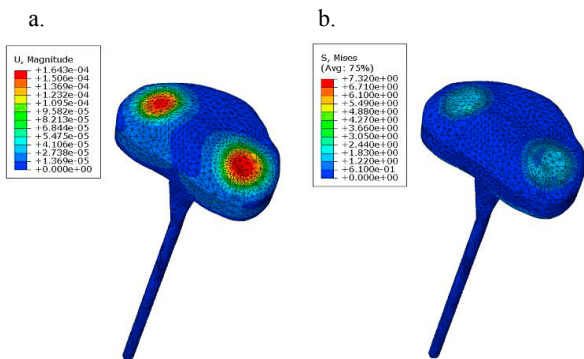


Fig. 6 Finite element analysis results before the optimization. (a) The displacement contour plot [mm]. (b) Von Mises contour plot [MPa].

3.2. Topology optimization results

TO was performed only for the top part (not for the stem), and the generated results are shown in Fig. 7. The weight of the implant is reduced by almost 30%, measuring a value of 225.38 g compared to initial weight of 321.58 g. This optimization sets the stage for further improvements that will be incorporated in the next phase, such as putting lattice structures in order to promote bone ingrowth and contribute to reduction of stress shielding problems. In addition to that, the implant will be post processed for further refinements.

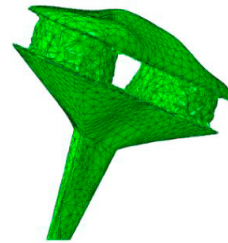


Fig. 7 Optimized tibia intramedullary implant.

3.2.1. Finite element analysis for optimized implant

The results of finite element analysis after the optimization are shown in Fig. 8, and as it can be seen from contour plots, the maximum magnitude of displacement is  $1.879 \times 10^{-4}$  mm and the maximum Von misses stress is 7.448 MPa.

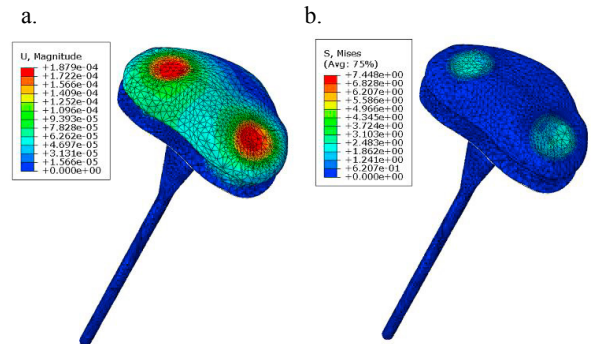


Fig. 8 Finite element analysis results after optimization. The displacement contour plot [mm] (left) and Von Mises contour plot [MPa] (right).

3.3. Comparison of FEA results for original and optimized tibia intramedullary implant

The comparison of finite element analysis results of original and the optimized model show not a significant change in the values of displacement and von Mises stress. The maximum magnitude of displacement increases from  $1.643 \times 10^{-4}$  mm for original model to  $1.879 \times 10^{-4}$  mm for the optimized model. Von Mises stress on the tibia intramedullary implant has also increased slightly from 7.32 MPa for original model to 7.448 MPa for optimized model. From the analysis and comparison of the results of FEA it can be stated that the topology optimization is beneficial for improvement of the implant by achieving a weight reduction of 30% while the maximum

magnitude of displacement and maximum von Mises stress increase only by 14.4% and 1.7 % respectively.

### 3.4. SLM processing for prototyping

The intramedullary implant was orientated lying to the platform to achieve a good surface topography in its interaction with the upper bone (femur). To start the process, the argon flow was controlled at the desired level and the chamber was pressurized with a total time of 45 minutes. During the SLM process, the powder was always well distributed over the platform with a platform offset of 0.05 mm and supply factor of 3 powder (3 times the layer thickness) without signs of warping on the edges of the implant, or over melted layers. The machine took 6 hours to produce the implant and 1 hour for the post-processing and cleaning. Figure 9 shows the resulted intramedullary tibia implant fabricated with SLM. The part has a bright metallic color, and it shows no defects on its surface or balling effect, no warping, or any deformation between the part and the building platform.

Also, in order to measure the surface roughness of the prototype fabricated via SLM, it was performed a surface characterization analysis with the aid of CHR 150, chromatic confocal sensor. Based on the conducted analysis, the value of surface roughness parameter Ra was found to be 9.63  $\mu\text{m}$ .



Fig. 9 Stainless steel 316L optimized tibia intramedullary implant fabricated via selective laser melting process.

### 3.5. Future design improvements

Compared to structural design optimization methods, the replacement of solid volumes by lattice structures may also offer robust solutions to different multi objective problems that involve unsureness of loading conditions [11]. Due to their high strength to weight ratio, lattice structures used in orthopaedic implants are found to be very beneficial for bone ingrowth stimulation (osseointegration) and reduction of problems related to stress shielding phenomena [50]. Furthermore, the geometry of lattice structures can be modified to accomplish certain levels of required performance. TO have been used by many researchers as an effective method in designing optimized unit cells that lead to several structural and functional improvements of orthopedic implants.

Therefore, in order to further improve the designed tibia intramedullary implant, lattice structures will be considered in future work. The results of topology optimization are valuable in identifying the regions where the material is not critical and therefore can be removed from the model. The optimized model will be used as a guide in taking the decision of replacing solid volumes with lattice structures in order to generate lighter design, while offering bone ingrowth simulation with suitable level of stiffness and energy absorption under static and dynamic loading.

Also, since the patient is a child, structural design modifications will be considered in future work allowing for adjustments of the implant as the patient grows.

## 4. Conclusions

This study has proposed a methodology that can be used for improvement of customized medical implants in general. A knee prosthesis case study is presented where the proposed procedure is applied to design, optimize, and fabricate a tibia intramedullary implant for an 8-year old osteosarcoma patient. Customization is focused on matching the geometry of the implant as close as possible to the original anatomy of the patient's tibia. In order to further improve the designed implant, structural design optimization is considered. Through performing a computational topology optimization, it was achieved 30% weight reduction. The process chain was validated virtually using Abaqus/Tosca, and a proof of concept is shown by fabricating a stainless steel 316L prototype via selective laser melting (SLM) process.

Future considerations for further improvement of tibia intramedullary implant are proposed. Lattice structures will be incorporated in next steps of implant design to stimulate bone ingrowth and reduce stress shielding phenomena. Further structural modifications will be also considered for implant adjustments due to patient growth.

## 5. Acknowledgments

The research was possible with the support of the College of Engineering of the University of North Texas, the Conacyt Mixed Scholarships Program and the Research Group in Advanced Manufacturing of Tecnológico de Monterrey. The authors acknowledge also the support of Dr. Adrian Negreros from Hospital Universitario and Dr. Carlos Cuervo from Hospital Zambrano Hellion.

## References

- [1] N.K. Sahu, A.K. Kaviti, A Review of Use FEM Techniques in Modeling of Human Knee Joint, *J. Biomimetics, Biomater. Biomed. Eng.* 28 (2016) 14–25.
- [2] S. Zanasi, Innovations in total knee replacement: New trends in operative treatment and changes in peri-operative management, *Eur. Orthop. Traumatol.* 2 (2011) 21–31.
- [3] D.C. McKeever, J.C. Pickett, THE CLASSIC: Tibial



- Plateau Prosthesis, Clin. Orthop. Relat. Res. 440 (2005) 4–8.
- [4] R.P. Robinson, The early innovators of today's resurfacing condylar knees, J. Arthroplasty. 20 (2005) 2–26.
- [5] A. Causero, P. Di Benedetto, A. Beltrame, R. Gisonni, V. Cainero, M. Pagano, Design evolution in total knee replacement: which is the future?, Acta Bio Medica Atenei Parm. 85 (2014) 5–19.
- [6] B.C. Carr, T. Goswami, Knee implants - Review of models and biomechanics, Mater. Des. 30 (2009) 398–413.
- [7] S.X. Xiaojian Wang Shiwei Zhou, Wei Xu, Martin Leary, Peter Choong, M. Qian, Milan Brandt, Yi Min Xie., Topological design and additive manufacturing of porous metals for bone scaffolds and orthopaedic implants: A review, Biomaterials. 83 (2016) 127–141.
- [8] S.M.P. R. Geoff Richards, Implants and Materials in Fracture Fixation, J. Chem. Inf. Model. 53 (2013) 1689–1699.
- [9] M. Saini, Implant biomaterials: A comprehensive review, World J. Clin. Cases. 3 (2015) 52.
- [10] K.S. Katti, Biomaterials in total joint replacement, Colloids Surfaces B Biointerfaces. 39 (2004) 133–142.
- [11] A.A. Al-Tamimi, C. Peach, P.R. Fernandes, A. Cseke, P.J.D.S. Bartolo, Topology Optimization to Reduce the Stress Shielding Effect for Orthopedic Applications, Procedia CIRP. 65 (2017) 202–206.
- [12] M.I.Z. Ridzwan, S. Shuib, A.Y. Hassan, A.A. Shokri, M.N. Mohammad Ibrahim, Problem of stress shielding and improvement to the hip implant designs: A review, J. Med. Sci. 7 (2007) 460–467.
- [13] M.P. Bendsoe, O. Sigmund, Topology optimization: theory, methods, and applications, Vasa. (2003) 370.
- [14] Y. Wang, Z. Kang, ScienceDirect A level set method for shape and topology optimization of coated structures, Comput. Methods Appl. Mech. Engrg. 329 (2018) 553–574.
- [15] M.Y. Wang, X. Wang, D. Guo, A level set method for structural topology optimization, Comput. Methods Appl. Mech. Eng. 192 (2003) 227–246.
- [16] N.P. Van Dijk, K. Maute, M. Langelaar, F. Van Keulen, Level-set methods for structural topology optimization: A review, Struct. Multidiscip. Optim. (2013).
- [17] O. Cansizoglu, O.L.A. Harrysson, H.A. West, D.R. Cormier, T. Mahale, Applications of structural optimization in direct metal fabrication, Rapid Prototyp. J. 14 (2008) 114–122.
- [18] T.E. Müller, E. van der Klashorst, A quantitative comparison between size, shape, topology and simultaneous optimization for truss structures, Lat. Am. J. Solids Struct. 14 (2017) 2221–2242.
- [19] N. Guo, M.C. Leu, Additive manufacturing: Technology, applications and research needs, Front. Mech. Eng. 8 (2013) 215–243.
- [20] S. Bose, D. Ke, H. Sahasrabudhe, A. Bandyopadhyay, Additive manufacturing of biomaterials, Prog. Mater. Sci. (2018).
- [21] T.D. Ngo, A. Kashani, G. Imbalzano, K.T.Q. Nguyen, D. Hui, Additive manufacturing (3D printing): A review of materials, methods, applications and challenges, Compos. Part B Eng. 143 (2018) 172–196.
- [22] M. Javaid, A. Haleem, Additive manufacturing applications in medical cases: A literature based review, Alexandria J. Med. (2017).
- [23] M.K. Thompson, G. Moroni, T. Vaneker, G. Fadel, R.I. Campbell, I. Gibson, A. Bernard, J. Schulz, P. Graf, B. Ahuja, F. Martina, Design for Additive Manufacturing: Trends, opportunities, considerations, and constraints, CIRP Ann. - Manuf. Technol. 65 (2016) 737–760.
- [24] B. Vandenbroucke, J.P. Kruth, Selective laser melting of biocompatible metals for rapid manufacturing of medical parts, Rapid Prototyp. J. 13 (2007) 196–203.
- [25] C. Körner, Additive manufacturing of metallic components by selective electron beam melting - A review, Int. Mater. Rev. 61 (2016) 361–377.
- [26] X.P. Tan, Y.J. Tan, C.S.L. Chow, S.B. Tor, W.Y. Yeong, Metallic powder-bed based 3D printing of cellular scaffolds for orthopaedic implants: A state-of-the-art review on manufacturing, topological design, mechanical properties and biocompatibility, Mater. Sci. Eng. C. 76 (2017) 1328–1343.
- [27] 3D SYSTEMS, Geomagic Freeform, (n.d.). <https://www.3dsystems.com/software/geomagic-freeform> (accessed September 21, 2018).
- [28] J. Nedoma, Mathematical and Computational Methods and Algorithms in Biomechanics : Human Skeletal Systems, Wiley-Interscience, Hoboken, N.J., 2011.
- [29] D.D. Lima, D.D. D'Lima, B.J. Fregly, S. Patil, N. Steklov, C.W. Colwell, Knee joint forces : prediction , measurement , and significance, Proc. Inst. Mech. Eng. H. 226 (2013) 95–102.
- [30] B. Heinlein, I. Kutzner, F. Graichen, A. Bender, A. Rohlmann, A.M. Halder, A. Beier, G. Bergmann, ESB clinical biomechanics award 2008: Complete data of total knee replacement loading for level walking and stair climbing measured in vivo with a follow-up of 6-10 months, Clin. Biomech. 24 (2009) 315–326.
- [31] D.E. Hurwitz, D.R. Sumner, T.P. Andriacchi, D.A. Sugar, Dynamic knee loads during gait predict proximal tibial bone distribution, J. Biomech. 31 (1998) 423–430.
- [32] K. Murase, R.D. Crowninshield, D.R. Pedersen, T.S. Chang, An analysis of tibial component design in total knee arthroplasty, J. Biomech. 16 (1983) 13–22.
- [33] D.A. Saravanos, P.J. Mraz, D.T. Davy, Shape Optimization of Tibial Prosthesis Components, Cleveland, 1993.
- [34] K. Kaur, Stainless Steel and Titanium in Surgical Implants, (2013) 3. <https://www.azom.com> (accessed December 10, 2018).
- [35] A.I. Bautista, A Finite Element Analysis of Tibial

- Stem Geometry for Total Knee, California Polytechnic State University, 2015.
- [36] LPW Carpenter Additive, Technical data sheet LPW 316L Stainless Steel, (2017) 1–2. <https://www.lpwtechnology.com/>.
- [37] I. Kutzner, B. Heinlein, F. Graichen, A. Bender, A. Rohlmann, A. Halder, A. Beier, G. Bergmann, Loading of the knee joint during activities of daily living measured in vivo in five subjects, *J. Biomech.* 43 (2010) 2164–2173.
- [38] J.B. Morrison, The mechanics of the knee joint in relation to normal walking, *J. Biomech.* 3 (1970) 51–61.
- [39] C.M. Müller-Karger, C. González, M.H. Aliabadi, M. Cerrolaza, Three dimensional BEM and FEM stress analysis of the human tibia under pathological conditions, *C. - Comput. Model. Eng. Sci.* 2 (2001) 1–13.
- [40] R. Cazacu, L. Grama, Overview of Structural Topology Optimization Methods for Plane and Solid Structures, *Ann. Univ. Oradea.* (2014) 17–22.
- [41] M.P. Bendsøe, N. Kikuchi, Generating optimal topologies in structural design using a homogenization method, *Comput. Methods Appl. Mech. Eng.* 71 (1988) 197–224.
- [42] O. Sigmund, K. Maute, Topology optimization approaches: A comparative review, *Struct. Multidiscip. Optim.* (2013).
- [43] M. Zhou, G.I.N. Rozvany, The COC algorithm, Part II: Topological, geometrical and generalized shape optimization, *Comput. Methods Appl. Mech. Eng.* 89 (1991) 309–336.
- [44] Y. Di Li, B. Kuang, J. Liu, SIMP-Based Evolutionary Structural Optimization Method for Topology Optimization, *Appl. Mech. Mater.* 651–653 (2014) 2237–2240.
- [45] D. Tcherniak, Topology optimization of resonating structures using SIMP method, *Int. J. Numer. Methods Eng.* 54 (2002) 1605–1622.
- [46] T.Y. Chen, Y.H. Chiou, Structural Topology Optimization Using Genetic Algorithms, *World Congr. Eng.* 3 (2013) 3–7.
- [47] D. Wang, S. Wu, Y. Yang, W. Dou, S. Deng, Z. Wang, S. Li, The effect of a scanning strategy on the residual stress of 316L steel parts fabricated by selective laser melting (SLM), *Materials (Basel).* 11 (2018) 1821.
- [48] E. Segura-Cardenas, E. Ramirez-Cedillo, J. Sandoval-Robles, L. Ruiz-Huerta, A. Caballero-Ruiz, H. Siller, Permeability Study of Austenitic Stainless Steel Surfaces Produced by Selective Laser Melting, *Metals (Basel).* 7 (2017) 521.
- [49] O. Zinger, K. Anselme, A. Denzer, P. Habersetzer, M. Wieland, J. Jeanfils, P. Hardouin, D. Landolt, Time-dependent morphology and adhesion of osteoblastic cells on titanium model surfaces featuring scale-resolved topography, *Biomaterials.* 25 (2004) 2695–2711.
- [50] D. Mahmoud, M. Elbestawi, Lattice Structures and Functionally Graded Materials Applications in Additive Manufacturing of Orthopedic Implants: A Review, *J. Manuf. Mater. Process.* 1 (2017) 13.
- [51] C. Beyer, D. Figueroa, Design and Analysis of Lattice Structures for Additive Manufacturing, *J. Manuf. Sci. Eng.* 138 (2016) 121014.

## Design and optimization of an orthopedic lattice-based hemiprosthesis for the proximal humerus.

E. Ramirez-Cedillo<sup>1,2</sup>, M. Peto<sup>1</sup>, H.R. Siller<sup>1</sup>

<sup>1</sup>Department of Engineering Technology, University of North Texas. Denton TX, 76207, United States of America

<sup>2</sup>Tecnologico de Monterrey, Escuela de Ingeniería y Ciencias. Av. Eugenio Garza Sada #2501 Sur, Monterrey, N.L. 64849, Mexico

### Introduction

Osteosarcoma is a form of cancer in bones that affects mostly the health of the humerus, the femur, and the tibia among other large bones. The surgical procedure to relieve pain or restore health conditions in the proximal humerus is called shoulder joint arthroplasty where an implant is collocated to promote structural fixation for the bone. In this clinical technique, metallic orthopedic implants are commonly used and the ones that available in the market are 5-6 times stiffer than bone [1]. The change in stiffness between metal implants and the bone will result in stress shielding problems when an orthopedic implant is introduced to the human body and will lead to weaker less dense bone [2]. The heavy weight of the implant will produce discomfort in performing daily activities. In order to not to have relative movement between the surface of the implant and the bone, the implant needs to be functionally and structurally integrated into the bone (osseointegrated) [3]. In this work, and for overcoming the challenges explained above, a contribution in the design and optimization of customized implants is presented, through a case study of a light-weight hemiprosthesis with lattices structures to treat proximal humerus cancer.

### Materials and Methods

The patient is a 46 years old male who suffered osteosarcoma in the proximal humerus near to the shoulder. The osteosarcoma affected only 10 cm of the upper part of the humerus according to Computed Tomography scans. For designing a hemoprosthesis, DICOM files were firstly analyzed, and the damaged part of the bone was removed from the imaging files using Geomagic Freeform (CAD software). Afterwards, the shape and complexity of the healthy mirror bone were replicated. After that, lattice-based optimization was performed to improve the performance of the implant, integration with the surrounding tissues, increase stiffness, and to reduce weight. The lattice structures were selected according to the interaction of its form and size with the cells looking for the best osseointegration. Finally, the hemiprosthesis was fabricated using powder bed fusion (Selective Laser Melting). The implant was fabricated by SLM using an Aconity 3D machine (Aconity GmbH, Herzogenrath, Germany). This system has a laser beam source (F-theta) with a maximum power of 1000W and a diameter spot in a range of 80-500  $\mu\text{m}$ . For its fabrication, a biocompatible material was used. Mechanical properties of the lattices structures were tested and geometric accuracy, surface quality, and corrosion resistance before implantation were measured.

### Results

Based on the requirements from the medical team, it was decided to divide the section into three sections named top, middle, and bottom, and the optimization is applied only on the middle portion of the implant. Fig. 1 shows the 3D model of the optimized shoulder hemiprosthesis.

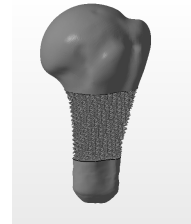


Fig. 1: Shoulder hemiprosthesis model with lattice structures.

Mechanical properties were enhanced through optimization routines where stress shielding was reduced according to simulations. The implant was successfully manufactured with powder bed fusion and in biocompatible material. Appropriate results were found on the corrosion, surface quality and geometric accuracy after running process parameters optimization strategies.

### Discussion and conclusion

An original biomodel was designed based on the requirements defined by the medical team. For further improving the implant in terms of weight reduction, osseointegration and minimizing stress shielding related problems, the optimization is performed based on lattice structures. Three different lattice unit cell configurations were designed, fabricated and tested. Based on compression mechanical testing previous results, the unit cell configuration with the best mechanical behavior was identified and selected to replace the solid middle portion of the implant, and the weight of the entire implant was reduced by 15%. It was shown that lattice structures are fabricated correctly using additive manufacturing with appropriate process parameters. Future work will be dedicated to the demonstration viability in the full implantation of the resulted prototype.

### References

- [1] K. S. Katti, "Biomaterials in total joint replacement," *Colloids Surf. B Biointerfaces*, vol. 39, no. 3, pp. 133–142, Dec. 2004.
- [2] M. I. Z. Ridzwan, S. Shuib, A. Y. Hassan, A. A. Shokri, and M. N. M. Ibrahim, "Problem of Stress Shielding and Improvement to the Hip Implant Designs: A Review," vol. 7, no. 3), Mar. 2007.
- [3] A. F. Mavrogenis, R. Dimitriou, J. Parvizi, and G. C. Babis, "Biology of implant osseointegration," *J. Musculoskelet. Neuronal Interact.*, vol. 9, no. 2, pp. 61–71, Apr. 2009.

# Appendix C

Mechanical Behavior of Lattice Structures Fabricated by Direct Light Processing With Compression Testing and Size Optimization of Unit Cells

November 2019

DOI: 10.1115/IMECE2019-12260

Conference: ASME 2019 International Mechanical Engineering Congress and Exposition

## MECHANICAL BEHAVIOR OF LATTICE STRUCTURES FABRICATED BY DIRECT LIGHT PROCESSING WITH COMPRESSION TESTING AND SIZE OPTIMIZATION OF UNIT CELLS

Marinela Peto<sup>1</sup>, Erick Ramirez-Cedillo<sup>2</sup>, Mohammad J. Uddin<sup>1</sup>, Ciro A. Rodriguez<sup>2</sup>, Hector R. Siller<sup>1</sup>

<sup>1</sup>University of North Texas, Denton, TX, United States of America

<sup>2</sup>Tecnologico de Monterrey, Monterrey, NL, Mexico

### ABSTRACT

Lattice structures used for medical implants offer advantages related to weight reduction, osseointegration, and minimization of stress shielding. This paper intends to study and to compare the mechanical behavior of three different lattice structures: tetrahedral vertex centroid (TVC), hexagonal prism vertex centroid (HPVC), and cubic diamond (CD), that are designed to be incorporated in a shoulder hemiprosthesis. The unit cell configurations were generated using nTopology Element Pro software with a uniform strut thickness of 0.5 mm. Fifteen cuboid samples of 25mm × 25mm × 15 mm, five for each unit cell configuration, were additively manufactured using Direct Light Printing (DLP) technology with a layer height of 50µm and a XY resolution of 73µm. The mechanical behavior of the 3D printed lattice structures was examined by performing mechanical compression testing. E-silicone (methacrylated silicone) was used for the fabrication of samples, and its mechanical properties were obtained from experimental tensile testing of dog-bone samples. A methodology for size optimization of lattice unit cells is provided, and the optimization is achieved using nTopology Element Pro software. The generated results are analyzed, and the HPVC configuration is selected to be incorporated in the further design of prosthesis for bone cancer patients.

Keywords: Additive Manufacturing, Direct Light Processing, Lattice Structures

### 1. INTRODUCTION

Lattice structures are one type of cellular materials [1]–[4] consisting of struts and nodes that are interconnected and arranged repetitively. They are used in various industries such as automotive, aerospace, biomedical, etc. due to their unique combination of properties [5]. One of the essential advantages

that lattice structures offer is high strength to weight ratio. Therefore, they are suitable for applications where extensive strain is required to occur before the yield due to low relative density. Furthermore, lattice structures can provide good properties in terms of energy absorption, insulation, acoustics, thermal conductivity, and weight reduction capabilities [1], [6], [7]. The geometrical configuration of unit cells can be modified in order to achieve a particular performance of the structure.

The implementation of lattice structures in the design of orthopedic implants [3] has led to significant benefits in addressing various issues related to the introduction of a medical implant into the bone. Metallic orthopedic implants that are available in the market are five to six times stiffer than the bone [8], and according to Wolff's law [9], the adaptation of the bone is directly related to the stresses acting on it. In the cases when the loading acting on the bone increases, the bone tends to restore itself with time increasing its mass and becoming stronger, and vice versa. Additionally, high stiffness and heavy weight of orthopedic implants may lead to loosening or failure of the implant, and discomfort on the patient while performing daily activities. Many researchers [10]–[12] have demonstrated successfully the potential of lattice structures on minimizing stress shielding and reducing the weight of the implant. Furthermore, lattice structures due to their porosity stimulate the structural and functional connection between the bone and the implant [3], [13], [14] providing mass transport requirements and proper mechanical properties. Thus, they have been used for the design of scaffolds in tissue engineering for substitutional or regeneration reasons [5].

In mesoscale (0.1-10mm), lattice structures are classified into three categories based on the degree of an order [6] as shown in Fig. 1. The first category, named the disordered lattice structure, consists of a random arrangement of unit cells with various configurations and sizes. The periodic (uniform) lattice

structure is the second category, and in contrast with the first category, it is composed by the repetition of a unit cell with specific configuration and size. Depending on the strut thickness, this category can be further divided into two subcategories: homogeneous and heterogeneous, having constant and variable strut thickness, respectively. In the third category, which is pseudo-periodic lattice structure, the configuration and size of each unit cell can be modified due to precise design requirements, while being part of the same general topology.

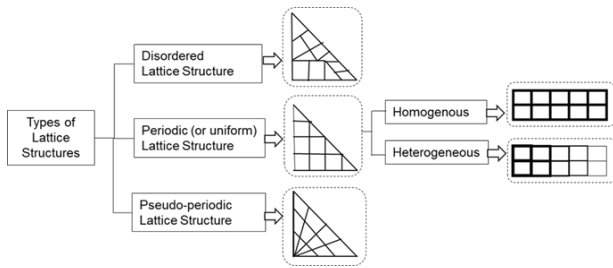


**Fig. 1 Types of lattice structures on mesoscale. Adapted from [6].**

The design and analysis of lattice structures is an iterative process that requires a lot of knowledge and human interaction in order to be able to explain the case study objectives [15]. Since the performance of a structure depends on the chosen pattern, researchers have been constantly focused on optimizing design variables of lattice structures such as strut thickness, orientation, material, topology, skins, etc. The lattice structures used for orthopedic implants can be divided based on the unit cell design [3], [16], [17]. The four groups are: (i) CAD-based unit cell design [18], [19]; (ii) image-based unit cell design [20]; (iii) topology optimized unit cell [21]; and (iv) implicit surface modeling unit cell [22].

Size optimization is a structural design optimization technique that is concerned with topology geometry and size optimization of components within a structure [23]. It defines the best component parameters for an optimal relationship between specific functionalities. Structural optimization problems are mostly nonlinear, and they consist of an objective function, constraints, and design parameters. Metaheuristic techniques have been successfully employed in solving size optimization problems. Few of the most popular metaheuristic techniques are [24]: Genetic Algorithms, Particle Swarm Optimization, Simulated Annealing, Artificial Bee Colony, Harmony Search Algorithm, Bing-Bang-Big Crunch Algorithm, etc.

The fabrication of lattice structures using conventional manufacturing methods can be challenging or even impossible in many cases. Additive manufacturing (AM) technology [25], which represents a class of manufacturing processes for fabricating parts in a layer by layer manner from digital information, offers excellent opportunities [26], [27] for fabrication of lattice structures related to ability to fabricate highly complex shapes, high resolution, clean build environment, less material used, and low cost. The most used AM processes for fabrication of biomaterials [28] are powder

bed fusion (PBF), direct energy deposition (DED), binder jetting (BJ), vat polymerization (VP), and materials extrusion (ME). Recently, there is a significant interest in the integration of lattice structures design and additive manufacturing. Design for AM (DfAM) [26] has been developed to fully exploit the advantages of AM in creating optimal complex and efficient designs featuring lattice structures. Researchers [15], [29]–[31] have worked on proposing the design and optimization methodologies with AM constraints. Direct Light Printing (DLP) also known as Direct Light Processing, is a type of vat photopolymerization AM process that uses an ultraviolet (UV) light to selectively cure the liquid photopolymer in a vat [32]. Compared to other AM processes such as SLS, FDM, and SLA, the DLP is acknowledged as an AM technique that has low cost and large throughput [33]. Additionally, DLP technique has the capability to produce structures with high complex shapes with highly resolution, typically down to 30  $\mu\text{m}$  layer thickness [32]. Furthermore, since the process takes place in a vat of liquid material, the requirement of support structures for hollow configurations is minimal, which makes this process an optimal technique for fabrication of lattice structures [33].

The objective of this study is to investigate the mechanical behavior of three different lattice unit cell configurations, in order to select the most proper configuration for its use in the design of lightweight implants, specifically a shoulder hemiprosthesis of a real patient suffering bone cancer, and its further utilization in other customized implants, as a practical solution for enabling osseointegration and mechanical resistance. The three-unit cell configurations designed are tetrahedral vertex centroid (TVC), hexagonal prism vertex centroid (HPVC), and cubic diamond (CD). The lattice structures design process is explained in section 2, along with direct light processing (DLP), which is the AM technique used for the fabrication of 15 silicone cuboid samples. Section 3 presents experimental results and discussion of mechanical testing and size optimization of unit cell lattice structures. Finally, the summary of the performed work is obtained in section 4.

## 2. MATERIALS AND METHODS

### 2.1. Materials

The material that is used for the fabrication and optimization of lattice structures is E-Silicone (methacrylate silicone) from EnvisionTec. The lattice structures were fabricated with a layer thickness of 50  $\mu\text{m}$ . The material properties provided by the manufacturer are shown in Table 1. In order to provide mechanical properties such as Young's modulus, shear modulus, and maximum strength needed for the simulation and optimization of unit cell lattices, tensile testing was performed as explained in section 2.2.5.

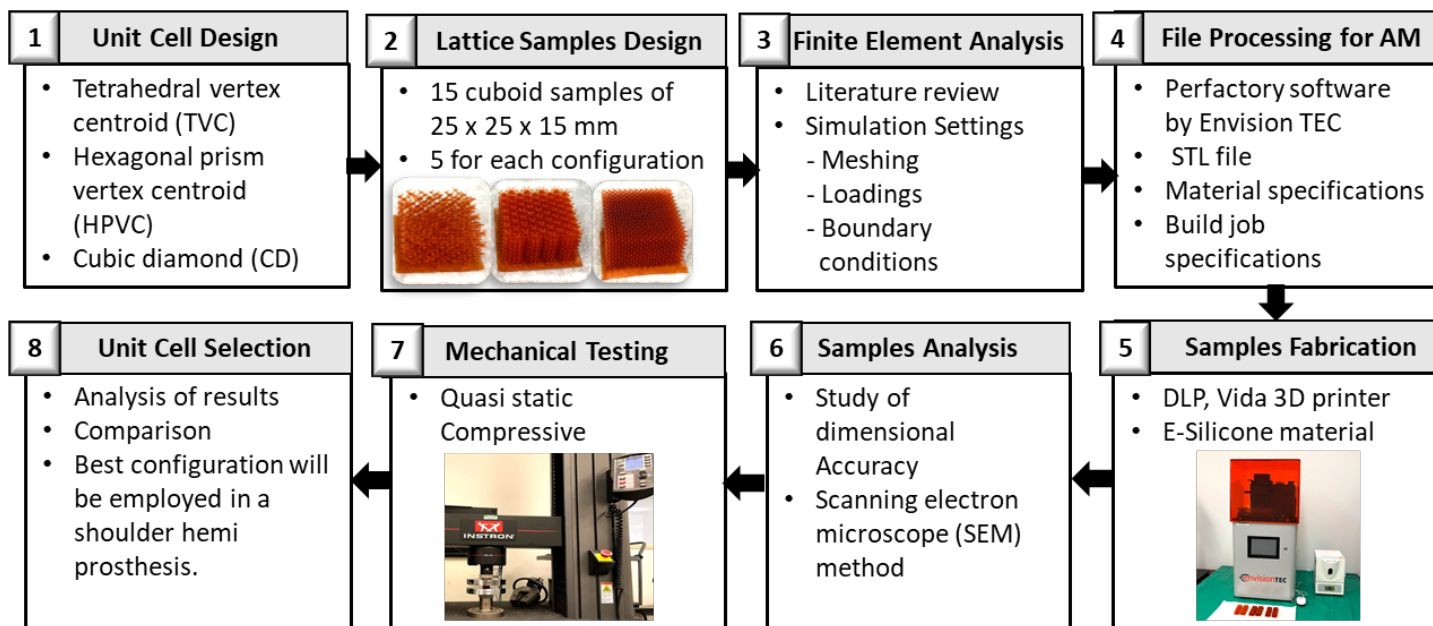


Fig. 2 Schematic of overall procedure followed for study of (i) Tetrahedral vertex centroid (TVC); (ii) Hexagonal prism vertex centroid (HPVC); and (iii) Cubic diamond (CD) unit cell configurations fabricated using DLP.

Table 1. Properties of E-Silicone from envisionTEC.

Description	Value
Material Density	170-220 cP at 30°C
Viscosity	1.05-1.15 g/cm <sup>3</sup>
Projector Brightness	500 mW/dm <sup>2</sup>

## 2.2. Methodology

The overall methodology followed for this study consists of unit cell design, lattice structures design, file preparation for AM, samples fabrication, mechanical testing, and selection of best unit cell configuration that will be used for a shoulder hemiprosthesis. A schematic of the overall process is shown in Fig. 2, and each step is explained in detail in the following sections.

### 2.2.1. Unit Cell Lattice Design

The unit cell lattice configurations were generated using nTopology Element (nTopology, New York, NY, USA). The dimensions for the unit cell used are 2 mm × 2 mm × 2 mm. The selection of 2mm unit cell size was based upon the findings of Yan et al. [34] stating that the yield strength and the Young's modulus decrease with the increase of the size for the unit cell configuration used. Tetrahedral Vertex Centroid (TVC), Hexagonal Prism Vertex Centroid (HPVC), and Cubic Diamond (CD) were the three-unit cell configurations generated using nTopology as shown in Fig. 3.

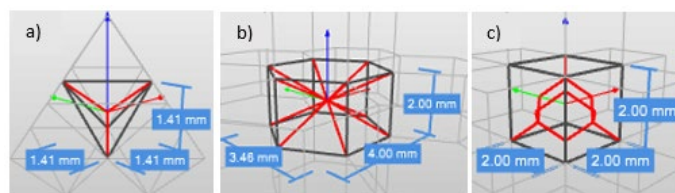
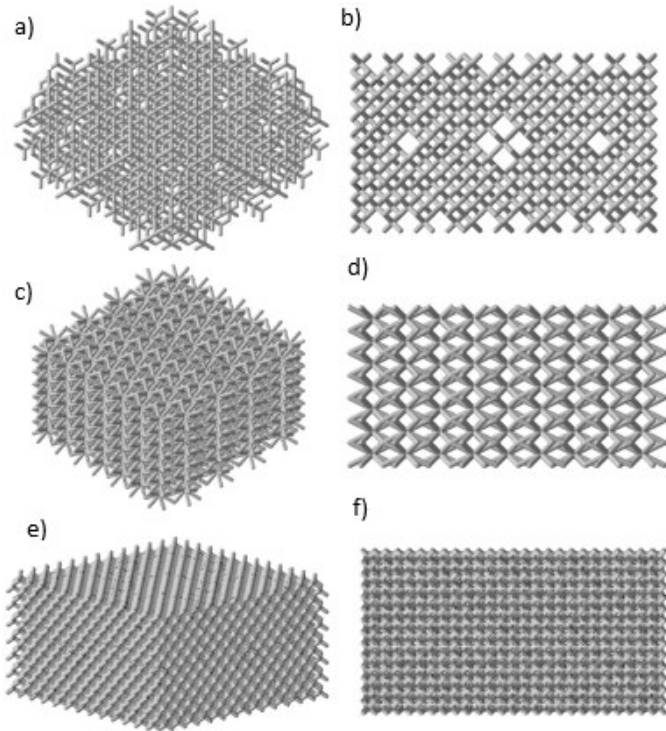


Fig. 3 Lattice unit cell configurations. (a) Tetrahedral vertex centroid (TVC), (b) Hexagonal prism centroid (HPC), and (c) Cubic diamond (CD).

### 2.2.2. Design of Cuboid Lattice Samples

Cuboid samples of 25 mm × 25 mm × 15 mm, containing the different unit cell lattice configurations, were designed in Netfabb (Autodesk, Mill Valley, CA, USA) and were exported in nTopology Element. A uniform thickness of 0.5 mm was used for the model after selecting the lattice generation rule for the configuration of the unit cell. The meshing was performed using parameters of 0.8, 0.1, and 0 for mesh resolution, node smoothing, and adoptively factor, respectively. The final step involved the export of mesh into a STL file. Isometric views and front views of 3D models are shown in Fig. 4.



**Fig. 4 Models of samples for each unit cell configuration. Tetrahedral vertex centroid: (a) isometric view, (b) front view. Hexagonal prism centroid: (c) isometric view, (d) front view. Cubic diamond: (e) isometric view, (f) front view.**

### 2.2.3. AM File Processing

The file preparation for direct light printing (DLP) was performed using Perfactory 3.2.3508 (envisionTEC, Dearborn, MI, USA) software. Subsequently, a STL (stereolithography) file was loaded on the job page that was created using the E-silicone material properties, and in order to optimize the space on the build plate, three samples were placed using 3mm spacing between them. Support structures were not needed for any of the created jobs. The last step involved exporting the job as an STL file.

### 2.2.4. Fabrication of Samples

The fabrication of samples was achieved by direct light processing (DLP) using a Vida 3D printer from Envisiontec (EnvisionTEC, Dearborn, MI, USA). DLP is a vat photopolymerization (VP) process, defined as an AM process that uses an ultraviolet (UV) light to selectively harden a liquid photopolymer in a vat, with the aid of CAM/CAD software, while the platform moves by the layer thickness. A curing oven was also used to cure the photopolymer resin. The user of the software, when needed, adds structural supports. This AM technology was selected for printing lattice structures due to the advantages that this process offers, such as good resolution for the printed parts and high building speed [35]. This printer uses a high-resolution projector performing at  $1920 \times 1080$  pixel resolution using a custom UV LED as a light source. It has a volumetric envelope of  $140 \text{ mm} \times 79 \text{ mm} \times 100 \text{ mm}$ . The

fabricated samples are shown in Fig. 5. The average weights were calculated to be 1.36, 3.68, and 4.5 gr with a standard error of 0.0257, 0.0578, and 0.205 for TVC, HPVC, and CD samples, respectively.

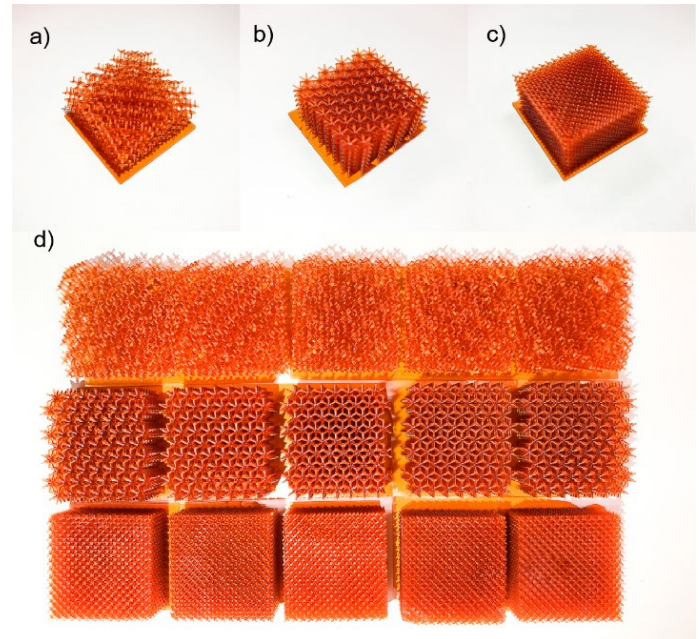


**Fig. 5 Lattice structures fabrication. (a) Tetrahedral Vertex Centroid (TVC); (b) Hexagonal Prism Vertex Centroid (HPVC); (c) Cubic Diamond (CD); (d) Total of 18 fabricated E-Silicone samples using DLP.**

### 2.2.5. Mechanical Testing

#### 2.2.5.1. Tensile Test

The E-silicone tensile samples shown in Fig. 6 were designed in Solidworks (Dassault Systèmes Solidworks Corp., Waltham, Ma) using the standard ASTM D 638-14 (Type 5) [34]. Three different set of samples were fabricated at different orientations relative to the building plate:  $0^\circ$ ,  $90^\circ$  and with a customized orientation.

They were fabricated using the same procedure explained in section 2.2.4, in which four samples of each configuration were made with a width range of 3.21-3.4 mm and a thickness range of 3.25-3.28 mm. The customized oriented samples (DLP oriented) were collocated in the building plate oriented in such way to reduce the cross-sectional area (2 rotations, one in the Y-axis of  $60^\circ$  and the other by  $30^\circ$  in the X-axis), which is directly proportional to the forces involved in the undesired adhesion of the part into the resin tank. Therefore, parts will be always oriented to avoid this frequent issue related to vat photopolymerization technologies. A universal testing machine, Instron® 3365 Tensile Tester (Instron Corporation, Nordstrom, MA, USA), was used to test the samples that were mounted between the grippers. The load applied to the lattice structures was 5kN and with the speed of the test set at 50 mm/min.



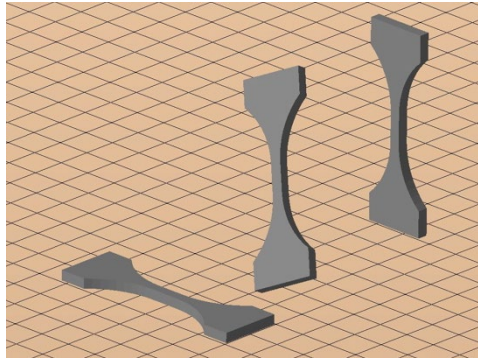


**Fig. 6** From left to right. 0°, DLP oriented and 90° E-silicone tensile samples.

### 2.2.5.2. Compression Mechanical Test

An Instron ® 5982 Dual Column Floor Beam Tensile Testing machine (Norwood, MA, USA) was used to carry out the mechanical compression test. Fifteen (15) samples were selected (5 CD, 5 TVC, 5 HPVC) for the test shown in Fig. 5. The compression test was performed according to ASTM D638-14 [36]. The maximum load capacity was 100 kN, and the frame movement was 3 mm/min. The load cells in general, are electrically calibrated, self-identifying, and rationalized. In order to avoid non-uniform loading on the lattice structure, the samples were set on the center of the disk. The deformation was recorded to visualize any particular feature at that moment on the compressive stress-compressive strain curve. For this study, cross-sectional areas were defined at the cross-section of the half of the sample with values of 2.08 cm<sup>2</sup> (CD), 1.59 cm<sup>2</sup> (HPVC), and 1.55 cm<sup>2</sup> (TVC). These areas were obtained by dividing the model into slices using additive manufacturing and design software Netfabb ®.

### 2.2.6. Size Optimization of Lattice Unit Cell

The size optimization of lattice unit cells was performed using nTopology Element Pro software. The procedure started with importing a STL file for a 2 mm × 2 mm × 2 mm cuboid model. Three design rules (TVC, HPVC, and CD) were used for lattice generation with a ruled scale of 2 × 2 × 2, followed by the selection of wrap to fit option. The lattice is thickened uniformly using 0.5 mm. The meshing was performed using a 0.8 mesh resolution and 0.1 node smoothing. A study for lattice size optimization was created with the predefined loading, boundary conditions, and optimization task. Point loads of 1N were applied on the Z direction, as shown in Fig. 7. A boundary condition restricting movement in Z direction was used for the simulation, and stress was used for the optimization objective. The mechanical properties used for simulation were derived from the performed tensile testing. The Young's modulus and shear modulus for the E-Silicone material employed in the analysis were 1.6526 GPa, and 656 MPa respectively. The maximum strength used was 66.6822 MPa. The number of iterations was kept 25 for the analysis. The diagram of the workflow for the lattice unit cell design and optimization is shown in Fig. 8.

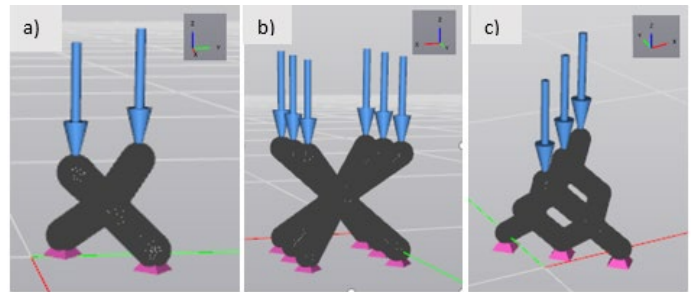


**Fig. 7** Loading and boundary conditions applied for size optimization of lattice unit cells. (a) Tetrahedral Vertex Centroid (TVC); (b) Hexagonal Prism Vertex Centroid (HPVC); (c) Cubic Diamond (CD).

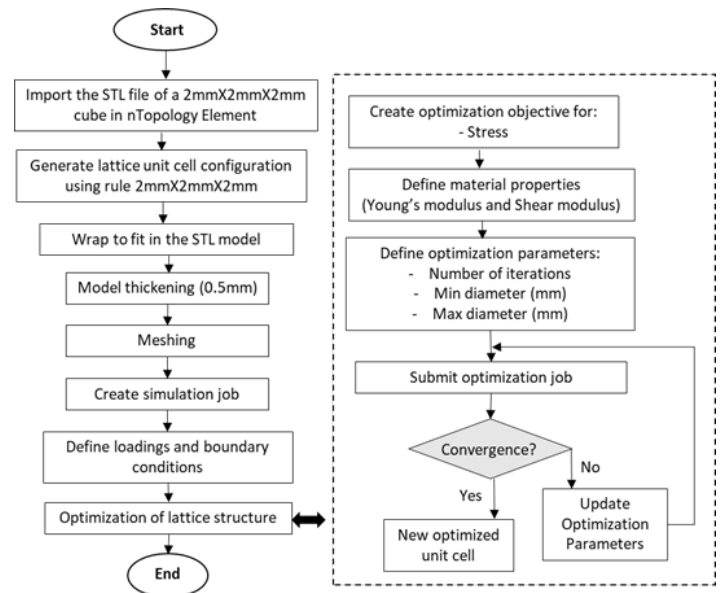


**Fig. 8** Unit cell design size optimization process using nTopology Element Pro.

## 3. RESULTS AND DISCUSSION

### 3.1. Tensile Mechanical Test

Results of the tensile test samples produced by DLP with a layer thickness of 50 µm are shown in Fig. 9. The cross-sectional areas were considered at the half of each of the tensile samples.

To understand the behavior of the anisotropy of the samples, parts were fabricated, as explained above, with different orientations: 0°, 90°, and customized orientation. For the samples with 0° and 90°, it was found a Young's modulus of 0.758 GPa and 0.756 GPa, respectively. The UTS in both orientations were 50.53 MPa and 50.6 MPa, which is approximately less by 25% in comparison with the exhibited in the DLP oriented samples. They presented an average UTS of 66.682 MPa with a standard deviation of 2.44 MPa, a Poisson ratio of 0.2596, an average modulus of young of 1.6526 GPa with a standard deviation of 0.066 GPa. From this experiment data, the reduction of the cross-sectional area during the printing process can result in the

increment of the elastic properties of the parts, which is a desired property in the design of bio-mechanical implants.

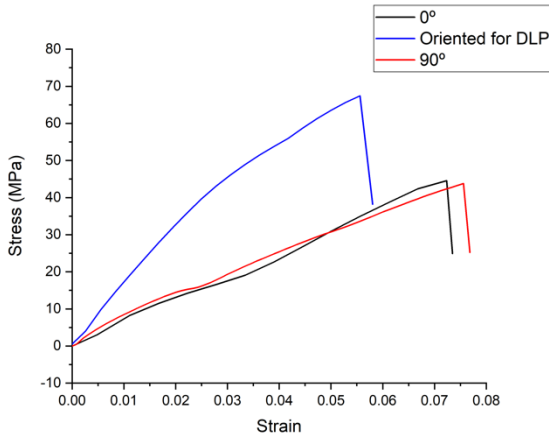


**Fig. 9 Stress [MPa] vs strain graph from the samples fabricated in different orientations.**

### 3.2 Compression Mechanical Test

The engineering stress vs. engineering strain curves (Fig. 10) were generated based on the collected data from the compression testing with the 100 kN cell load capacity for CD, HPVC, and TVC lattice structured samples. The engineering strain was found by dividing the displacement by the original height of each sample (15 mm). Few images are provided on the engineering stress vs engineering strain plots to investigate the deformation process; each test was recorded using a camera (Fig. 10).

Stress-strain curve Fig. 10(c) of HPVC samples shows extensive stress plateau phase before reaching the densification strain. The dome-like curve, which started at around 0.45 engineering strain, indicated that this structure required a lot of loads to break the last layer. There were not so many notches appeared on the curve as grooves appeared on the curve of CD and TVC. The average yield stress was around 95 MPa for HPVC lattice structures. The stress dropped right after the yield point achieved and was in the range of 63.2% - 46.67%. In the case of CD and TVC structures Fig. 10 (a, c), gradual breakage of the layers was observed. No sudden drop of stress was visible to identify the elastic limit on the curves for both of the lattice structures. The stress dropped and repeatedly rose as a member, or few members broke together. CD lattice structures needed a lot higher amount of stress compared to TVC lattice structures. The stress dropped before buckling for TVC samples, and was shallow compared to that exhibited in HPVC samples (20% to 35.7%).

The TVC lattice structures seemed to be the weakest of all three because as it is very clear from the meager curve amount of stress was required for the breakage of the structure. On the other hand, HPVC lattice structures showed the best structural integrity and superior performance under compression testing. All the curves went very high in the end, implying that all the

layers were broken down and lattice structures became a completely solid, which requires the highest load to compress further. Compressive testing for all lattice structures proceeded with breaking the bottom layer first, then the layer on top of that and so on until the structures formed a horizontal surface.

### 3.2. Size Optimization of Lattice Unit Cells

The results generated from the size optimization process performed in nTopology Element for three lattice configurations are summarized in Table 2. As can be seen from the images shown in Fig. 11, portions of the struts are thickened while other portions are becoming thinner depending on the FEA results. The hexagonal prism vertex centroid exhibits the lowest maximum Von Mises stress compared to tetrahedral prism vertex centroid and cubic diamond. On the other hand, CD is the most stressed structure after the optimization.

**Table 2 Number and iterations, and Von Mises stress for the optimized lattice TVC, HPVC, and CD unit cells.**

Type	Number of Iterations	Min Von Mises Stress [MPa]	Max Von Mises Stress [MPa]
TVC	6	18.377	63.422
HPVC	6	12.621	60.226
CD	8	5.274	65.655

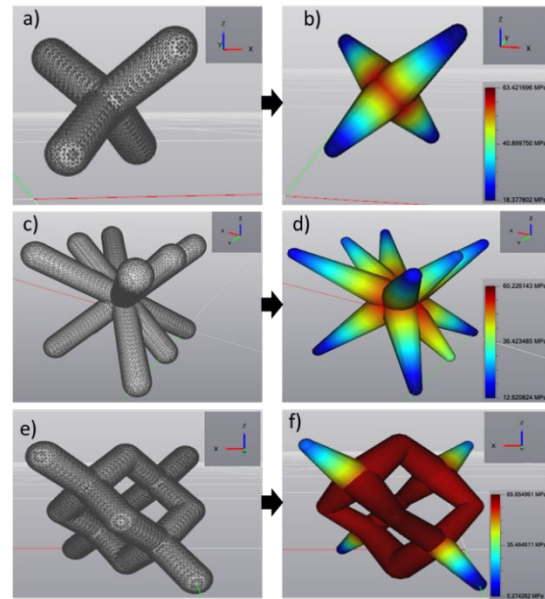


**Fig. 11 Original (on the left) and optimized lattice unit cells (on the right) for each configuration: TVC (a) and (b); HPVC (c) and (d); CD (e) and (f).**

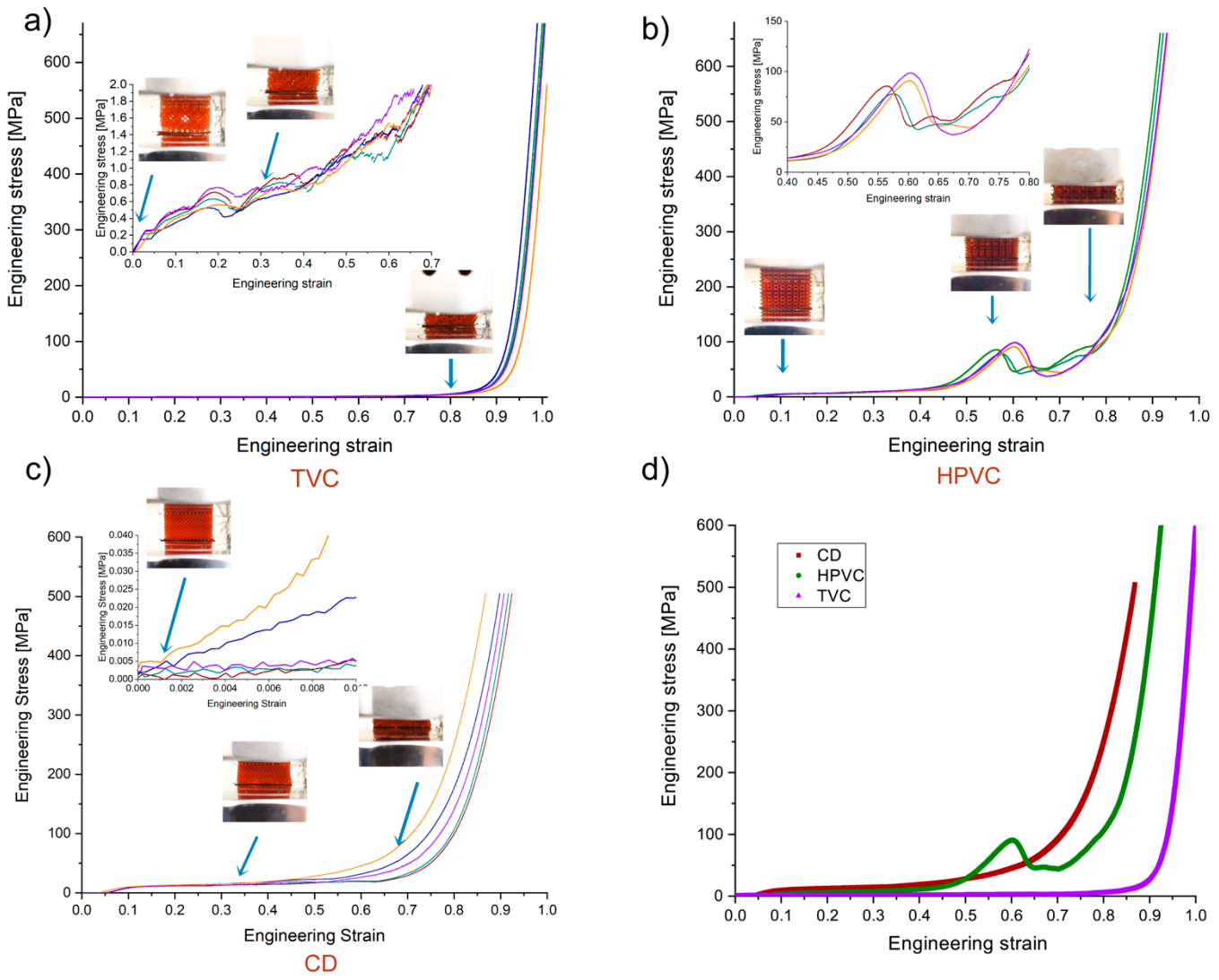


**Fig. 10 Engineering stress [MPa] vs. engineering strain for: (a) Tetrahedral Vertex Centroid (TVC); (b) Hexagonal Prism Vertex Centroid (HPVC); (c) Cubic Diamond (CD); and (d) all three configurations.**

#### 4. CONCLUSIONS

This paper addresses the mechanical performance of lattice structures fabricated by additive manufacturing. Tetrahedral Vertex Centroid (TVC), Hexagonal Prism Vertex Centroid (HPVC), and Cubic Diamond (CD) were designed, and 3D printed using direct light processing (DLP) technology and E-silicone material. The mechanical behavior of the E-silicone material was obtained by performing tensile testing on standard dog-bone samples designed according to ASTM D 638-14 (Type 5) standard. Compression mechanical testing was used to investigate the mechanical behavior of fifteen cuboid lattice structures (five for each configuration) with dimensions of 25mm × 25mm × 15mm. Furthermore, a process for designing

and size optimization of the unit cell configurations was presented. From the analysis of the results, it was concluded that:

1. The configuration of the lattice unit cell has a significant effect on the mechanical performance and weight of a structure.
2. Consistency on the tensile testing was found in all orientations, and the DLP oriented sample presented a UTS of 66.6822 MPa and a Young's modulus of 1.65 GPa.
3. CD lattice structured samples showed very ductile behavior compared to TVC and HPVC.
4. The engineering stress vs. engineering strain curve for HPVC samples showed that the stress dropped in the range of 63.2% - 46.67%.

5. The curves of TVC and HPVC showed similar behavior except TVC curves revealed more and repeated buckling of the lattice structures. The stress drop before buckling was very low compared to HPVC samples (20% to 35.7%).
6. CD and HPVC exhibit higher strength compared to TVC samples.
7. From the size optimization results, HPVC exhibits the lowest max Von Mises stress compared to CD, and TVC. The optimized HPVC structure has better stress distribution compared to CD structure. The highly stressed area for HPVC structure is significantly smaller compared to CD structure. Therefore, from the analysis of results of the size optimization, it is suggested that HPVC unit cell is appropriate to be incorporated in the design of a shoulder hemiprosthesis.

## 5. FUTURE WORK

The Hexagonal Prism Vertex Centroid (HPVC) lattice cell configuration will be used in the design and optimization of a shoulder hemi prosthesis for a patient that has a tumor on his humerus. A finite element analysis (FEA) will be performed on the shoulder hemi prosthesis consisting of HPVC configuration with uniform strut thickness. In order to further study the improvement of performance, the optimized HPVC with varying strut thickness will be investigated using FEA. A prototype of the final design implant will be fabricated using selective laser melting.

## ACKNOWLEDGMENTS

The research was possible with the support of the College of Engineering of the University of North Texas, the CONACYT Mixed Scholarships Program and the Research Group in Advanced Manufacturing of Tecnológico de Monterrey.

## REFERENCES

[1] Gibson, Lorna J., Ashby, Michael F. and Harley, Brendan A. "Structure and Mechanics of Cellular Materials." *Cellular Materials in Nature and Medicine*. Cambridge University Press, New York (2010): pp. 3-73.

[2] Rosen, David W. "Computer-Aided Design for Additive Manufacturing of Cellular Structures." *Journal of Computer-Aided Design & Applications* Vol. 4 No. 5 (2007): pp. 585-594. DOI 10.1080/16864360.2007.10738493.

[3] Mahmoud, Dalia and Elbestawi, Mohamed A. "Lattice Structures and Functionally Graded Materials Applications in Additive Manufacturing of Orthopedic Implants: A Review." *Journal of Manufacturing and Materials Processing* Vol. 1 No. 2 (2017): pp. 13. DOI 10.3390/jmmp1020013.

[4] Beyer, Christiane and Figueroa, Dustin. "Design and Analysis of Lattice Structures for Additive Manufacturing." *ASME Journal of Manufacturing Science and Engineering* Vol. 138 No. 12 (2016): pp. 15. DOI 10.1115/1.4033957.

[5] Gibson, Lorna J., Ashby, Michael F. and Harley, Brendan A. "Cellular Solids as Biomedical Materials." *Cellular Materials in Nature and Medicine*. Cambridge University Press, New York (2010): pp. 225-248.

[6] Tang, Yunlong, Kurtz, Aidan and Zhao, Yaoyao F. "Bidirectional Evolutionary Structural Optimization (BESO) Based Design Method for Lattice Structure to Be Fabricated by Additive Manufacturing." *Journal of Computer-Aided Design* Vol. 69 (2015): pp. 91-101. DOI 10.1016/j.cad.2015.06.001.

[7] Chang, Patrick S. and Rosen, David W. "The Size Matching and Scaling Method: A Synthesis Method for the Design of Mesoscale Cellular Structures." *International Journal of Computer Integrated Manufacturing* Vol. 26 No. 10 (2013): pp. 907-927. DOI 10.1080/0951192X.2011.650880.

[8] Katti, Kalpana S. "Biomaterials in Total Joint Replacement." *Journal of Colloids and Surfaces B: Biointerfaces* Vol. 39 No. 3 (2004): pp. 133-142. DOI 10.1016/j.colsurfb.2003.12.002.

[9] Frost, Harold M. "Wolff's Law and Bone's Structural Adaptations to Mechanical Usage: An Overview for Clinicians." *Journal of The Angle Orthodontist* Vol. 64 No.3 (1994): pp. 175-188.

[10] He, Yuhao, Burkhalter, Drew, Durocher, David and Gilbert, James M. "Solid-Lattice Hip Prosthesis Design: Applying Topology and Lattice Optimization to Reduce Stress Shielding from Hip Implants." *ASME Proceedings of the 2018 Design of Medical Devices Conference*. DMD2018-6804: pp. 5. Minneapolis, MN, April 9-12, 2018. DOI:10.1115/DMD2018-6804.

[11] Arabnejad, Sajad and Pasini, Damiano. "Multiscale Design and Multiobjective Optimization of Orthopedic Hip Implants with Functionally Graded Cellular Material." *Journal of Biomechanical Engineering* Vol. 134 No. 3 (2012): pp. 031004. DOI 10.1115/1.4006115.

[12] Jetté, Bruno, Brailovski, Vladimir, Dumas, Mathieu, Simoneau, Charles, and Terriault, Patrick. "Femoral Stem Incorporating a Diamond Cubic Lattice Structure: Design, Manufacture and Testing." *Journal of the Mechanical Behavior of Biomedical Materials* Vol. 77 (2018): pp. 58-72. DOI 10.1016/j.jmbbm.2017.08.034.

[13] Hollister, Scott J. and Taboas, Juan M. "Optimal Design and Fabrication of Scaffolds to Mimic Tissue Properties and Satisfy Biological Constraints." *Journal of Biomaterials* Vol. 23 No. 20 (2002): pp. 4095-4103. DOI 10.1016/S0142-9612(02)00148-5.

- [14] Chen, Yuhang, Zhou, Shiwei and Li, Qing. "Microstructure Design of Biodegradable Scaffold and Its Effect on Tissue Regeneration." *Journal of Biomaterials* Vol. 32 No. 22 (2011): pp. 5003-5014. DOI 10.1016/j.biomaterials.2011.03.064.
- [15] Yang, Sheng and Zhao, Yaoyao F. "Additive Manufacturing-Enabled Design Theory and Methodology: A Critical Review." *the International Journal of Advanced Manufacturing Technology* Vol. 80 No. 1-4 (2015): pp. 327-342.
- [16] Giannitelli, Sara Maria, Accoto, Dino, Trombetta, Marcella and Rainer, Alberto. "Current Trends in the Design of Scaffolds for Computer-Aided Tissue Engineering." *Journal of Acta Biomaterialia* Vol. 10, No.2 (2014): pp. 580-594. DOI 10.1016/j.actbio.2013.10.024.
- [17] Wang, Xiaojian, Xu, Shanqing, Zhou, Shiwei, Xu, Wei, Leary, Martin, Choong, Peter, Qian, Ma, Brant, Milan and Xie, Yi Min. "Topological Design and Additive Manufacturing of Porous Metals for Bone Scaffolds and Orthopaedic Implants: A Review." *Journal of Biomaterials* Vol. 83 (2016): pp. 127-141. DOI 10.1016/j.biomaterials.2016.01.012.
- [18] Wettergreen, Matthew A., Bucklen, Brandon S., Starly, Binil, Yuksel, Eser, Sun, Wei, Liebschner, Michael A.K. "Creation of a Unit Block Library of Architectures for Use in Assembled Scaffold Engineering." *Journal of Computer-Aided Design* Vol. 37 No.11 (2005): pp. 1141-1149. DOI 10.1016/j.cad.2005.02.005.
- [19] Sun, Wei, Starly, Binil, Nam, Jae, Darling, Andrew. "Bio-CAD Modeling and Its Applications in Computer-Aided Tissue Engineering." *Journal of Computer-Aided Design* Vol. 37 No. 11 (2005): pp. 1097-1114. DOI 10.1016/j.cad.2005.02.002.
- [20] Feinberg, Stephen E., Hollister, Scott J., Halloran, John W. and Chu, Tien-Min G. "Image-Based Biomimetic Approach to Reconstruction of the Temporomandibular Joint." *Journal of Cells Tissues Organs* Vol. 169 No.3 (2001): pp. 309-21. DOI 10.1159/000047896.
- [21] Xiao, Zefeng, Yang, Yongqiang, Xiao, Ran, Bai, Yuchao, Song, Changhui and Wang, Di. "Evaluation of Topology-Optimized Lattice Structures Manufactured Via Selective Laser Melting." *Journal of Materials & Design* Vol. 143 (2018): pp. 27-37. DOI 10.1016/j.matdes.2018.01.023.
- [22] Rajagopalan, Srinivasan and Robb, Richard A. "Schwarz meets Schwann: Design and Fabrication of Biomorphic and Durataxic Tissue Engineering Scaffolds." *Journal of Medical Image Analysis* Vol. 10 No.5 (2006): pp. 693-712. DOI 10.1016/j.media.2006.06.001.
- [23] Müller, Theo and Klashorst, Etienne. "A Quantitative Comparison Between Size, Shape, Topology and Simultaneous Optimization for Truss Structures." *Latin American Journal of Solids and Structures* Vol. 14 No. 12 (2017): pp. 1679-7817. DOI 10.1590/1679-78253900.
- [24] Ahari, Ali, Atai, Ali A. and Deb, Kalyanmoy. "Simultaneous Topology, Shape and Size Optimization of Truss Structures by Fully Stressed Design Based on Evolution Strategy." *Journal of Engineering Optimization* Vol. 47 No.8 (2015): pp. 1063-1084. DOI 10.1080/0305215X.2014.947972.
- [25] ASTM F2792-12a. "Standard Terminology for Additive Manufacturing Technologies, (Withdrawn 2015)." *ASTM International*, West Conshohocken, PA. 2012. DOI: 10.1520/F2792-12A. www.astm.org/Standards/F2792.
- [26] Thompson, Mary K., Moroni, Giovanni, Vaneker, Tom, Fael, Georges, Campbell, Ian, Gibson, Ian, Bernar, Alain, Schulz, Joachim, Graf, Patricia, Ahuja, Bhriugu and Martina, Filomeno. "Design for Additive Manufacturing: Trends, Opportunities, Considerations, and Constraints." *CIRP Annals* Vol. 65 No. 2 (2016): pp. 737-760. DOI10.1016/j.cirp.2016.05.004.
- [27] Javaid, Mohd and Haleem, Abid. "Additive Manufacturing Applications in Medical Cases: A literature Based Review." *Alexandria Journal of Medicine* Vol. 54 No. 4 (2018): pp. 411-422. DOI 10.1016/j.ajme.2017.09.003.
- [28] Bose, Susmita, Ke, Dongxu, Sahasrabudhe, Himanshu, Banyopahyay, Amit. "Additive Manufacturing of Biomaterials." *Progress in Materials Science* Vol 93 (2018): pp. 45-111. DOI 10.1016/j.pmatsci.2017.08.003.
- [29] Mezzadri, Francesco, Bouriakov, Vladimir and Qian, Xiaoping. "Topology Optimization of Self-Supporting Support Structures for Additive Manufacturing." *Additive Manufacturing* Vol. 21 (2018): pp. 666-682. DOI 10.1016/j.addma.2018.04.016.
- [30] Li, Hao, Li, Peigen, Gao, Liang, Zhang, Li, and Wu, Tao. "A Level Set Method for Topological Shape Optimization of 3D Structures with Extrusion Constraints." *Computer Methods in Applied Mechanics and Engineering* Vol. 283 (2015): pp. 615-635. DOI 10.1016/j.cma.2014.10.006.
- [31] Tang, Yunlong, Dong, Guoying, Zhou, Qinxue and Zhao, Yaoyao F. "Lattice Structure Design and Optimization with Additive Manufacturing Constraints." *IEEE Transactions on Automation Science and Engineering* Vol. No. (2017): pp. 1546-1562. DOI 10.1109/TASE.2017.2685643.
- [32] Gardan, Julien. "Additive Manufacturing Technologies: State of the Art and Trends." *International Journal of Production Research* Vol. 54 No. 10 (2016): pp. 3118-3132. DOI 10.1080/00207543.2015.1115909.
- [33] Patel, Dinesh K., Sakhaei, Amir H., Layani, Michael, Xhang, Biao, Ge, Qi and Magdassi, Shlomo. "Highly Stretchable and UV Curable Elastomers for Digital Light Processing Based 3D Printing." *Advanced Materials* Vol. 29 No.15 (2017): pp. 1606000. DOI 10.1002/adma.201606000.
- [34] ASTM D638-14. "Standard Test Method for Tensile Properties of Plastics." *ASTM International*, West

Conshohocken, PA, 2014. DOI: 10.1520/D0638-14.  
[www.astm.org/Standards/D638](http://www.astm.org/Standards/D638).

[35] Yan, Chunze, Hao, Liang, Hussein, Ahmed and Raymont, David. "Evaluations of Cellular Lattice Structures Manufactured Using Selective Laser Melting." *International Journal of Machine Tools and Manufacture Vol. 62 (2012)*: pp. 32-38. DOI 10.1016/j.ijmachtools.2012.06.002.

[36] ASTM F2792-12a. "Standard Terminology for Additive Manufacturing Technologies, (Withdrawn 2015)." *ASTM International*, West Conshohocken, PA, 2012. DOI: 10.1520/F2792-12A. [www.astm.org/Standards/F2792](http://www.astm.org/Standards/F2792).

# Published papers

1. **Mechanical Behavior of Lattice Structures Fabricated by Direct Light Processing With Compression Testing and Size Optimization of Unit Cells.** January 2020 | ASME, IMECE
2. **Bone-Integrated Optical Micro lasers for In-Vivo Diagnostic Biomechanical Performances** January 2020 | ASME, IMECE
3. **Preparation of electrospun fibers of Poly (L-lactide-co-D, L-lactide) with Na<sub>2</sub>Ti<sub>6</sub>O<sub>13</sub>, Ca<sub>3</sub>(PO<sub>4</sub>)<sub>2</sub> and ZrO<sub>2</sub> as a bioactive mesh.** October 2019 | Carbon MEMS
4. **Parametric Modeling of Biomimetic Cortical Bone Microstructure for Additive Manufacturing** Mar 19, 2019 Materials | MDPI
5. **Alginate/Gelatin Hydrogels Reinforced with TiO<sub>2</sub> and β-TCP Fabricated by Micro extrusion-based Printing for Tissue Regeneration** Mar 11, 2019 Polymers MDPI
6. **Electrospun Polycaprolactone Fibrous Membranes Containing Ag, TiO<sub>2</sub> and Na<sub>2</sub>Ti<sub>6</sub>O<sub>13</sub> Particles for Potential Use in Bone Regeneration** Jan 10, 2019 Membranes | MDPI
7. **Structural design optimization of knee replacement implants for Additive Manufacturing,** January 01, 2019, Procedia Manufacturing
8. **Process planning guidelines in selective laser melting for the manufacturing of stainless-steel parts** Jun 21, 2018, Procedia Manufacturing
9. **Process chain for the fabrication of a custom 3D barrier for guided bone regeneration,** 3rd CIRP Biomanufacturing, 2017
10. **Process chains for the Development of Medical Implants using Metal Additive Manufacturing,** November 2017 Research Discovery Workshop
11. **Permeability Study of Austenitic Stainless-Steel Surfaces Produced by Selective Laser Melting,** Nov 24, 2017, Metals
12. **Manufactura Digital Aplicada a la Regeneración Guiada de Hueso Alveolar,** Oct 24, 2017, CNIB 2017
13. **Electrospinning PCL nanofibers with ceramic nanoparticles for wound dressing,** Nov 6, 2015, Congreso Anual de la Sociedad Española de Ingeniería Biomédica / ISBN: 978-84-608-3354-3
14. **Electrospun antibacterial meshes for Dermal Skin Protection,** Aug 27, 2015 Conference: International Materials Research Conference, At Cancun, Mexico, Volume: XXIV

# Curriculum Vitae

## Erick Ramírez-Cedillo

erick.ramce@gmail.com | Lucila Godoy 135, Col. Roma, Monterrey, N.L. | +521 (81) 1538 8614

### Researcher, academic and entrepreneur

I am looking forward to being part of a research center/academic institution where I can make contributions to the literature on the topics of advanced manufacturing. As part of my experience, I have successfully created startups product of my research, and I can help the organization on the business development and commercialize the research projects. In my international experience, I learned how to lead with different cultures, establish proper communication, and obtain good results. My expertise in advanced manufacturing covers optimization of parameters, process chains, process guidelines, life cycle inventory, design and optimization of parts, and others. I have a passion for innovation and organization, to end what I start, open to new challenges, and teach what I have learned.

### Professional Experience

#### Cofounder and CEO

Monterrey, MX

3D FACTORY MX

01/2013 – current

- Development of the Website and eCommerce (www.3dfactory.mx), subdomains, and the punch out system/manufacturing on demand for different clients. Development of the strategy management of the online store: receive orders, inventory management, and order delivery.
- Customer service, negotiation, and client facing capacity.
- Suppliers negotiation, logistics, and management of inventories.
- Commercial Agreements with distributors and retailers in Mexico and worldwide.
- Annual financial reports, annual objectives and goals, sales planning and legal representation of the company.
- Procurement of external funding (government, investors, banks).
- Infrastructure selection and plant layout.
- Design of the workflow and the operation of the additive manufacturing/3D Printing services.
- Engineering management of projects using 3D Printing technologies such as FDM, SLA, DLP, SLS, SLM, BJ and others.

#### Cofounder

MX

CUSTOMED

– current

- Design and manufacturing of cranial, humerus, tibia, and maxillofacial implants using metal additive manufacturing (SLM)
- Inverse engineering projects using digitalization with 3D scanners.

#### Research Visiting Scholar

Denton, TX, USA

University of North Texas

06/2018 – 08/2019

- Responsible of research projects in collaboration with Emerson US in topics of corrosion of stainless steel parts fabricated with metal additive manufacturing (Stainless Steel 316L / Stainless Steel 17-4PH).
- Evaluated and tested mechanical properties of different lattices structures with metal and polymers using additive manufacturing using nTopology and Netfabb Premium.
- Performed parameters optimization and process guidelines for the Additive Manufacturing Lab (SLM Machine, Aconity 3D Midi)

#### Tecnológico de Monterrey

MX

Professor

01/2016 – 06/2016

- Professor of the class *Innovation of Processes and Prototypes Design* for students of the B.S. Innovation and Development Engineering.

#### Researcher

01/2016-12/2019

- Responsible of research project about life cycle inventory and parameters optimization for a powder bed fusion machine (Renishaw AM400)

01/2014 – 12/2015,



- Responsible of the design of experiments for several project with different characterization techniques such as: SEM, mechanical testing (tensile, fatigue and compression), hardness, roughness, porosity and density, micro-CT, and results were reported with a statistical analysis.
- Responsible of the fabrication of parts using additive manufacturing with SLM, DLP, FDM, BJ, and others.
- Collaboration between different institutions such as UNAM (Mexico), UNT (USA), CEITEC (Czech Republic), UANL (México), MADIT (México), Hospital Universitario (México).
- Design and fabrication of electrospun meshes for wound dressing and tissue engineering.
- Experimental work with fibroblasts and cells. Physical and chemical analysis like: FTIR, XRD, DSC and morphological analysis with SEM.

#### Laboratory coordinator

01/2013 – 12/2014

- Administration of the students of this laboratory and courses.
- Design and development of a new Computerized Drawing manual for NX 8.0.

### Education

<b>PhD in Engineering Sciences</b>	<b>2019</b>
Tecnológico de Monterrey, Campus Monterrey	
<b>Master in Sciences</b>	<b>2015</b>
Tecnológico de Monterrey, Campus Monterrey	
<b>B.E in Mechatronics</b>	<b>2013</b>
Tecnológico de Monterrey, Campus Monterrey	

### Languages

English (TOEFL 567), Spanish (native) and French (DELTA A1), German (basic)

### Research Publications

- **Mechanical Behavior of Lattice Structures Fabricated by Direct Light Processing with Compression Testing and Size Optimization of Unit Cells.** January 2020 | ASME, IMECE
- **Bone-Integrated Optical Microlasers for In-Vivo Diagnostic Biomechanical Performances** January 2020 | ASME, IMECE
- **Preparation of electrospun fibers of Poly (L-lactide-co-D, L-lactide) with Na<sub>2</sub>Ti<sub>6</sub>O<sub>13</sub>, Ca<sub>3</sub>(PO<sub>4</sub>)<sub>2</sub> and ZrO<sub>2</sub> as a bioactive mesh.** October 2019 | Carbon MEMS
- **Parametric Modeling of Biomimetic Cortical Bone Microstructure for Additive Manufacturing** Mar 19, 2019 Materials | MDPI
- **Alginate/Gelatin Hydrogels Reinforced with TiO<sub>2</sub> and  $\beta$ -TCP Fabricated by Microextrusion-based Printing for Tissue Regeneration** Mar 11, 2019 Polymers MDPI
- **Electrospun Polycaprolactone Fibrous Membranes Containing Ag, TiO<sub>2</sub> and Na<sub>2</sub>Ti<sub>6</sub>O<sub>13</sub> Particles for Potential Use in Bone Regeneration** Jan 10, 2019 Membranes | MDPI
- **Structural design optimization of knee replacement implants for Additive Manufacturing,** January 01, 2019, Procedia Manufacturing
- **Process planning guidelines in selective laser melting for the manufacturing of stainless-steel parts** Jun 21, 2018, Procedia Manufacturing
- **Process chain for the fabrication of a custom 3D barrier for guided bone regeneration,** 3rd CIRP Biomanufacturing, 2017
- **Process chains for the Development of Medical Implants using Metal Additive Manufacturing,** November 2017 Research Discovery Workshop
- **Permeability Study of Austenitic Stainless-Steel Surfaces Produced by Selective Laser Melting,** Nov 24, 2017, Metals
- **Manufactura Digital Aplicada a la Regeneración Guiada de Hueso Alveolar,** Oct 24, 2017, CNIB 2017
- **Electrospinning PCL nanofibers with ceramic nanoparticles for wound dressing,** Nov 6, 2015, Congreso Anual de la Sociedad Española de Ingeniería Biomédica / ISBN: 978-84-608-3354-3
- **Electrospun antibacterial meshes for Dermal Skin Protection,** Aug 27, 2015 Conference:International Materials Research Conference, At Cancun, Mexico, Volume: XXIV

### Recognition and awards

- Finalist in the National Entrepreneur Award in the category of Small Companies in Mexico (*Mar 2018, Secretaría de Economía*)
- 16 young promises of the Mexican Engineering (Apr 2017, Manufactura de Grupo Expansión)

### Courses

- Training in SLM Machine Aconity MIDI - Aconity 3D USA, 2019
- Micro/nano-fabrication course - Massachusetts Institute of Technology (MIT), 2019
- Process parameters for SLM machines - Renishaw Canada, 2017